

High Fidelity Probe and Mitigation of Mirror Thermal Fluctuations

Thesis by
Tara Chalermongsak

In Partial Fulfillment of the Requirements
for the Degree of
Doctor of Philosophy



California Institute of Technology
Pasadena, California

2014
(Defended May 22, 2014)

© 2014

Tara Chalermongsak

All Rights Reserved

Acknowledgments

Each day, after spending strenuous hours of lab work and about to call it a night, I liked to look around the setup of the work. Not only did I think about what could be improved or what to be fixed, but I also reminded myself about how far I had accomplished with a lot of help from several people who taught me all about the optic mounts on the table, electronic equipments, or even softwares for controlling the setup. I consider myself very fortunate to learn from many of the smartest people I have ever known over the years.

First, I have to thank Rana Adhikari for taking me under his wing and entrusting me to this exciting experiment, and for his patient for teaching someone who's not the fastest learner like me. I'm also grateful for Eric Gustafson, another boss who always has indispensable advice on my work. I also thank Yanbei Chen, Kenneth Libbrecht, and Alan Weinstein for serving on my committee.

I learned many crucial lab skills from Frank Seifert whose help contributes significantly to my work. Also, I am grateful to Koji Arai, Peter King, Vladimir Degarchev, Matt Abernathy, Nicolas Smith, Steve Vass, Jamie Rollins, Jan Harms, Aidan Brooks, Alastair Heptonstall, Manasa Thiruganasambandamand, and Larry Price. They were always ready to answer any questions I had. Without them, I would be like a blind man roaming in a minefield.

The work would not be made possible without all the electronic supports from LIGO engineers, especially, Daniel Sigg, Rich Abbott, and Charles Osthelder. They have been very kind to help me through these years.

Also, I like to thank all the TNI members, Riccardo DeSalvo, Eric Black, Akira Villar, and Greg Ogin from their guidance during my first few years at Caltech. Their researches motivated my study in the following years.

I appreciate all the help from my grad student fellows, David Yeaton-Massey, Jenne Driggers, Kiwamu Izumi, Zach Korth, Eric Quintero, Denis Martynov, and Evan Hall. I used to struggle with problems alone, and it was devastating. They taught me how to help and learn from each others and the value of teamwork.

SURF students who worked with me, Rafael Cervantes, Megan Daily, Larissa Thorne, Vanessa Acon, Sarah Terry, Erica Chan, and Chloe Ling helped me with various lab tasks. I'm glad I had chances to co-mentor these brilliant students.

I'm also indebted to all Physics and LIGO members, especially Donna Driscoll, Julie Hiroto, and Gina Salone for their help and support on various works.

I also have to thank Laura F. Kim, Daniel Yolder and Caltech ISP team who have helped me with all the issues for an international student like me.

I am lucky to know some Caltech Thai students who always share laugh and cry with me. Special thanks to Tichakorn Wongpiromsarn and Piti Ongmongkolkul for several useful helps and discussions in maths and physics.

Above all, I would like to thank my family. I am indeed fortunate to have them standing beside me throughout my life. The pursuit of Ph.D. would not have been possible without their unfailing love and support.

Abstract

Thermal noise arising from mechanical loss in high reflective dielectric coatings is a significant source of noise in precision optical measurements. In particular, Advanced LIGO, a large scale interferometer aiming to observed gravitational wave, is expected to be limited by coating thermal noise in the most sensitive region around 30–300 Hz. Various theoretical calculations for predicting coating Brownian noise have been proposed. However, due to the relatively limited knowledge of the coating material properties, an accurate approximation of the noise cannot be achieved. A testbed that can directly observed coating thermal noise close to Advanced LIGO band will serve as an indispensable tool to verify the calculations, study material properties of the coating, and estimate the detector's performance.

This dissertation reports a setup that has sensitivity to observe wide band (10 Hz to 1 kHz) thermal noise from fused silica/tantala coating at room temperature from fixed-spacer Fabry–Perot cavities. Important fundamental noises and technical noises associated with the setup are discussed. The coating loss obtained from the measurement agrees with results reported in the literature.

The setup serves as a testbed to study thermal noise in high reflective mirrors from different materials. One example is a heterostructure of $\text{Al}_x\text{Ga}_{1-x}\text{As}$ (AlGaAs). An optimized design to minimize thermo–optic noise in the coating is proposed and discussed in this work.

Contents

Acknowledgments	iii
Abstract	v
1 Introduction to Thermal Noise	1
1.1 Thermal Noise in Various Measurements	1
1.1.1 The Brownian Movement	1
1.1.2 Johnson-Nyquist Noise	2
1.1.3 Micro Electromechanical Systems: MEMS	3
1.1.4 Torsion Pendulum	3
1.1.5 Optical Clock	4
1.1.6 Laser Interferometer Gravitational Wave Observatory	4
1.1.6.1 A Short Review on Gravitational Wave	5
1.1.6.2 LIGO Setup	6
1.1.6.3 Thermal Noise in LIGO	6
1.2 Direct Observations of Thermal Noise in High Reflective Mirrors	8
1.2.1 Previous Coating Thermal Noise Measurements	8
1.2.2 Coating Brownian Noise from Fixed Spacer Fabry–Perot Cavity	9
2 Thermal Noise in Fixed–Spacer Fabry–Perot Cavity	11
2.1 Fluctuation-Dissipation Theorem	13
2.2 Direct Approach	14
2.3 Two Kinds of Thermal Noise	14
2.3.1 Brownian Thermal Noise	15
2.3.2 Thermodynamic Noise	15
2.4 Thermal Noise in Substrate	16
2.4.1 Brownian Noise in Substrate	17
2.4.2 Thermoelastic Noise in Substrate	17
2.4.3 Thermo–Optic Noise in Substrate	18

2.5	Thermal Noise in Coatings	19
2.5.1	Brownian Noise in Coatings	19
2.5.2	Thermo–Optic Noise in Coatings	21
2.6	Thermal Noise in Spacer	23
2.6.1	Brownian Noise in Spacer	23
2.6.2	Thermoelastic Noise in Spacer	24
2.7	Photothermal Noise: Absorption from Shot Noise and Intensity Noise	25
2.8	Noise in the Bonding between a Mirror and a Spacer	26
2.8.1	Optical Contact	27
2.8.2	How to Measure Mechanical Loss in Optical Contact	27
2.9	How to Reduce Thermal Noise	28
2.9.1	Lower Temperature	28
2.9.2	Lower Loss	29
2.9.3	Different Beam Shape	30
2.9.4	No Coating Cavity	30
3	Experimental Setup	32
3.1	Optical Cavity as a Frequency Reference	33
3.2	Prototype Setup	35
3.2.1	8–inch Reference Cavities	35
3.2.2	Setup Layout	37
3.2.3	Result from the Prototype Setup	40
3.3	Two Laser Setup with 1.45 Inch Cavities	42
3.3.1	1.45 Inch Reference Cavities	42
3.3.2	Overall Explanation of The Two–Laser Setup	43
3.3.3	Result from 1.45 Inch Cavities	46
3.4	Discussion	46
4	Technical Noise in the Setups	49
4.1	Seismic Noise	49
4.1.1	Coupling from Seismic to Displacement Noise	49
4.1.2	Scattered Light and Seismic Isolation in the Setup	51
4.2	Mechanical Peaks from Opto–Mechanical Components	51
4.3	PDH Lock: Shot Noise	53
4.4	PDH Lock: Electronic Noise	55
4.5	PDH Lock: Residual Amplitude Modulation	56
4.6	Noise from Phase Locked Loop Readout	57

4.7	Photothermal Noise	61
4.8	Noise from Ambient Temperature	62
5	AlGaAs Crystalline Coatings	63
5.1	History of AlGaAs Usage	63
5.2	Thermo-Optic Noise and Coatings Optimization	64
5.2.1	Thermal Noise in AlGaAs Coatings	65
5.2.2	Optimization Consideration	66
5.2.3	Uncertainties in Material Parameters	69
5.2.4	Errors Due to Manufacturing Process	70
5.2.5	Optimization Method	71
5.2.6	Cavity Parameters	78
5.3	Implications for Advanced LIGO	78
6	Future Upgrade and Application	83
6.1	Future Upgrade	83
6.1.1	Improvement in Sensitivity at Low Frequency	83
6.1.2	Improvement in Sensitivity at High Frequency	85
6.2	Application: Frequency Stabilized Light Source	87
6.2.1	Laser Gyroscope	87
6.2.2	Crackle	88
6.2.3	External Cavity Diode Laser	89
A	Comparison with Other Experiments	91
B	Frequency Stabilization Servo	95
C	Material parameters for SiO₂/Ta₂O₅ and AlGaAs	99
C.1	Table of Parameters	99
C.2	Uncertainties in Parameters	99
C.3	Note for AlGaAs	100
D	High Reflective Coating Structure and its Average Properties	101
D.1	Why Half Wave Cap?	101
D.2	Averaged Material Parameters for Coatings	102
E	1.45 Inch Reference Cavity: Design and Assembly	104
E.1	Choosing Cavity Length	104
E.2	Assembling Reference Cavity with Optical Contact	105

E.3 Eigenmode study	110
E.4 Searching for Optimum Support Point with COMSOL	111
E.5 Mount Design and Assembly	111
F Pre-Mode Cleaner Cavity	117
F.1 Eigenmode Study	117
G Mathematical Note	119
G.1 Note About Fabry–Perot Cavity	119
G.2 Temperature Fluctuations for TO Calculation	120
G.3 Error Analysis of the Measurement	122
G.4 Bayesian Analysis	123
Bibliography	127

Chapter 1

Introduction to Thermal Noise

For a system in thermal equilibrium at temperature T , the Equipartition Theorem tells us that the average kinetic from each degree of freedom will be equal to $\frac{1}{2}k_B T$. For example, a 1-D mass-spring system with only one degree of freedom, will oscillate with an average energy of $\frac{1}{2}k_B T$. At first, it seems that the only movement will be $x(t) = x_0 \sin(2\pi ft)$, a perfect sinusoidal motion with its frequency f determined solely by the mass m and the spring constant k . However, if the spring has a mechanical loss which can be written as an imaginary part of the spring constant $k = k_0(1 + i\phi)$, where $\phi \ll 1$, this loss will cause an off-resonant motion that creates noise in other frequencies. In the next chapter, we will discuss more about Fluctuation-Dissipation theorem, which explains how loss and fluctuation in a system are related (for this chapter, we can just remember that a system that can dissipate the input energy, can exhibit fluctuations as in the mass-spring system).

This minute motion manifests itself in a larger scale and has been observed in various experiments, and becomes one of the fundamental limiting sensitivity for sensitive measurements. This chapter will give some examples of thermal noise in measurements.

1.1 Thermal Noise in Various Measurements

1.1.1 The Brownian Movement

When small particles (e.g., pollen grains) are suspended in still water with no influence from the surrounding, the particles will move randomly. This motion was observed in 1827 by Robert Brown [1] and it was named as Brownian motion. The particle's movement originates from continuous random collisions from the surrounding water molecules that move due to their thermal energy $k_B T$. It had been left as a mysterious phenomenon until explained by Einstein and verified by Jean Perrin [2, 3], almost a century later. This explanation of Brownian motion, which won the Nobel Prize in Physics in 1926 for Perrin, also confirmed the existence of atoms and molecules. The study also served as one of the proofs of the Equipartition Theorem [4].

1.1.2 Johnson-Nyquist Noise

Voltage noise in resistors relating to the temperature had been observed by Johnson in 1928 [5] (Fig. 1.1), and explained by Nyquist in the same year [6]. The cause is electrons' movement inside a resistor due to thermal agitation. Nyquist proved it using an argument that certain wave patterns can be formed in a system of two resistors joined by two transmission lines together with the Equipartition Theorem stating that each degree of freedom has an energy equal to $k_B T$. In general, the power spectral density of the voltage noise is

$$V^2(f) = \frac{4hf\Delta f}{\exp[\frac{hf}{k_B T}] - 1} \quad (1.1)$$

Usually, in most cases when $hf \ll k_B T$ (For example, $T = 300\text{K}$, f can be up to 100GHz), Eq. 1.1 is reduced to a more familiar form,

$$V^2(f) = 4Rk_B T \Delta f. \quad (1.2)$$

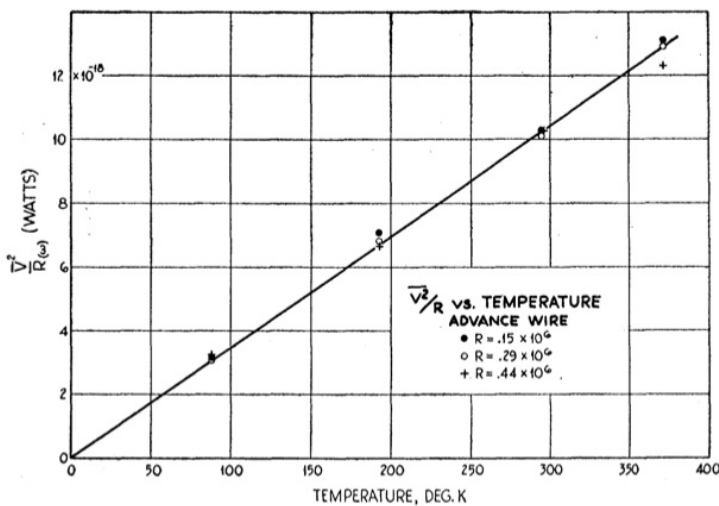


Figure 1.1: Apparent power $[V^2/R]$ vs. temperature, for Advance wire resistances [5]

Aside from this flat Johnson-Nyquist noise, there is another known noise in a resistor. It is directly proportional to the current flow and its power density varies with $1/f$. It has been observed in various metal films and found to be temperature dependent [7, 8]. This excess current noise is the bunching and releasing of electrons associated with current, e.g., due to fluctuating conductivity based on imperfect contacts within the resistive material. Hence the amount of this current-noise depends largely on the methods used to manufacture resistors [9, 10]. For metal films, this noise was found to be originated from the substrate on which the thin film is deposited [11, 12].

1.1.3 Micro Electromechanical Systems: MEMS

Developments in micro-machining process make small tools at micron scale possible. Typically, they consist of simple mechanical devices (e.g., a mass-spring system, a cantilever blade) with sizes of around 100 to 1000 microns, (see Fig. 1.2). These devices are suitable for space-limited applications because they are small and light. Similar to any mechanical systems, they are also subject to thermal noise due to intrinsic mechanical losses in the material [13]. Although the devices are usually limited by the related electrical noise and systematic errors, mechanical thermal noise sets the fundamental limit of the devices and it is important to characterize them for the improvement of the higher accuracy devices. Some examples of MEMS devices and their thermal noise considerations can be found in Ref. [14] for a frequency selective device using the mechanical resonance of a small cantilever blade, Ref [15] for a gyroscope, and Ref. [16] for a Fabry–Perot tunable etalon.

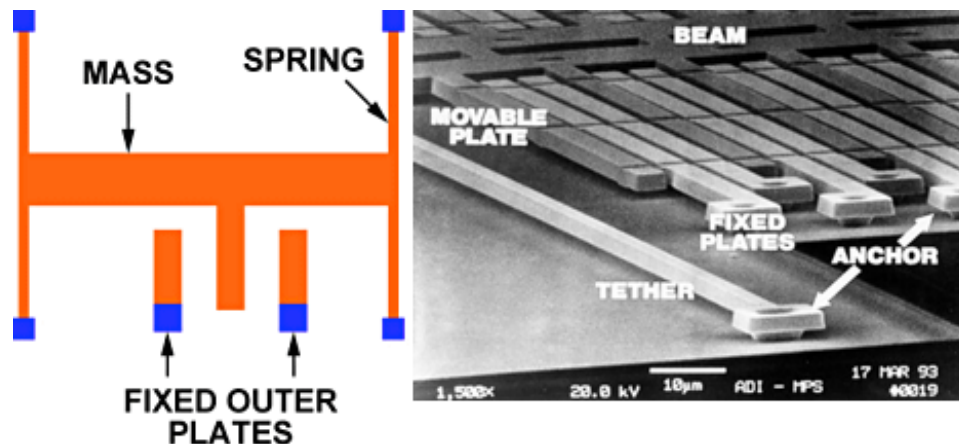


Figure 1.2: Left, a schematic diagram of a capacitive MEMS accelerometer. Right, a micrograph of the ADXL50 MEMS accelerometer's structure. Credit: www.sensorsmag.com

1.1.4 Torsion Pendulum

A torsion pendulum is another sensitive tool for determining the magnitude of a small force. One of the most famous experiment using this technique is Cavendish experiment [17] from which the gravitational constant value G can be derived. The torsion pendulum technique has been used for various experiments. For instance, the equivalence principle assumes that the inertial mass and the gravitational mass are the same, but this might not be true at all time. The Standard Model predicts the violation of the equivalent mass during a short period of time [18]. An experiment using a torsion pendulum helps improving a limit on the equivalence-principle violations [19]. Another example is a prediction from quantum electrodynamics (QED), the Casimir effect. It states that two parallel conduction plate placed closely to each other will be mutually attracted [20]. This effect can be demonstrated using a torsion pendulum [21].

Torsion pendula can be used to study the influence of solar eclipses on some mechanical processes on earth [22, 23], although, in this case, they are not used for determining any small forces. The oscillation period of the torsion pendulum increases during the solar eclipse. This phenomenon has not been properly explained.

Similar to other sensitive measurements, a torsion pendulum is subject to thermal noise due to loss in the torsion spring. A direct measurement to observe thermal noise in a torsion pendulum was done with a polyamide Nylon wire, and the result was in good agreement with the Fluctuation-Dissipation theorem [24].

1.1.5 Optical Clock

The optical clock [25] has been quickly developed as another frequency standard, which is important in various fields (e.g., primary standards, time distributions services, global navigation satellite systems (GPS)). Three main components of an optical clock are (1) a highly stable reference frequency (a narrow optical absorption line in an atom or ion)¹, (2) a laser (local oscillator), which is locked to that reference frequency, and (3) a femtosecond comb for measuring the frequency of the laser. The laser has two important tasks; it must probe the reference transition (the atomic system) while introducing minimal noise, and it must act temporarily as stable frequency reference to maintain the short to medium term stability of the frequency reference [27]. To do this, the laser is also frequency locked to a reference cavity. Thermal noise in that reference cavity, which will be studied in details in this dissertation, becomes one of the main limiting noise source of the laser's performance.

1.1.6 Laser Interferometer Gravitational Wave Observatory

The existence of gravitational waves was predicted as a consequence of the theory of general relativity [28, 29, 30]. As a gravitational wave propagates through space, it contracts and expands the space periodically. Although observations on the displacement due the warped space has never been made because of their extremely weak signals, there is strong evidence suggesting their existence. In 1974, a piece of evidence of gravitational waves was observed from the shrinking orbit of a binary system of two neutron stars, PSR1913+16 (one of which is also a pulsar) due to energy loss in the form of gravitational waves [31, 32]. The prediction of general relativity agrees with the measurement to accuracy of about 0.1 percent, after 30 years of data [33].

Another example is recent news at the time of writing this dissertation, researchers from the BICEP2 collaboration [34] have announced they found evidence of cosmic inflation and reported the image of gravitational waves from the Big Bang by observing the B-modes polarization of the cosmic

¹For optical lattice clock [26] the atoms are kept into an optical lattice instead of trapped by laser cooling. The method results in a better precision.

microwave background (CMB) [35]. This new finding is currently under peer review for scientific confirmation. Nevertheless, gravitational wave is real.

In 1990s, scientists proposed a large scale interferometer to measure gravitational wave (LIGO² [36]). The configuration based on a Michelson interferometer with 4-km arms. Later, a network of ground based observatories (VIRGO³ [37], GEO⁴ [38], KAGRA⁵ [39]) have been built around the world to increase the confidence and to pinpoint a location of an event. Some possible GW sources that will be detectable by the observatories are: signals from binaries, coalescing binaries, supernovae, or stochastic signals.

1.1.6.1 A Short Review on Gravitational Wave

In General Relativity, space-time is described by the mass-energy following the Einstein's field equation:

$$R_{\mu\nu} - \frac{1}{2}Rg_{\mu\nu} = \frac{8\pi G}{c^4}T_{\mu\nu}. \quad (1.3)$$

$R_{\mu\nu}$ is the Ricci curvature tensor, R is the scalar curvature, $g_{\mu\nu}$ is the metric tensor, which explains the structure of the space-time. The stress-energy tensor $T_{\mu\nu}$ describes the density and flux of energy, mass, and momentum in space-time. See Ref. [40] for more details. In a place far away from the presence of mass or energy, the space time metric $g_{\mu\nu}$ can be approximated as

$$g_{\mu\nu} = \eta_{\mu\nu} + h_{\mu\nu} \text{ with } |h_{\mu\nu}| \ll 1, \quad (1.4)$$

where $\eta_{\mu\nu}$ is the flat space-time (Minkowski) metric and $h_{\mu\nu}$ is a small perturbation due to the gravitational wave. In free space ($T_{\mu\nu} = 0$), substituting this space time metric to Einstein's field equations and using an appropriate gauge choice (transverse traceless gauge), the Einstein's field equation reduces to a wave equation for h :

$$\nabla^2 h_{\mu\nu} = \frac{\partial^2 h_{\mu\nu}}{\partial t^2} \quad (1.5)$$

Due to the constraints of the choice of gauge and the field equation, $h_{\mu\nu}$ can be decomposed into two linearly independent modes, which are h_+ and h_\times . Conventionally, h_+ squeezes and stretches along the \hat{x} and \hat{y} directions while h_\times will stretch and squeeze along $\hat{x} + \hat{y}$ and $\hat{x} - \hat{y}$ directions. If a gravitational wave with h_+ polarization propagates along the z -axis, an object with length L oriented along x or y axes will have the maximum displacement due to the strain equal to

$$\Delta L = Lh_+. \quad (1.6)$$

²<http://www.ligo.org>

³http://www.ego-gw.it/virgodescription/pag_4.html

⁴<http://www.geo600.org>

⁵<http://gwcenter.icrr.u-tokyo.ac.jp/en/>

For a binary system with its orbital plane being parallel to x-y plane, the strain h is [41]:

$$h(z, t) = \frac{-4G^2 M_1 M_2}{c^4 r z} \cos(2\pi f(z - ct)/c), \quad (1.7)$$

M_1, M_2 are the masses of the two bodies separated by distance r . For the binary system PSR1913+16, $M_1 = 1.44M_\odot$, $M_2 = 1.39M_\odot$, and M_\odot is the solar mass, $r = 2.3$ light seconds, $z = 20,000$ light years. Substituting these numbers in Eq. 1.7, we get the strain around 1.3×10^{-22} . However, the wave frequency is around 0.1 mHz, making it undetectable for the current sensitivity of the ground based observatory, see Fig. 1.4.

1.1.6.2 LIGO Setup

Due to the nature of a gravitational wave that warps space-time as it propagates, a Michelson interferometer can be a suitable tool for detecting the wave. A schematic diagram of LIGO is shown in Fig. 1.3. The input laser is separated into two directions orthogonal to each other. They bounce off of the high reflective mirrors at the end of each arm and recombine at the output. The differential length between the two arms, induced by the passing wave, results in the varying power of the output monitored by a photodiode.

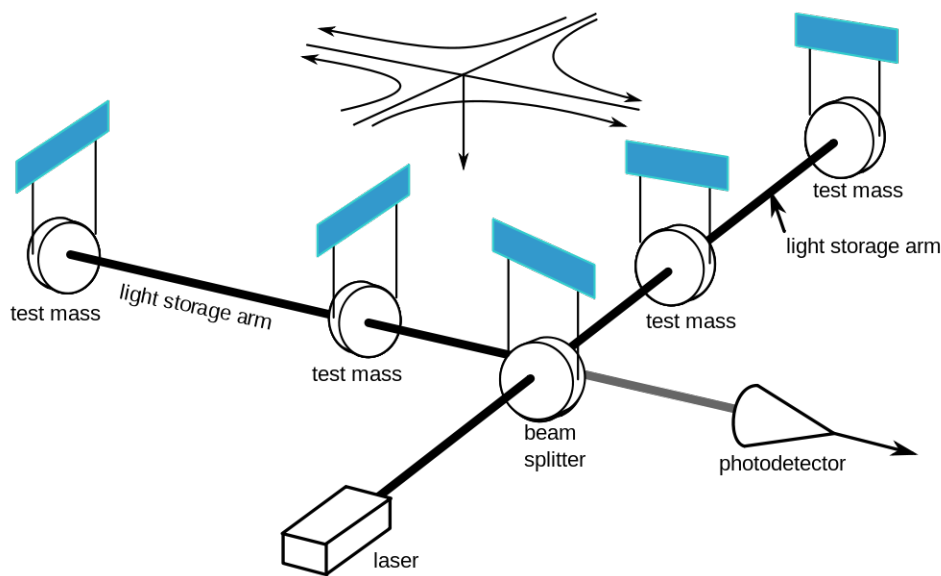


Figure 1.3: A simplified schematic diagram of LIGO. It is a Michelson interferometer with a Fabry–Perot cavity in each arm. The test masses are suspended for seismic isolations.

1.1.6.3 Thermal Noise in LIGO

Since the output signal of the interferometer is proportional to the differential length between the two arms, any displacement noise will corrupt the sensitivity of the detector. For example, seismic

motion on the ground that shakes the test masses' positions will prevent LIGO from detecting gravitational waves at frequencies below 10 Hz. The estimated noise budget of Advanced LIGO is shown in Fig. 1.4⁶.

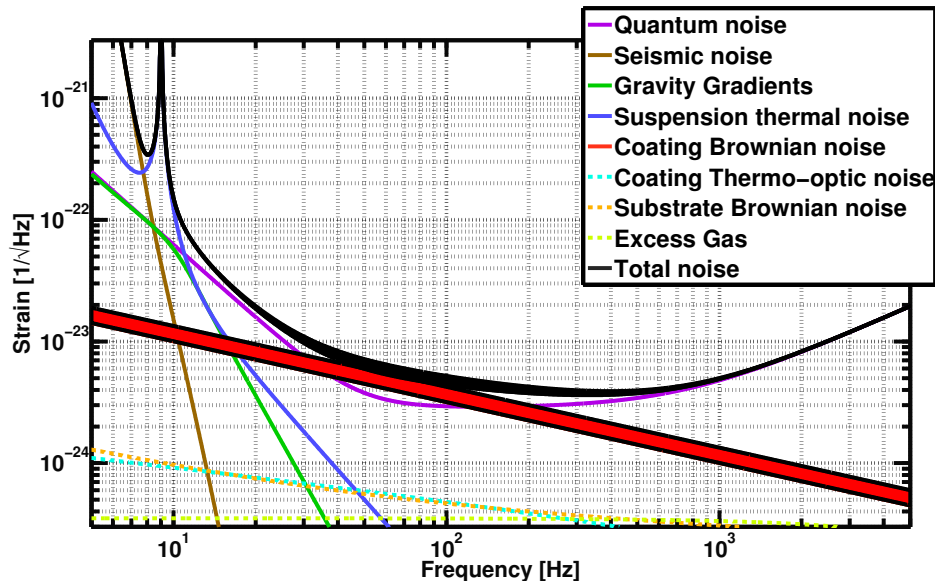


Figure 1.4: Baseline Advanced LIGO's noise budget (GWINC v2.0). 125 W input power [43]. Coating Brownian noise is plotted in confidence interval where uncertainties of coatings' mechanical loss angles and Young's moduli are taken into consideration.

Thermal noise comes into LIGO sensitivity in two places, the suspensions and the test masses.

- **Thermal noise in suspension**

To reduce seismic noise due to the ground's motion, LIGO test masses are suspended with multiple stages for seismic isolations [44]. Similar to thermal noise in a torsion pendulum, the suspension wires joining each stage also come with thermal noise because of the loss in the wires [45]. Another example of thermal noise measurement in a mechanical flexure suspension can be found in Ref. [46]. Not only the losses in the suspension wires that contribute to the displacement noise, but also the dissipation associated with the whole suspension system, e.g., the magnet-coil actuators, joints between a suspension wire and the test mass, maraging blade springs, gas damping due to residual gas molecules, or electrostatic damping due to currents induced in structures and charges. These noise sources must be minimized to achieve the target sensitivity.

It is worth mentioning that dislocations that cause mechanical losses in materials may also cause displacement noise in the audio band from sub Hz-frequency driving force. This noise, called crackle noise, shows up in other nature phenomena, e.g., earthquakes, or the sound of a

⁶For a comprehensive review of relevant noise sources in Advanced LIGO, see Ref. [42].

crumbling paper. An experiment to test this phenomenon in maraging steel blades is on going at Caltech [47]. The device under test will be driven at sub hertz frequency in order to observe the noise in audio band interferometrically.

- **Thermal Noise in Test Masses**

As the output from the asymmetric port of the beam splitter is directly related to the differential arm lengths, thermal noise in the test masses changes the test mass surfaces' positions and directly couples to the output signal. It is estimated that the sensitivity of Advanced LIGO in the most sensitive band (30 Hz to 300 Hz) will be limited by thermal noise in the high reflective coatings, see Fig. 1.4. Although quantum noise is another dominating noise source that covers the whole measurement bandwidth, it can be reduced below coating thermal noise by frequency dependent squeezed light [48, 49]. The radiation pressure noise at low frequencies can be reduced by amplitude squeezing, while the shot noise limit at high frequencies can be reduced by phase squeezing.

Since coating thermal noise has been identified as an important limiting noise source, research on coatings has rapidly grown. Many groups have developed mathematical models to calculate coating thermal noise [50, 51, 52, 53]. However, due to the coating's multilayer structure and uncertainties in the thin film material parameters (e.g., Young's moduli, Poisson ratios, and loss angles), thermal noise in coatings is not thoroughly understood. For this reason, a test facility, which can measure coating thermal noise with high signal-to-noise ratio across a wide frequency band relevant to Advanced LIGO, is necessary for a comprehensive verification. The setup for this coating thermal noise measurement will be the one of the main topics in this dissertation.

1.2 Direct Observations of Thermal Noise in High Reflective Mirrors

1.2.1 Previous Coating Thermal Noise Measurements

Direct observations of thermal noise in high reflective mirrors were made by Numata et al. and Black et al. [54, 55]. The results, measured between 1 kHz and 10 kHz band, were in good agreement with theoretical predictions. These experiments used four independently suspended mirrors to form two Fabry-Perot cavities that were locked to a frequency stabilized laser and sensed the coating thermal noise via feedback signals to the cavities. The sensitivity of this method, however, is limited by seismic noise at frequencies below 1 kHz, even with the passive seismic isolation of the suspended large test masses (4 inches in diameter, 3 inches thick). Therefore, the noise level between 10 Hz to 300 Hz has yet to be verified experimentally. The measurement will be important for characterizing

Advanced LIGO performance since it is predicted to be limited by coating thermal noise in this bandwidth. Additionally, the setup similar to that of TNI requires larger, heavier substrates to overcome seismic noise for measurements at lower frequencies. Big custom made substrates are expensive for testing several samples. A setup that uses smaller commercially available substrates is preferred. An alternative setup is needed to overcome such issues.

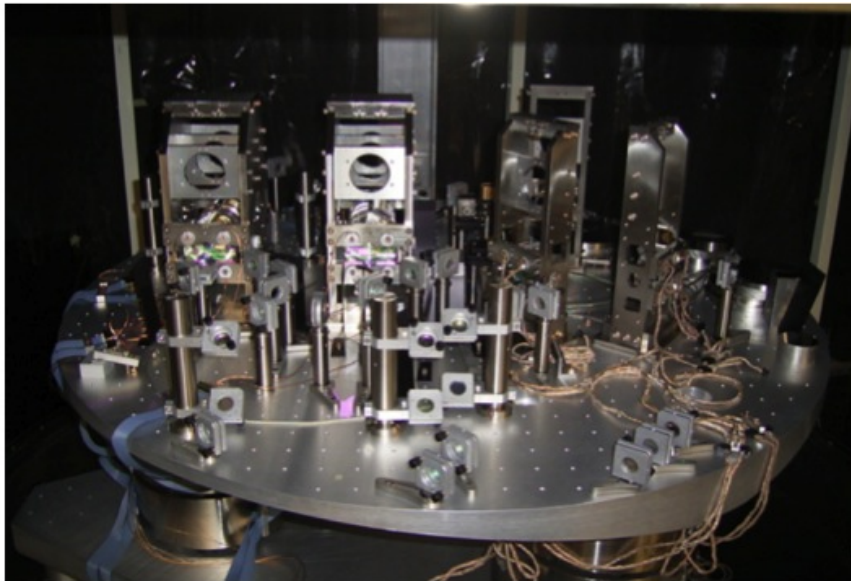


Figure 1.5: Inside of TNI’s main vacuum chamber, ca. 2007. The suspended test masses are on the left, the triangular Mode Cleaner cavity is on the right. Picture credit: Akira Villar

1.2.2 Coating Brownian Noise from Fixed Spacer Fabry–Perot Cavity

In the field of optical frequency metrology, a fixed–spacer Fabry–Perot cavity (see Fig. 1.6) is typically used as a stable reference for locking laser frequency. By designing the shape of the spacer, and searching for vibration insensitive support points, several groups have demonstrated that the total displacement noise of a rigid cavity can be very close to the thermal noise limit from the high mirror coating at frequencies around 0.01 - 1 Hz [56, 57, 58]. However, none have reported Brownian thermal noise in the frequency band relevant to ground based GW detectors.⁷

This motivates us to develop a testbed that can directly observe coating thermal noise in the 10 Hz to 1 kHz bandwidth using fixed spacer Fabry–Perot cavities and standard 1 inch diameter substrates. Fortunately, the spacer does not introduce a lot of excess displacement noise. Thermal noise associated with a spacer made from fused silica is predicted to be much smaller than that in dielectric coatings [59, 60]. More details are discussed in chapter 2.

Another advantage of the fixed spacer setup, besides the lower cost for the samples, is the shorter turnaround time because of commercially available substrates and the less complicated suspension

⁷See the comparison among the experiments in appendix A

system. It takes approximately a month for each set of samples to be installed and measured. In addition, as the measurement can be done optically from the transmitted beams, the calibration is relatively simple (cf. section 4.6) compared to the readout technique used in TNI measurement [55]. Furthermore, an error related to spot size and cavity's length in a fixed-spacer cavity will be less than that of a suspended cavity. Better knowledge on the spot size leads to more accurate coating thermal noise calculation. In the next chapter, thermal noise in all parts of a fixed-spacer Fabry-Perot cavity will be discussed in detail.

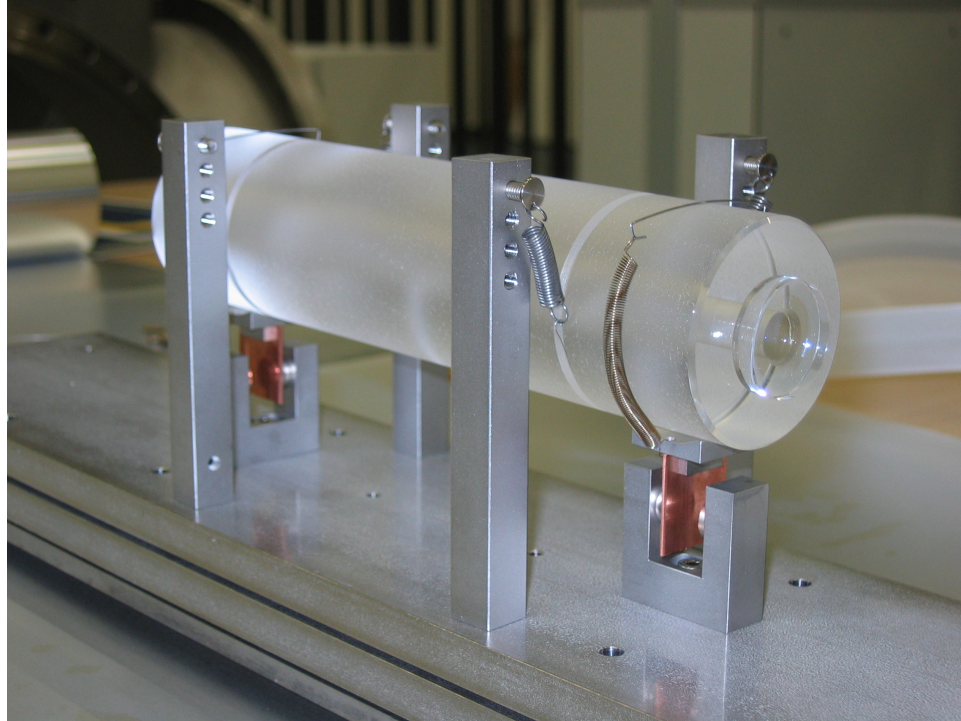


Figure 1.6: An 8 inch reference cavity used in LIGO as a low noise reference cavity, the spacer and mirror substrates are made from fused silica. The cavity is suspended with two spring wires fitted around the Airy point. The eddy current damper can be seen on the top of the plate.

Chapter 2

Thermal Noise in Fixed–Spacer Fabry–Perot Cavity

Typically, a Fabry–Perot cavity consists of three parts: two mirror substrates, high reflective coatings deposited on the substrates, and a spacer with a bore hole along the beam line axis for the beam to propagate in vacuum. The substrates are usually optically bonded to the spacer on both ends, as shown in Fig. 2.1. To use a fixed-spacer Fabry–Perot cavity in a coating thermal noise measurement, all fundamental noises related to the cavity have to be considered.

This chapter will start with the Fluctuation-Dissipation theorem where the coupling between the dissipation and the fluctuation in a system is derived. Then the discussion will move to explain how a Gaussian beam resonating inside the cavity senses thermal noise contributed from each part of the cavity. All assumptions and formulas used to generate the thermal noise contributions will be explained. Numerical values of the relevant parameters and symbols are given in Tab. 2.1. A brief discussion on several efforts to reduce thermal noise is included at the end of the chapter.

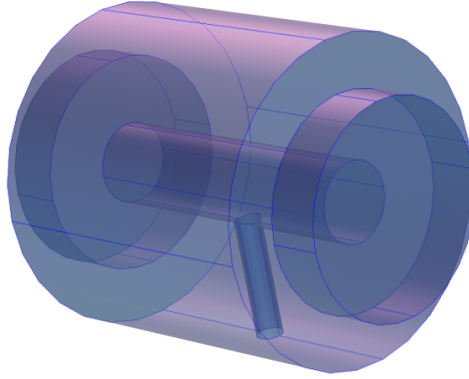


Figure 2.1: Assembly of a 1.45-in spacer used in this dissertation. The substrates are optically contacted on both ends of the spacer. The vent hole for using the cavity in a vacuum system can be seen.

Symbol	Name	unit
f	temporal frequency	Hz
c	light speed in vacuum	m/s
$S_x(f)$	single-sided power spectral density	m^2/Hz
k_B	Boltzmann constant	J/K
T	Mean temperature	K
C	Heat capacity per volume	J/Km^3
κ	Thermal conductivity	W/mK
Y	Young's modulus	N/m^2
σ	Poisson's ratio	
α	Thermal expansion coefficient	$1/K$
β	Thermorefractive coefficient, $\partial n/\partial T$	$1/K$
n	Refractive index	
λ	Beam wavelength	m
ν	carrier frequency	Hz
ω_0	Beam radius ($1/e^2$ power)	m
d	Coating thickness	m
ϕ	Mechanical loss angle	
L	cavity length	m

Table 2.1: Symbols, constants, and material parameters frequently used in this chapter. The subscripts s and c following a parameter will be used to denote a property of the substrate or the coating.

2.1 Fluctuation-Dissipation Theorem

Let's look back to Brownian motion of a particle in water. When the particle is left alone, water molecules randomly and continuously collide with it and move the particle around. On the other hand, if the particle is dragged through the water, these random collisions from the water will act as a frictional force trying to dissipate the particle's kinetic energy. From these two situations, we see that the fluctuation of the particle's position (or velocity) and the dissipation of the particle's energy under the influence of an external force are both caused by the same phenomenon: the collisions with the surrounding water molecules. This implies that the fluctuation and the dissipation are related, as they share the same origin. The coupling between them given by the Fluctuation-Dissipation Theorem (FDT) [61] is ¹

$$S_x(f) = \frac{k_B T}{\pi^2 f^2} \text{Re}[Y(f)], \quad (2.1)$$

where f is Fourier temporal frequency, $Y(f)$ is the mechanical admittance associated with $x(t)$. The admittance can be computed by looking at a generalized force $F(t)$ that drives the system in one of the generalized coordinates, $x(t)$. The admittance is the Fourier transform of the derivative of $x(t)$ divided by the applied force which is

$$Y(f) = \frac{\dot{x}(f)}{F(f)} = \frac{2\pi i f x(f)}{F(f)}. \quad (2.2)$$

Let's see an example in a mass-spring system. A mass m is attached to a spring with spring constant $k(1 + i\phi)$. The equation of motion can be written as

$$F = k(1 + i\phi)x + m\ddot{x}. \quad (2.3)$$

The equation can be transformed to the frequency domain via a Laplace transformation. Rearrange the equation to get,

$$Y = \frac{\dot{x}}{F} = \frac{i\omega}{k - \omega^2 m + ik\phi} \quad (2.4a)$$

$$= \frac{(i\omega)(k - \omega^2 m - ik\phi)}{(k - \omega^2 m)^2 + k^2 \phi^2}, \text{ and} \quad (2.4b)$$

$$\text{Re}[Y] = \frac{k\phi\omega}{(k - \omega^2 m)^2 + k^2 \phi^2}, \quad (2.4c)$$

where $\omega = 2\pi f$. Substituting this back into Eq. 2.1, in the limit of $2\pi f \ll \sqrt{\frac{k}{m}}$ we get

¹A comprehensive review about the Fluctuation-Dissipation can be found in Ref. [62], and an introduction to a modern aspect of the fluctuation-dissipation theorem can be found in Ref. [63]

$$S_x(f) = \frac{2k_B T}{\pi f} \frac{\phi}{k}. \quad (2.5)$$

This equation captures all significant characteristics of thermal Brownian noise. It is directly proportional to the temperature and the loss of the system. It is inversely proportional to the frequency and the stiffness of the material (spring constant). In general, ϕ can be frequency and temperature dependent.

2.2 Direct Approach

Thermal noise in a beam-optic system is not as simple as the mass-spring example. Previous calculations to determine thermal noise were done by a modal expansion, for example, in a suspension system [64], or in a mirror of a laser interferometer gravitational-wave detector [65]. This method calculates the admittance and sums up contributions from all vibration modes contributing to the strain of the system. However, it is computationally expensive, complicated, and the result is not guaranteed to converge [66]. Additionally, this method cannot handle non-uniform loss in the substrate. The dielectric coatings turn out to be more lossy than the mirror substrate. As the coating is closer to the beam than the substrate, its effect contributes to the surface fluctuation even more. Instead of using modal expansion, one can use the so-called “direct approach” to compute $\text{Re}[Y(f)]$. This was introduced by González and Saulson [67] for computing thermal noise in suspensions, and was later applied to a laser mirror by Levin [66]. In this approach, one calculates the thermal noise by applying a cyclic force which causes power dissipation in a lossy system. With the FDT, the dissipated power W_{diss} and the PSD S_x are related by

$$S_x(f) = \frac{2k_B T}{\pi^2 f^2} \frac{W_{\text{diss}}}{F_0^2}, \quad (2.6)$$

where F_0 is the magnitude of the applied force to calculate the dissipated power. In the case of mirror whose position is interrogated by a laser beam, the cyclic “force” applied is a pressure with the same profile as the intensity of the beam.

2.3 Two Kinds of Thermal Noise

As we can see from Eq. 2.6, any dissipation due to the applied force creates thermal noise in a system. For a solid system, there are two known sources of dissipation: mechanical loss and thermal dissipation. Mechanical loss is caused by impurities or dislocations in the material, and displacement noise associated with this mechanism is usually referred to as Brownian noise. Thermal dissipation, often called Zener damping [68], occurs due to irreversible heat flow down temperature gradients

which create temperature fluctuations in a system.

2.3.1 Brownian Thermal Noise

Mechanical loss arises from the internal structure of a material, such as impurities or dislocations [69]. It is represented by introducing an imaginary part to the Young's modulus of the material: $E = E_0(1 + i\phi)$. The quantity ϕ is referred to as the *loss angle*, and may be temperature and frequency dependent. When a sinusoidal force is applied to a system subject to mechanical loss, the dissipated power due to the applied force is given as [66]

$$W_{\text{diss}} = 2\pi f U_0 \phi, \quad (2.7)$$

where U_0 is the maximum energy of elastic deformation. The loss angle ϕ is equal to $1/Q$, where Q is the quality factor. In general, Q can be measured from a ring down measurement: an amplitude of an oscillation with resonant frequency f_0 decays over time as $A(t) = A(0)\text{Exp}[i2\pi f_0 t]\text{Exp}[-t\pi f_0/Q]$.

If one is interested only in frequencies f below the first mechanical resonance frequency of the system (as is the case with our reference cavities), it is sufficient to compute the stored energy U_0 in the presence of a static force. The problem of evaluating W_{diss} then reduces to a single elastostatic computation, which can be carried out with finite element analysis (FEA) if necessary. Together with Eq. 2.6, one can then calculate the Brownian contribution to the apparent position fluctuation of the mirror as sensed by a laser beam interrogating the mirror surface.

2.3.2 Thermodynamic Noise

In contrast to Brownian noise, thermo-optic noise is related to thermal, rather than mechanical, dissipation; it arises from fluctuations in the temperature field $T(\mathbf{r}, t)$ throughout the mirror [70]. In classical solid state thermodynamics, these fluctuations are not correlated with the volume fluctuations driven by Brownian noise. The two effects have to be summed incoherently.

In general, for a volume V , the total variance of temperature fluctuations can be described by [71]

$$\langle \delta T^2 \rangle = \frac{k_B T^2}{CV}. \quad (2.8)$$

With non-zero thermal expansion α , and thermorefractive β , in coatings, a mirror and a spacer, the thermal fluctuation is converted into displacement noise or phase noise as the beam is reflected off of the mirror surface.

To compute thermo-optic noise using the direct approach, one can apply either an imaginary force [52, 72] or imaginary heat [73, 74] to the mirror's surface; the results will be the same if the stress inside the coating is uniform [52]. The applied force will cause temperature gradients inside

the mirror through the equation of static stress balance [75]

$$\nabla(\nabla \cdot \mathbf{u}) + (1 - 2\sigma)\nabla^2 \mathbf{u} = -2\alpha(1 + \sigma)\nabla\delta T, \quad (2.9)$$

where \mathbf{u} is the displacement vector of the mirror body due to the applied pressure. Then, the temperature perturbation evolves according to the thermal diffusion equation as [75]

$$\frac{\partial(\delta T)}{\partial t} - \frac{\kappa}{C}\nabla^2(\delta T) = \frac{-\alpha Y T}{C(1 - 2\sigma)} \frac{\partial(\nabla \cdot \mathbf{u})}{\partial t}. \quad (2.10)$$

Finally, the power dissipation due to the heat flow caused by the temperature gradient is given by the expression [75, Eq. 35.1]

$$W_{\text{diss}} = \left\langle T \frac{dS}{dt} \right\rangle = \left\langle \int d^3r \frac{\kappa}{T} (\nabla\delta T)^2 \right\rangle. \quad (2.11)$$

Here T is the unperturbed temperature of the system and δT is the temperature perturbation due to the applied force F_0 . The entropy S of the system changes due to the heat flux $-\kappa\nabla(\delta T)$, and the angle brackets denote an average over the period of oscillation of the force. By substituting Eq. 2.11 into Eq. 2.6, we can obtain the temperature fluctuation on the mirror sensed by a Gaussian beam. This fluctuation couples into the electromagnetic response of the mirror via α and β .

In the literature, the term ‘‘thermoelastic noise’’ refers to physical displacement noise of the mirror’s surface position due to thermal expansion of the substrate and the coating [76, 72, 77, 78]. In a beam-optic system, the change of the mirror position causes the phase shift of the reflected beam. On the other hand, ‘‘thermorefractive noise’’ refers to the phase fluctuation of the beam as it propagates through or reflects off the mirror (the path length of the beam changes even though the mirror surface position is fixed), and it is a combined effect of both α and β . This is a slight misnomer, and it will be emphasized again. Since both thermoelastic and thermorefractive noises arise from a common origin, they are computed in a coherent fashion and the combined effect is called thermo-optic noise [74].

2.4 Thermal Noise in Substrate

A substrate is the bulk of a mirror on which the coating is deposited. In a Fabry–Perot topology, the light goes through the input substrate, and bounces back and forth on the surfaces before leaving the end substrate. The displacement noise on the substrate from both Brownian noise and thermoelastic noise will change the cavity length. Thermo-optic effects in the substrate will be negligible compared to the other two. We will start the discussion with the substrate because of its relative simplicity compared to that of the coating.

2.4.1 Brownian Noise in Substrate

By using the direct approach, Brownian noise from a substrate as sensed by a Gaussian beam is given as [66],

$$S_x(f) = \frac{2k_B T}{\pi^{3/2} f} \frac{1 - \sigma_s^2}{w_0 Y_s} \phi_s. \quad (2.12)$$

The result here is obtained from a half-infinite model, where the spot size is much smaller than the mirror size. Corrections for a finite size mirror are given in Ref. [72]. For our case, where spot sizes will be on the order of 200-300 μm , with 1 inch diameter and 0.25 inch thick substrates, the correction is negligible.

2.4.2 Thermoelastic Noise in Substrate

For Initial LIGO, the test masses were made of fused silica. In hopes of improving the sensitivity of the detector, scientists had proposed to switch test masses' material from fused silica to sapphire due to its lower mechanical loss. However, Braginsky et al. [76] pointed out that thermoelastic noise had to be taken into consideration. As a result, a sapphire substrate was predicted to have higher total thermal noise than that of a fused silica substrate.

For the case of a half-infinite substrate in the adiabatic limit $l_{th} \ll w_0$, where $l_{th} = \sqrt{\kappa_s / (2\pi C_s f)}$ is the thermal diffusion length at frequency f , and κ_s and C_s are, respectively, the thermal conductivity and the heat capacity per unit volume of the substrate, thermoelastic noise in substrate can be expressed as

$$S_x^{TEsub}(f) = \frac{4k_B T^2 \alpha_s^2 (1 + \sigma_s)^2 \kappa_s}{\sqrt{\pi^5} C_s^2 w_0^3 f^2}. \quad (2.13)$$

Later, a non-adiabatic correction for low frequencies and small beam sizes was computed by Cerdonio et al. [77, Eq. 20], with some minor corrections as stated in Ref. [54, 79] :

$$S_x^{(subTE)}(f) = \frac{4k_B T^2}{\sqrt{\pi}} \frac{\alpha_s^2 (1 + \sigma_s)^2 w_0}{\kappa_s} J(f/f_T), \quad (2.14)$$

where $f_T = \kappa_s / \pi w^2 C_s$, and $J(f/f_T)$ is a non-elementary function whose asymptotes are $2 / (3\sqrt{\pi f/f_T})$ for $f/f_T \ll 1$ and $1 / (f/f_T)^2$ for $f/f_T \gg 1$; the full expression is

$$J(f/f_T) = \left(\frac{2}{\pi}\right)^{1/2} \int_0^\infty du \int_{-\infty}^\infty dv \frac{u^3 e^{-u^2/2}}{(u^2 + v^2)[(u^2 + v^2)^2 + (f/f_T)^2]}. \quad (2.15)$$

At $f \gg f_T$, or in the adiabatic limit, Eq. 2.14 reduces to Eq. 2.13. The simplified equation presents how thermoelastic noise level changes explicitly with the spot size and frequency.

An experiment at the TNI measured thermoelastic noise in sapphire mirror at room tempera-

ture [79], and found a good agreement with the theoretical calculation, showing that sapphire, even with lower mechanical loss than that of fused silica, has a higher total noise level due to thermoelastic noise.

2.4.3 Thermo–Optic Noise in Substrate

In a Fabry–Perot cavity topology, the beam passes through each substrate only once. Hence, thermo–optic noise in the substrate is usually much smaller than other thermal noise in the cavity. An analytical result for thermo–optic noise in a finite–sized cylindrical substrate sensed by a Gaussian beam is given in Ref. [80]. The frequency noise on the signal due to this effect is on the order of $10^{-7} Hz/\sqrt{Hz}$ which will be negligible for our setup.

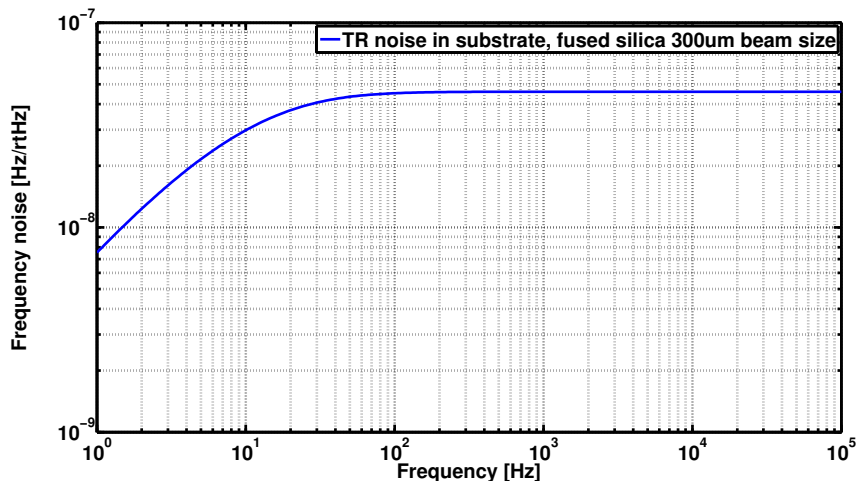


Figure 2.2: Frequency noise of the beam passing through a quarter inch thick fused silica substrate. It is negligible compared to other noise source as shown in Fig. 3.5 and Fig. 3.9.

Note that the “thermo–optic” noise calculation in Ref. [80] only takes the phase noise due to β ($\partial n/\partial T$) into account (it is also called *thermorefractive* noise in the original paper). In reality, the optical path of the output beam is also changed by thermal expansion of the substrate due to the temperature change. For example, see the calculation for thermal noise in optical fiber where the thermal noise from β and α in fiber optic are calculated coherently [81]. By using $\beta + n\alpha$ instead of just β , the effect from thermal expansion will be included. As the calculation here includes the contribution from α , the effect is called thermo–optic noise. For fused silica, the effect will not be altered by much because the contribution from thermal expansion is an order of magnitude smaller.

2.5 Thermal Noise in Coatings

One of the most important conclusions derived from the direct approach calculation is that the loss from the reflecting surface contributes to the noise significantly [66]. As a result, attention shifted to study more about the dielectric coatings. The coatings are usually more lossy than the bulk substrate, so they are expected to have higher thermal noise. Additionally, because of the multilayer structure and how light interacts within the coatings, thermal noise inside the coatings becomes more complicated, as we will see in this section.

2.5.1 Brownian Noise in Coatings

Brownian thermal noise in a thin film on a half-infinite substrate can be expressed as [50]

$$S_x^{(\text{cBR})}(f) = \frac{4k_B T}{\pi^2 f} \frac{(1 + \sigma_s)(1 - 2\sigma_s)}{E_s} \frac{d}{w_0^2} \phi_c, \quad (2.16)$$

where d is the total thickness of the coating, and ϕ_c is the coating's loss angle.

This equation assumes that the elastic properties of substrate and the thin coating are the same, and that all the coating properties are isotropic. Due to the multilayer structure of the amorphous materials, the coating loss and elastic properties may be anisotropic. For this reason, authors such as Harry et al. [51] decompose coating loss and elastic deformation into parallel (\parallel) and perpendicular (\perp) directions relative to the mirror normal. Then, in accordance with Eq. 2.7, the total dissipated energy can be written as $W_{\text{diss}} = 2\pi f(U_{\perp}\phi_{\perp} + U_{\parallel}\phi_{\parallel})$. The stored elastic energy U_{\perp} and U_{\parallel} can be calculated in the cylindrical coordinate. The spectral density is given as

$$\begin{aligned} S_x^{\text{coating}}(f) = & \frac{2k_B T}{\pi^2 f} \frac{1 - \sigma^2}{\omega_0^2 Y} \times \frac{d}{Y Y_c (1 - 2\sigma_c)(1 - \sigma^2)} \\ & \times \left\{ Y_c^2 (1 + \sigma)^2 (1 - 2\sigma)^2 \phi_{\parallel} \right. \\ & + Y Y_c \sigma_c (1 + \sigma)(1 + \sigma_c)(1 - 2\sigma)(\phi_{\parallel} - \phi_{\perp}) \\ & \left. + Y^2 (1 + \sigma_c)^2 (1 - 2\sigma_c)^2 \phi_{\perp} \right\}. \end{aligned} \quad (2.17)$$

This equation assumes that the coating's Young's modulus is isotropic: the modulus is the same in both parallel and perpendicular directions. In the case $Y_c = Y$, $\sigma_c = \sigma$ and $\phi_{\perp} = \phi_{\parallel}$, Eq. 2.17 agrees with Eq. 2.16.

For coatings with multiple layers of high and low refractive index materials, Young's moduli and Poisson's ratios have to be averaged (this is similar to the calculation of connected springs) and

Eq. 2.17 can be rewritten as [82]

$$S_x^{coating}(f) = \frac{2k_B T}{\pi^2 f} \frac{1 - \sigma^2}{\omega_0^2 Y Y_\perp} \times d \times \left\{ \left(\frac{Y}{1 - \sigma_\perp} - \frac{2\sigma_\parallel^2 Y Y_\parallel}{Y_\perp (1 - \sigma^2)(1 - \sigma_\parallel)} \right) \phi_\perp + \frac{Y_\parallel \sigma_\parallel (1 - 2\sigma)}{(1 - \sigma_\parallel)(1 - \sigma)} (\phi_\parallel - \phi_\perp) + \frac{Y_\parallel Y_\perp (1 + \sigma)(1 - 2\sigma)^2}{Y(1 - \sigma_\parallel^2)(1 - \sigma)} \phi_\parallel \right\}, \quad (2.18)$$

with averaged coatings parameters:

$$Y_\perp = (d_1 + d_2) / \left(\frac{d_1}{Y_1} + \frac{d_2}{Y_2} \right), \quad (2.19a)$$

$$Y_\parallel = \frac{Y_1 d_1 + Y_2 d_2}{d_1 + d_2}, \quad (2.19b)$$

$$\sigma_\perp = \frac{\sigma_1 Y_1 d_1 + \sigma_2 Y_2 d_2}{Y_1 d_1 + Y_2 d_2}, \quad (2.19c)$$

$$\phi_\perp = Y_\perp \left(\frac{\phi_1 d_1}{Y_1} + \frac{\phi_2 d_2}{Y_2} \right), \quad (2.19d)$$

$$\phi_\parallel = \frac{Y_1 \phi_1 d_1 + Y_2 \phi_2 d_2}{Y_\parallel (d_1 + d_2)}, \quad (2.19e)$$

where subscripts 1 and 2 refer to the two coating materials. For σ_\parallel the equivalent equation is more complicated. In general, an averaged values between σ_1 and σ_2 is good within 5%.

However, as argued by Hong et al. [53], ϕ_\perp and ϕ_\parallel are not a suitable choice to be consistently used as the loss angles of a material, since the corresponding energies U_\perp and U_\parallel can be negative in certain cases. Instead, W_{diss} should be decomposed into bulk (“B”) and shear (“S”) contributions: $W_{\text{diss}} = 2\pi(U_B \phi_B + U_S \phi_S)$. If the effect of the light propagating inside the coating layers is omitted, the power spectral density for a duplex structure of material with high reflective index and low refractive index can be written as,

$$S_x^{coatBR} = q_H^B S_H^B + q_H^S S_H^S + q_L^B S_L^B + q_L^S S_L^S, \quad (2.20)$$

with

$$S_j^X = \frac{4k_B T \lambda_j \phi_X^j (1 - \sigma_j - 2\sigma_j^2)}{3\pi^2 f Y_j (1 - \sigma_j)^2 \omega_0^2}, \quad X = B, S, \text{ and } j = H, L \quad (2.21)$$

The subscripts H and L denote the material with high and low indices respectively, while the superscripts B and L denote the bulk and shear modes.

For SiO₂/Ta₂O₅ coatings, the individual loss angles (either ϕ_\perp and ϕ_\parallel , or ϕ_B and ϕ_S) are not well known, and knowledge of the individual material properties is also limited. These uncertainties

will propagate forward toward the estimate of the loss angle [53].

It is remarkable that if we assume that $\phi_B = \phi_S$, and elastic parameters of the substrate and those of the coating are the same, then the results of Harry et al. [51] and Hong et al. [53] reduce to Eq. 2.16.

In any case, since there is no fundamental reasons for the assumptions, the “coating loss angle” ϕ_c as defined in Eq. 2.16 should be viewed not as a physical parameter, but as a figure of merit which is related to the various loss angles and material parameters of each coating material.

More details about Brownian noise in coating with finite size substrate is done in Somiya and Yamamoto [52]. Although the loss angles are assumed to be isotropic in the coatings, this mathematical treatment explains how the finite size causes the noise level to increase. For our case, the spot size is usually much smaller than the substrate, and the finite size correction is negligible.

2.5.2 Thermo–Optic Noise in Coatings

The term thermo–optic noise includes two effects that occur in the coating, thermoelastic noise and thermorefractive noise. Each noise was calculated independently [78, 83, 84]. Later, when scientists realized that both effects originated from the same temperature fluctuation, they were computed coherently [74].

Thermoelastic Noise in Coatings

Temperature fluctuations in coatings directly change the position of the mirror surface via thermal expansion coefficient. As the coating expands, the total length of the cavity contracts. This is very similar to thermoelastic noise in substrate discussed in section 2.4.2.

Thermorefractive Noise

For a highly reflective mirror with multilayer dielectric coatings used in an interferometric measurement, the output phase of the beam reflected from the mirror carries information about the mirror position. However, not all of the electric field of the beam just reflects off the top surface of the mirror. A certain amount of electric field propagates inside the coating layers and reflects off from every coating interface. Ideally, for a quarter wavelength design, all the reflected beams will interfere constructively at the air-coating surface, see Fig. D.1. Because of the non-zero thermo refractive coefficient, the temperature fluctuation adds the random path length in each layer, resulting in the phase noise summed up at the total reflected beam. Even though the surface position is kept stationary, the reflected phase is still varied due to the thermorefractive mechanism resulting in the displacement noise on the mirror surface as interpreted by the probe beam.

It should be emphasized that the term “thermorefractive” used in this context refers to the mechanism that alters the optical path length inside the coatings. As the temperature changes, not only $\partial n/\partial T$ that changes the optical path length of the beam propagating inside the layers, but also α , as seen in Eq. D.8 which is taken from **B15** of Ref. [74].

Thermo-optic Noise in Coatings: The Combined Effect

Since both thermoelastic noise and thermorefractive noise originate from the same thermal fluctuations inside coatings, the effects are summed coherently, and called thermo-optic noise. The calculation is done by injecting Gaussian profile heat (entropy) on the mirror then calculating the heat flow loss [73]. Then the FDT is applied to relate loss to the spectral density of noise in temperature. Finally, the temperature fluctuation is converted to displacement noise and phase noise via the thermoelastic coefficient and the thermo refractive coefficient. The unified result is [74]

$$S_x^{TO}(f) = S_{\Delta T}^{TO}(f)\Gamma_{tc} \left(\bar{\alpha}_c d - \bar{\beta}\lambda - \bar{\alpha}_s d \frac{C_c}{C_s} \right)^2, \quad (2.22)$$

and

$$S_{\Delta T}^{TO}(f) = \frac{2}{\pi^{3/2}} \frac{k_B T^2}{\omega_0^2 \sqrt{\kappa C f}}, \quad (2.23)$$

where $\bar{\alpha}_c$ and $\bar{\beta}$ are the effective thermal expansion coefficient of the coating and the effective thermorefractive coefficient respectively. Their full expressions are shown in Appendix D.

$S_{\Delta T}^{TO}(f)$ is the power spectrum of the coating thermal fluctuations sensed by a Gaussian beam. The parameters used in that factor are those of substrate, whereas the contribution from the coatings are included in the thick coating correction Γ_{tc} . The calculation above uses the adiabatic-assumption, where δT in the material due to the applied heat does not flow in or out in the orthogonal direction (thermal diffusion length $l_{th} \ll$ spot size w_0) and solves the heat equation in 1 dimension along the beam line direction [84, 73, 74]. However, this is not true at low frequency, or when the spot size becomes comparable to the thermal length. At such regimes, the heat flow in the orthogonal direction becomes large, causing $\nabla\delta T$ to be smaller and the noise is overestimated. The correction for small spot size-low frequency regime is done in Ref. [27], by extending the calculation from Braginsky et al. [84]. The outline for mathematical derivation is shown in appendix G. Hence, in the general case, the temperature fluctuation sensed by a Gaussian beam is

$$S_{\Delta T}^{TO}(f) = \frac{2\sqrt{2}k_B T^2}{\pi\kappa\omega_0} K(\Omega) \quad (2.24)$$

with

$$K(\Omega) = R \left[\int_0^\infty du u e^{-\frac{u^2}{2}} \frac{\sqrt{u^2 + i\Omega}}{\sqrt{u^4 + \Omega^2}} \right] \quad (2.25)$$

The correction is conceptually similar to what is done in Ref. [77] for thermoelastic noise in the substrate. However, the thick coating correction Γ_{tc} from Ref. [74] treats the heat flow in the coating only in the beam line direction and must be modified. To my knowledge, the correction where the heat flow in the coating is solved in 3 dimensions does not exist in the literature yet. This will lead to some error in the thermo optic noise estimation for materials like AlGaAs coatings where l_{th} can

be quite large compared to the spot size, see Tab. 2.2.

Parameters	<i>SiO₂</i> Substrate	<i>SiO₂/Ta₂O₅</i> QWL	optimized AlGaAs
Thermal conductivity, κ [W/mK]	1.38	2.23	61.5
Heat capacity, C [J/m ³] $\times 10^6$	1.63	1.82	1.72
Thermal diffusion length, l_T , $\sqrt{\frac{\kappa}{C2\pi f}}$ [μm]	$37 \sqrt{\frac{100\text{Hz}}{f}}$	$44 \sqrt{\frac{100\text{Hz}}{f}}$	$238 \sqrt{\frac{100\text{Hz}}{f}}$
beam radius, ω_0 [μm]	-	182-292	215
coating thickness, d , [μm]	-	4.5	4.6

Table 2.2: Some parameters for TO noise calculation. Parameters in QWL and optimized AlGaAs columns are averaged based on the coating structure and the material parameters. QWL here is a 27 layer quarter wave thickness stack with a half wave cap of SiO₂ on top (a total of 28 layers). The Optimized structure for AlGaAs can be found in chapter 5.

2.6 Thermal Noise in Spacer

2.6.1 Brownian Noise in Spacer

Another part of a fixed-spacer Fabry–Perot cavity that has thermal noise is the spacer. Brownian noise in spacer was first calculated by Numata et al. [59] and later refined by Kessler et al. [60] with the effect of the size of the bore hole along the spacer length.

$$S_x^{spacer}(f) = \frac{4k_B T}{\pi f} \frac{L}{2\pi(R^2 - r^2)Y} \phi_{spacer} \quad (2.26)$$

Where R is the radius of the spacer, r is the bore hole radius, and L is the length of the spacer. However, the analytical result assumes that the mirror and the spacer have the same outer radii and are fully attached together. Typically, the mirror radius is smaller than that of the spacer, and the contact area is only an annulus with thickness around 2 mm, see Fig. 2.3. To calculate the effect correctly, a finite element analysis (FEA), by COMSOL, is used together with the direct approach. By computing the elastic energy stored in the body of the spacer, the displacement noise in spacer can be calculated. First, the FEA result where the force is applied on the whole surface area of the spacer is compared with the analytical result in Eq. 2.26. Both results agree well within 2%. Once the model is verified, the contact surface is changed to match the real situation, see Fig. 2.3, and

the elastic energy is calculated. The dependence of spacer Brownian noise on the size of the contact surface is shown in Fig. 2.4. The smaller area creates more elastic energy and increases the thermal noise level. This explains why the analytical model which assumes the full mirror-spacer contact area underestimates the noise level.

For a fused silica spacer, its Brownian noise will be smaller than the coating noise by at least an order of magnitude.

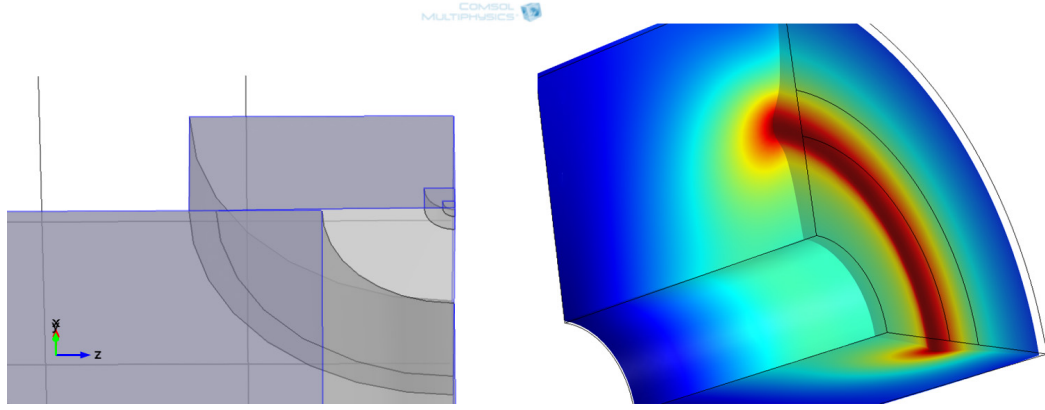


Figure 2.3: COMSOL model for thermal noise calculation. Left, 1/8 of the model is used with symmetric boundary condition on three planes to reduce the computation time. Since most of the deformation will occur close to the applied force, to further minimize the calculation time, only the small volume at the center of the mirror has very fine mesh size while the mesh size is larger far away from the beam. Right, the deformation on the spacer because of the applied force on the mirror contacted on the spacer (not shown), and the elastic energy in the spacer can be calculated.

2.6.2 Thermoelastic Noise in Spacer

To estimate the level of thermoelastic noise in the spacer, one can follow the method outlined by Liu and Thorne [72]:

$$S_x^{(\text{spTE})}(f) = \frac{2k_B T}{\pi^2 f^2} \kappa_{sp} T \left[\frac{Y_{sp} \alpha_{sp}}{(1 - 2\sigma_{sp}) C_{sp}} \right]^2 \int \frac{[\nabla(\nabla \cdot \mathbf{u})]^2}{F_0^2} d^3 r, \quad (2.27)$$

where $\mathbf{u}(\mathbf{r})$ is the displacement field of the spacer in response to a static pressure of total force F_0 applied to the mirror faces. The subscript sp denotes the material parameters of the spacer. For our case, the spacer is made from fused silica similar to the substrates.

We use the same FEA model as described above for computing the spacer Brownian noise to evaluate the integral in Eq. 2.27. The calculation is performed under the adiabatic assumption, since the diffusion length l_{th} is much smaller than the width of the contact area between the spacer and the mirror. Due to the thickness of the annulus (≈ 2 mm), the assumption $l_{th} \ll \omega_0$ should be valid down to a few millihertz. At very lower frequencies, where the assumption on l_{th} is not satisfied, the expected thermoelastic noise is smaller than the adiabatic prediction [77].

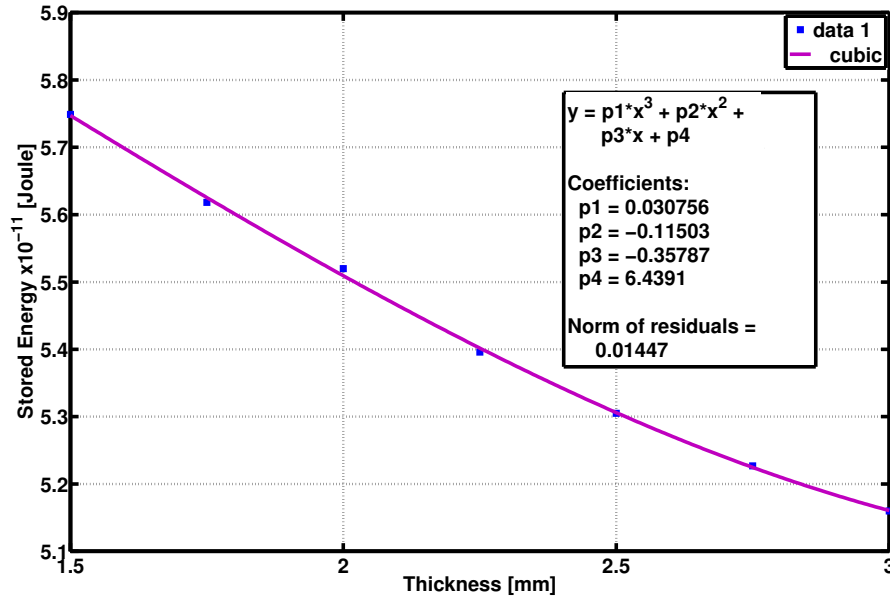


Figure 2.4: Maximum elastic energy due to the applied pressure in 1/8 of the cavity vs the annulus thickness. The outer radius of the annulus is fixed at 0.5 inch which is the radius of the mirror. The fit parameters are shown in the plot. The cavity is 1.45 inch long, with outer and inner radii of 0.75 inch and 0.1875 inch, respectively

To validate the result from FEA, the model is used to calculate thermoelastic noise in substrate. This is done by applying a force with Gaussian profile on the mirror and solving Eq. 2.27 only in the substrate domain. The FEA result agrees well with the adiabatic calculation within 20 percent. It is certain that both Brownian thermal noise and thermoelastic noise in the spacer will not be a limiting noise source in our cavities.

2.7 Photothermal Noise: Absorption from Shot Noise and Intensity Noise

Fluctuation in laser power from shot noise, classical intensity noise, or squeezed light, induces a local temperature change in both coatings and substrate because of the absorption on the mirror. Due to the thermal expansion and thermorefractive coefficients of the mirror substrate and the coating, the temperature gradient caused by the absorbed laser power couples into cavity's displacement noise, and this is called photothermal noise. Similar to thermo-optic noise, the effect in the substrate is mostly thermoelastic. This noise source was first considered in a restricted regime by Braginsky

et al. [76], and later refined for small beam size and low frequencies, can be written as [77]

$$S_x^{(\text{PT})}(f) = \frac{2}{\pi^2} \frac{(1 + \sigma_s)^2}{\kappa_s^2} \mathcal{S}_{\text{abs}} K(f/f_T), \quad (2.28)$$

where

$$K(f/f_T) = \left| \frac{1}{\pi} \int_0^\infty du \int_{-\infty}^\infty dv \frac{u^2 e^{-u^2/2}}{(u^2 + v^2)(u^2 + v^2 + if/f_T)} \right|^2, \quad (2.29)$$

and

$$\mathcal{S}_{\text{abs}} = \delta P(f) \frac{2\mathcal{F}/\pi}{1 + (f/f_{\text{cav}})^2} \chi_{\text{abs}}, \quad (2.30)$$

where \mathcal{F} is the finesse of the cavity, $\delta P(f)$ is the input power fluctuation, χ_{abs} is an absorption coefficient of the mirror, and $f_{\text{cav}} = f_{\text{FSR}}/(2\mathcal{F})$ is the cavity pole.

The effects from the coating (both thermoelastic and thermorefractive effects) were later included in the work of Farsi et al. [85], who treated all the contributions from substrate and coating coherently. The effect can be measured directly by modulating the power of the laser and observing the displacement noise of the cavity. The results are complicated and will not be repeated here.

Generally, classical intensity noise in a laser is much higher than the shot noise limit. The relative intensity noise due to shot noise is

$$\frac{\delta P}{P} = \frac{\sqrt{2h\nu P}}{P} = 2 \times 10^{-8} \left[\sqrt{\frac{1mW}{P}} \right] \frac{1}{\sqrt{Hz}}, \quad (2.31)$$

where h is the Planck's constant. On the other hand, other sources of power fluctuations in a laser are relaxation oscillations, power fluctuations in the pump laser, and beam pointing fluctuations². A measurement of the relative intensity noise due to these classical effects usually range from 1×10^{-6} to $1 \times 10^{-3} \frac{1}{\sqrt{Hz}}$ between 0.1 Hz and 10 kHz. Since they can be suppressed with intensity stabilization servo (ISS), we will revisit the issue in section 4.7, during technical noise discussion.

2.8 Noise in the Bonding between a Mirror and a Spacer

For a fixed-spacer Fabry-Perot cavity, the interfaces between the spacer and the mirrors are another parts that might introduce displacement noise as well. The level of the noise highly depends on the bonding method. Several bonding methods, for example, epoxy, hydroxide bonds, or optical contact

²When the beam is directed to a reference cavity, the misaligned beam leads to fluctuations in the power coupled into the cavity. For example, power fluctuations due to beam translation dx , and the angular tilt $d\alpha$ can be approximated as [86]

$$\frac{\delta P}{P} \approx \exp \left[\left(\frac{dx}{w_0} \right)^2 + \left(\frac{d\alpha}{\Theta_D} \right)^2 \right], \quad (2.32)$$

where w_0 is the spot size, and $\Theta_D = \lambda/\pi w_0$. Several causes of pointing fluctuations are thermal lensing, vibrations and thermal expansion on opto-mechanical components and thermal lensing.

can be used to make a fixed-spacer cavity. For this experiment, noises associated with the bond has to be low, so the signal from the coating thermal noise is not masked. Plus, the bond has to be vacuum compatible since the cavities are placed in a vacuum chamber. The simplest solution is to optically contact the pieces together. It required no bonding agents, and, if executed correctly, has no noise associated with the bond as the assembly becomes a monolithic piece [87].

2.8.1 Optical Contact

When two objects with flat surfaces are brought to contact, intermolecular force, i.e., van der Waals force becomes large enough to keep the two objects together. In general, different kind of materials can also be bonded [88]. As time goes by, the van der Waals bonds (hydroxyl bonds) turn into covalent bonds (siloxane bonds) making the bond stronger, see Fig. 2.5. Annealing can help accelerating the process. However, care should be taken when the object is heat up or cooled down. The thermal expansion might bend the objects, especially, if the attached pieces are of different material with unequal thermal expansion coefficients, causing a rip in the joint-surfaces that breaks the bond. For this reason, optical contact may not be the most suitable solution for bonding objects used in a space project, (e.g., LISA³), where a large thermal change occurs. Nevertheless, optical contact is still proved to have the lowest noise compared to other bonding methods [89]. More details about how to optically contact a mirror to a spacer can be found in appendix E.2.

In this experiment, all the cavities were assembled by optical contact. As discussed above, noise in the optical bonds are assumed to be negligible as the spacer and the mirror become monolithic. Furthermore, from the direct approach calculation, the beam is far away from the bonding area, and its noise contribution should be negligible. This assumption, as shown in the measurement results in the next chapter, is consistent with the experimental results.

2.8.2 How to Measure Mechanical Loss in Optical Contact

To measure noise introduced by the optical contact, we can use a setup similar to the setup for measuring loss in KOH bond [90]. First, we measure a mechanical loss from a control sample with length L . Then we can compare it with the mechanical loss of a test sample, which is formed by optical contacting two pieces with length ΔL and $L - \Delta L$. Since we want to measure the loss associated with perpendicular direction of the bonded surface, the measurement must be done on longitudinal modes. The first longitudinal mode will have a node at the center of the rod, so, in general, ΔL should be shorter than $L/2$. The thickness of the bond can be determined by the surface grinding specification or it can be measured by optical scattering from the surface [91]. Once the mechanical loss is determined, the loss per area can be estimated and applied to the cavity-substrate

³<http://lisa.nasa.gov>

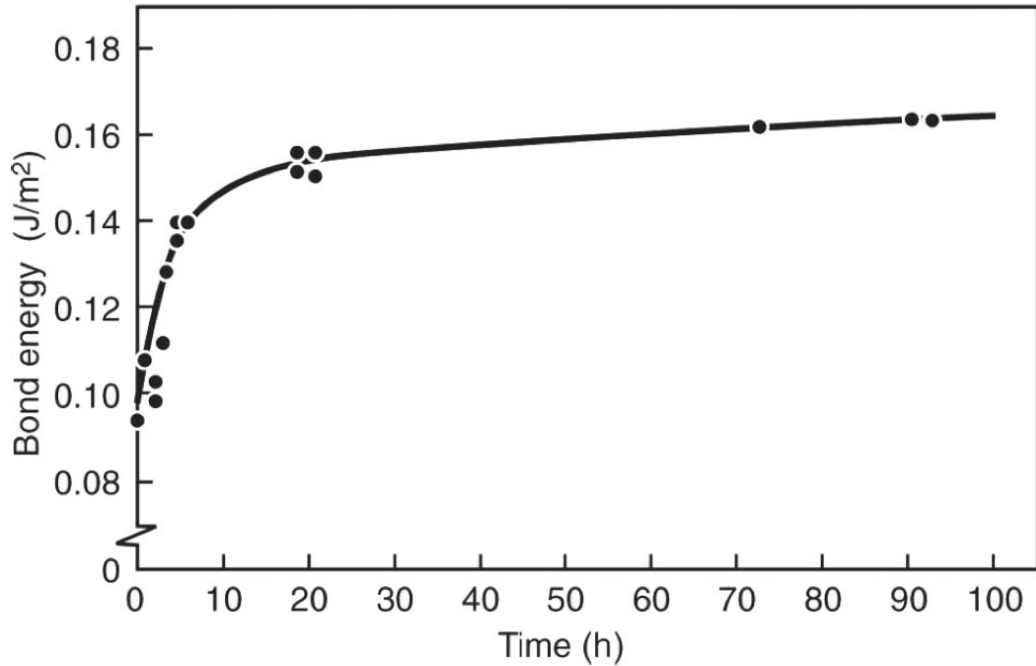


Figure 2.5: Measured bond energy vs time after optical bonding: The bond strengthens as time passes and more van der Waals bonds become covalent bonds. This settling process might take up to several days [87].

situation.

2.9 How to Reduce Thermal Noise

From the discussion above, thermal noise sensed by a Gaussian beam on a dielectric mirror has been explained. For fused silica/tantala coatings, coating Brownian noise will be the dominating noise. Let's look at Eq. 2.16 again,

$$S_x^{(\text{cBR})}(f) = \frac{4k_B T}{\pi^2 f} \frac{(1 + \sigma_s)(1 - 2\sigma_s)}{E_s} \frac{d}{w_0^2} \phi_c. \quad (2.33)$$

This simplified formula captures all significant parameters contributing to coating thermal noise. To reduce thermal noise, we can either decrease the temperature T , reduce loss in the coating ϕ_c , or increase the spot size w_0 . Most methods evolving around these concepts are explained below.

2.9.1 Lower Temperature

As thermal noise is driven by the ambient temperature, reducing the temperature seems to be the most straight forward way to tackle the problem. But it is not as easy as one might hope. Some of the issues are

- **Cooling down:** The first task is to cool down the setup. Suppose that the goal is to reduce the power of the noise by a factor of 10. The required temperature will be around 30 Kelvin. Liquid Nitrogen (LN) can cool the setup to 77 K, liquid Helium can cool the setup down to 4 K. But a well designed cryostat is required.
- **Material Properties:** Most of material parameters are temperature dependent. For fused silica and tantala deposited by ion beam sputtering process (IBS), their losses are temperature dependent. At temperature between 10 K and 300 K, tantala's mechanical loss can be varied from 3×10^{-4} to 10×10^{-4} [92, 93], and from 1×10^{-4} to 9×10^{-4} for fused silica [93]. These variations due to temperature are not monotonic and usually have peaks around 20–30 K. More importantly, fused silica substrates will have higher loss at lower temperature around 30–40 K [94, 95], making it an unsuitable substrate for a mirror. Other materials that have low loss at cryogenic temperature and have good optical properties are, for instance, sapphire and silicon.

One example of a large scale gravitational wave detector operated at cryogenic temperature will be KAGRA. It will use sapphire test masses during a science run at 20 K. Although sapphire is not a suitable choice for substrates at room temperature because of its high thermoelastic noise, at cryogenic temperature, thermal expansion of sapphire can be very low resulting in the lower level of thermoelastic noise.

2.9.2 Lower Loss

Since Brownian noise is also directly proportional to the material loss, reducing the loss in the coatings can lower the noise, but material with lower mechanical loss is not always the best solution (as in the fused silica/sapphire cause). In addition, the materials must have good optical properties. A few ways to improve the loss without compromising the optical properties are:

- **Doping Ta_2O_5 with TiO_2 :** Loss in tantala is usually higher than that of fused silica. Lower loss in tantala will result in the reduction of the overall loss of the coating. One way to reduce loss in tantala is to mix small amount of TiO_2 into it. This method can reduce tantala's loss by 40 percent [96] without weakening its optical properties.
- **Heat treatment after coating process** Ion-beam sputtered coatings are often heat treated after deposition to reduce the stress in the film and to reduce the optical absorption. This heat treatment also reduces loss in both SiO_2 [97] and Ta_2O_5 [98], as a result of a reduction of internal stresses due to the altered distribution of the potential barrier heights. But the coating can be annealed to around 800 Celsius. At higher temperature Ta_2O_5 starts to crystallize and its optical properties change.

- **Optimized coating structure:** Most of the loss in the dielectric coatings come from Ta_2O_5 . Ring down measurements show that coatings with more Ta_2O_5 have higher loss [99, 100, 101]. If the overall physical thickness of Ta_2O_5 in the coatings can be decreased, the overall loss will be smaller. By adjusting the thickness of SiO_2 and Ta_2O_5 and the total number of layers [102], TNI team has shown that the effective loss in the optimized coating can be reduced by about twenty percent while preserving the reflectivity of the mirror [103].
- **New Material with lower loss:** Recently, thin film of GaAs and AlGaAs and AlGaP has been researched in hope of new low loss coating materials. As crystalline structure has much smaller mechanical loss due to less dislocations and impurities in the material. Its mechanical loss is expected to be one order of magnitude smaller than the conventional fused silica/tantala coatings. More about AlGaAs as coating materials can be found in chapter 5

2.9.3 Different Beam Shape

Using a larger beam size can also reduce thermal noise as the averaged surface is increased, but this method requires larger substrate and coatings to keep the loss from clipping below the acceptable level. By using a different beam shape, the substrate size can be maintained while the effective beam area is larger. Other beam shapes that might be possible to use are mesa beam (flat-top) [104], conical beam [105] or Lagurre–Guass 33 [106]. However, these beam requires special mirror shape and more unstable because of the parametric instability⁴ [109]. Compared to a Gaussian beam shape, they are more sensitive to angular misalignments [110]. Because of these drawbacks, using different beam shape to reduce coating thermal noise might not be a practical solution for the current technology.

2.9.4 No Coating Cavity

Another way to reduce coating thermal noise is to get rid of the coating. This raises the question of how to get a high reflective surface. Two examples are:

- **Total internal reflection Cavity:** Instead of a dielectric mirror, another type of cavity employs a basic principle of total internal reflection to bounce the beam [111]. Although Brownian noise from coatings is completely removed from the system, thermo-optic noise still persists [112]. However, this can be minimize by choosing materials with low thermal expansion coefficient or tuning the temperature such that α is minimized.
- **Grating cavity:** The input mirror of a Fabry–Perot cavity can be replaced by a grating [113]. But a lot of power is lost to other diffraction orders.

⁴Parametric instability occurs when the beat between two optical modes is close to the mechanical frequency of an acoustic mode of the mirror [107, 108].

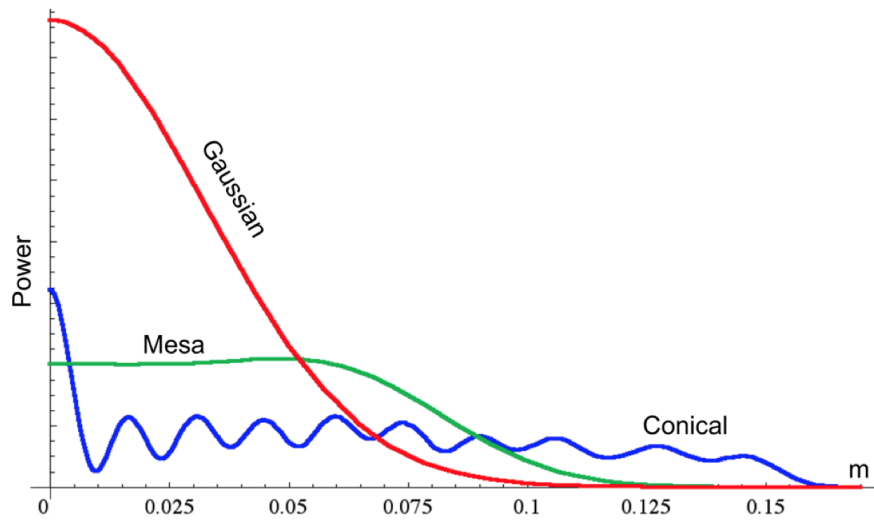


Figure 2.6: Different kinds of Beam profile. Red: Gaussian, Blue: conical, Green: Mesa [105]

A coating free cavity with high mechanical quality factor and a small optical linewidth has not yet been demonstrated. As these techniques are relatively new compared to a conventional cavity formed by dielectric mirrors. More researches have to be done to improve their performances before they can be used as a high finesse reference cavity.

Chapter 3

Experimental Setup



Figure 3.1: A picture taken of the setup for this work. The thermally insulated vacuum chamber that houses the two cavities is at the further end of the optical table.

In this chapter, two experimental setups for observing coating thermal noise are explained in detail. Technical noise sources associated with the setups will be discussed in the next chapter. The first setup measures the noise from 8 inch reference cavities. The second setup which is conceptually similar to the first one, but measures coating thermal noise from 1.45-inch reference cavities.

3.1 Optical Cavity as a Frequency Reference

A Fabry–Perot cavity is formed by two reflecting mirrors facing each other, separated by a distance L . One useful property of the Fabry–Perot cavity is frequency selection. Only light with certain frequencies can pass through the cavity. The cavity’s Free Spectral Range (FSR) frequencies are given by

$$\nu = n \frac{c}{2L}, \quad (3.1)$$

where n is an integer denoting the axial mode number. Basically, it is a condition that the laser must form a standing wave pattern in the cavity. This property allows a Fabry–Perot cavity be a useful tool for laser frequency stabilization. One important property of a laser is its highly coherence output, i.e., a single frequency light, but it has frequency noise which can be measured in the spectral density of noise power, $S_\nu(f)$, in Hz^2/Hz or the linear spectral density, $\delta\nu(f)$, with units of $\text{Hz}/\sqrt{\text{Hz}}$.

The fundamental frequency noise in a laser is placed by the Schawlow-Townes limit [114, 115],

$$S_f^{S-T} = \delta\nu_L \sqrt{\frac{2h\nu}{P_{out}}} \quad (3.2)$$

where $\delta\nu_L$ is the laser cold cavity line width and P_{out} is the laser output power. This is the random frequency noise from spontaneous emission inside a laser. The distribution is flat and can be as low as $0.5\text{Hz}/\sqrt{\text{Hz}}$ for 1mW output because of the narrow laser cavity linewidth [116]. However, the actual noise from a laser is far higher than this. Anything that changes the optical path length of the laser cavity affects the laser frequency. Frequency noise in a Non-Planar Ring Oscillator (NPRO) laser can be roughly estimated to be $10 \text{ kHz} \left[\frac{1\text{Hz}}{f} \right] \frac{\text{Hz}}{\sqrt{\text{Hz}}}$ from 1 Hz to 10 kHz. This estimated frequency noise mostly originates from power fluctuations in its pump laser [117].

If the laser frequency is forced to follow the length of the cavity by means of frequency discrimination techniques e.g. Pound–Drever–Hall locking (PDH) [118, 119] (examples for comprehensive reviews of PDH technique can be found in Ref. [117, 120]). The laser frequency noise can be suppressed significantly until it matches the displacement noise of the reference cavity. The relation between the two is

$$\frac{\delta\nu}{\nu} = -\frac{\delta L}{L}. \quad (3.3)$$

If the dominant displacement noise in a reference cavity is coating Brownian noise, this means that the frequency noise of the laser locked to the cavity contains information about the coating noise in the cavity. By measuring the stabilized frequency noise we can get information about the coating noise. The frequency locking technique can be cast as a linear control theory problem as shown in Fig. 3.2. The laser has free running noise $\delta\nu$. The frequency discriminator D , electronic servo gain G , and actuator response A combine to produce the open-loop gain $H = DGA$. When

the loop is engaged, the suppressed frequency noise $\delta\nu_s$ of the laser becomes

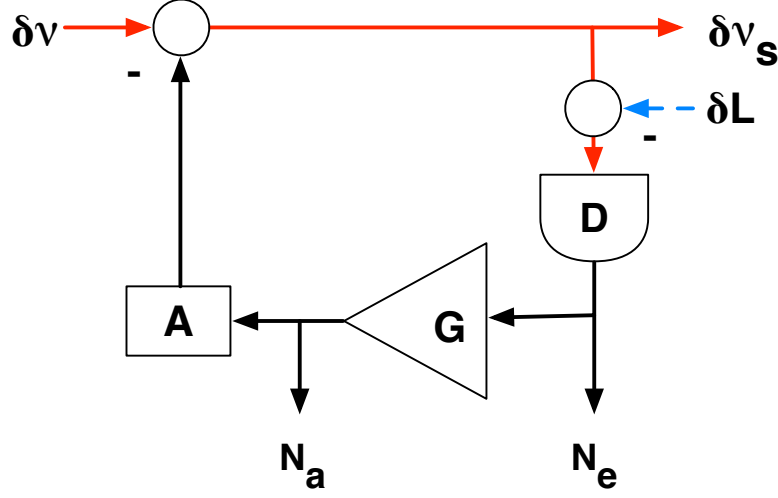


Figure 3.2: A block diagram of PDH lock. $\delta\nu$ is the laser free running noise in $\text{Hz}/\sqrt{\text{Hz}}$, $\delta\nu_s$ is the suppressed frequency noise, or the frequency noise of the transmitted beam behind the cavity, δL is the cavity's displacement noise which converts to the frequency noise via PDH lock. D is the frequency discriminator gain in V/Hz , G is the servo gain in V/V , A is the actuator gain in Hz/V . N_e and N_a are the error signal and the control signal, respectively. The minus sign from the actuator A , represents the negative feedback. The minus sign from δL means the displacement noise of the cavity is compared to the laser frequency.

$$\delta\nu_s = \frac{\delta\nu}{1+H} + \frac{H}{1+H} \times \frac{c}{L\lambda} \delta L \quad (3.4a)$$

$$\approx \frac{\delta\nu}{H} + \frac{c}{L\lambda} \delta L \quad \text{for } |H| \gg 1. \quad (3.4b)$$

Within the loop bandwidth, where the magnitude $|H|$ of the open-loop gain is large, the displacement noise δL of the cavity is impressed onto the frequency noise of the laser: $\delta\nu_s \approx (c/L\lambda)\delta L$. The power spectral density of the frequency noise is given by $S_\nu(f) = |\delta\nu_s|^2$.

It is impossible to measure δL inside the control loop, as N_e is an in-loop sensor, N_a will contain only the information about the free running noise of the laser which is much larger than δL . To measure δL , we have to measure it optically from $\delta\nu_s$ as an out-of-loop witness. The transmitted beam can be compared with a very stable reference, or beat against another identical setup. The latter method is chosen since it offers common mode rejections for disturbance from seismic noise, acoustic noise, ambient temperature noise, and other noises that are coherent between the two setups.

In other words, thermal noise can be measured by having two setups of a laser frequency locked to a reference cavity with the two transmitted beams recombined at the output. Because of the slightly different lengths of the two cavities, the two beams have different frequencies, ν_1 and ν_2 .

When directed onto an RF photodiode, the combined beam results in a beat note with frequency $\hat{\nu} = \nu_1 - \nu_2$ (the high frequency portion $\nu_1 + \nu_2$ is filtered out by a low pass filter). The frequency noise of this beat note has a power spectral density $S_{\hat{\nu}} = S_{\nu_1} + S_{\nu_2}$ which can be read out using a phase-locked loop (PLL) technique¹ which will be discussed in section 4.6.

3.2 Prototype Setup

Instead of using two similar setups of a laser locked to a reference cavity as suggested at the beginning of this chapter, the first setup, serving as a prototype for thermal noise experiment, requires only one laser, one high performance frequency stabilizing servo (FSS), and two reference cavities.

3.2.1 8-inch Reference Cavities

These reference cavities were originally designed as reference cavities for Initial LIGO. We used them largely due to their immediate availability.

- **Mirrors:** The mirror substrates are commercially available fused silica with a 1 inch diameter, 0.25 inch thickness, and a 0.5 m radius of curvature (ROC). The coatings were fabricated by Research Electro-Optics Corporation (REO) of Boulder, Colorado, USA, via ion-beam sputtering in 1998. The coating was annealed at 480 C after deposition. They consist of 28 alternating layers of fused silica (SiO_2) and tantala (Ta_2O_5). The first 27 layers are each deposited to a thickness of $\lambda/4n$, where n is the refractive index of the layer material. Due to its hardness, the final layer is fused silica, and in order to give the correct interference condition, it is deposited to a thickness of $\lambda/2n$. The transmission of each mirror is approximately 300 ppm.
- **Cavities:** Using these mirrors, we initially constructed two symmetric cavities using fused-silica spacers with length $L = 8$ inches. The cavities were formed by optically contacting mirrors to cylindrical fused-silica spacers. Both substrates and spacers are made of fused silica because of its low mechanical loss and small thermal expansion coefficient.
- **Cavity mount:** Each cavity is fitted with a pair of O-rings close to the cavity's Airy points. These O-rings then sit upon a pair of teflon blocks with a semicircular cut. The block has a transverse V-shaped groove to keep the O-ring in place. The cavities are placed side by side on a double-stack seismic isolation platform, as shown in Fig. 3.3. The resonances of this platform all lie below 10 Hz. The use of a single platform and chamber endows the beat measurement with some amount of common-mode rejection of seismic and ambient temperature related noises.

¹For example, see [121].

- **Vacuum chamber:** The cavities and the platform are installed inside a temperature-stabilized vacuum chamber with the pressure below 10^{-7} torr (using an ION pump). Heater jackets are attached around the chamber and a software control loop stabilizes the overall temperature of the vacuum chamber to within 1 mK. The chamber sits on pneumatic legs which have a resonant frequency around 5 Hz.

To tune the beat frequency between the two cavities, each cavity has a separate radiative shield wrapped with a heater wire. The length of the cavity is controlled by thermal expansion via heating of the shield, and the resonant frequency of the transmitted laser is changed accordingly.

Cavity length / FSR	8 inch (20.32 cm) / 738 MHz
Finesse	9,816
Cavity linewidth (FWHM)/ cavity pole	75.2 kHz 37.6 kHz
Beam radius on the mirror	$w_0 = 292\mu\text{m}$
mirror coatings	27 Layers of QWL $\text{SiO}_2/\text{Ta}_2\text{O}_5$ with $\lambda/2$ cap of SiO_2
mirror transmission	300 ± 30 ppm
Loss in each mirror	20 ppm
Mirror radius of curvature	0.5 m

Table 3.1: Table of parameters for 8 inch cavity and the mirrors.

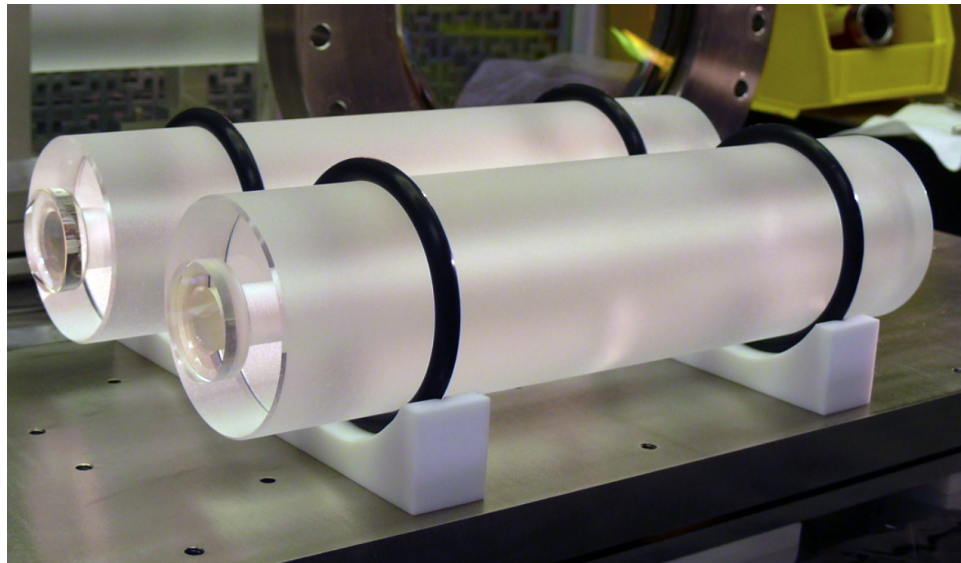


Figure 3.3: 8 inch cavities on the passive seismic isolation stack. The thermal shields are removed to show how the cavities are held.

3.2.2 Setup Layout

Fig. 3.4 shows a schematic of the prototype experimental setup. A 100 mW Nd:YAG laser is simultaneously stabilized to two identical cavities: a reference cavity and an analyzer cavity. Each component in the setup is explained below following the operational step.

- **PMC:** Because the beam profile from the laser does not have a perfect Gaussian profile (TEM00), the beam shape is filtered by a Pre-Mode Cleaner (PMC) triangular cavity [122]. The PMC is locked to the laser frequency via PDH technique, with a sideband frequency of 21.5 MHz. When the beam is close to a purely TEM00 profile, we can reduce the amount of light that cannot be coupled into the Fabry–Perot cavities because of the mismatched beam shape. This left-over reflected light causes extra noises in several ways. It can go back all the way to the laser source and cause instability in the laser frequency. It can increase shot noise level on the RFPD. Additionally, the scattered light associated with the reflected beam can add random phase noise in the PDH locking technique.
- **Locking the laser to reference cavity:** After the beam profile is filtered by the PMC, the side band at 14.75 MHz is added on the carrier by an EOM. The EOM used in the setup is New Focus 4003 with resonant frequency at 14.75 MHz. Then, the beam is separated into two paths. The main path is directed to the reference cavity and the laser is frequency stabilized to the cavity using PDH lock with three actuators acting on the laser. From DC to around 1 Hz, the temperature actuator on the laser head has a large dynamic range. Although the response is slow, the tunable range is up to 40 GHz. The range is calibrated at 4 GHz/V. Around 1 Hz–1 kHz, the PZT attached to the NPRO is used to change the laser frequency, and from 1 kHz to 1 MHz, a broadband EOM dithers the beam’s phase, which is similar to changing its frequency. With all these actuators, the unity gain frequency can reach almost 1 MHz. More details about the frequency stabilization servo (FSS) are discussed in appendix B.
- **Locking the secondary beam to analyzer cavity:** The second beam path is picked off from the main beam behind the PMC and the EOM, so the side bands are already included in the second beam. An acousto-optic modulator (AOM) is used to lock this beam to the second cavity (analyzer cavity). The AOM is driven by a voltage–controlled oscillator (VCO) operated at the nominal frequency of 80 MHz, and the beam is double passed to reduce any position jitters associated with the frequency locking since the deflection angle depends on the driving frequency [123]. First, the AOM shifts the carrier frequency by 160 MHz (double passed, 1st order beam). The cavity length is tuned (by changing the temperature) so that it roughly matches the frequency of the beam. Next is to lock the beam to the cavity. The control loop uses the AOM as a frequency actuator to shift the frequency light going to the analyzer cavity. The feedback to the VCO varies the driving frequency which changes the

frequency of the beam to keep it locked to the cavity. Usually, the operational range of the AOM is around ± 5 MHz. The performance of this loop can be less demanding because the frequency of the main laser is already stabilized to the reference cavity and becomes very quiet. In general, the servo gain has to be enough to suppress any noise introduced by the servo and the VCO. See section 4.4 for more details.

- **beat path** Behind the cavities, the two transmitted beams are recombined (beat) and detected with a photodiode. In order to extract the frequency noise of the beat note due to thermal noise, the beat note is compared to an ultra-stable frequency reference via a phase locked loop (PLL).

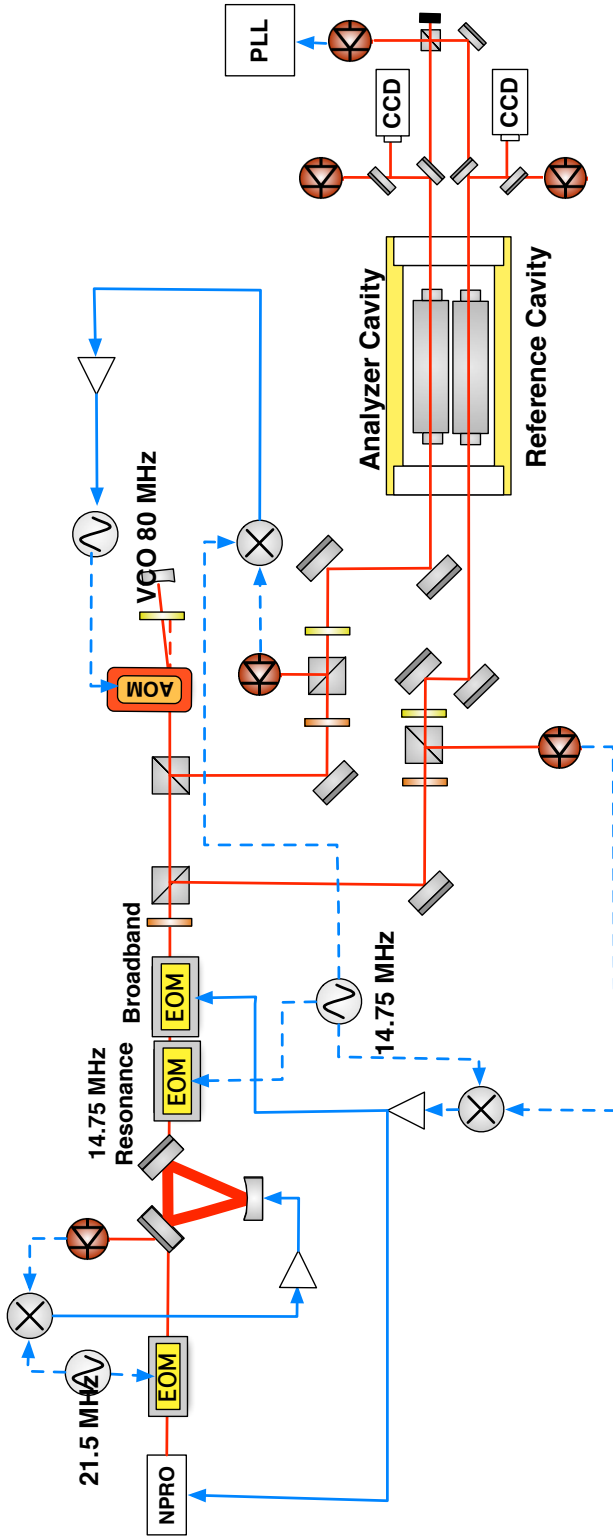


Figure 3.4: The prototype experimental setup for measuring the coating thermal noise of LIGO reference cavities. A Nd:YAG laser is simultaneously stabilized to two identical cavities and the transmitted beams are used to measure the length noise by comparing their beat signal.

3.2.3 Result from the Prototype Setup

The measurement of the noise profile of the prototype setup is plotted together with the noise budget in Fig. 3.5. The sensitivity at low frequencies is limited by seismic noise and scattered light. At frequencies above 1 kHz, the frequency is limited by the local oscillator's phase noise from the PLL readout technique. Since the measured signal is heavily contaminated by technical noise sources, the coating loss extracted from the data is not reliable. This is not surprising, as these reference cavities were not intended for thermal noise measurement. The spot size is fairly large, and the cavities are long. These result in a low frequency noise which is the object of a reference cavity. However this setup has served to provide proof of principal and expertise in the requirement of the frequency stabilization servo and readout technique. More importantly, this prototype demonstrated the achievable sensitivity of the design. Hence the prototype provided confidence that the upgraded setup would be able to observe coating thermal noise.

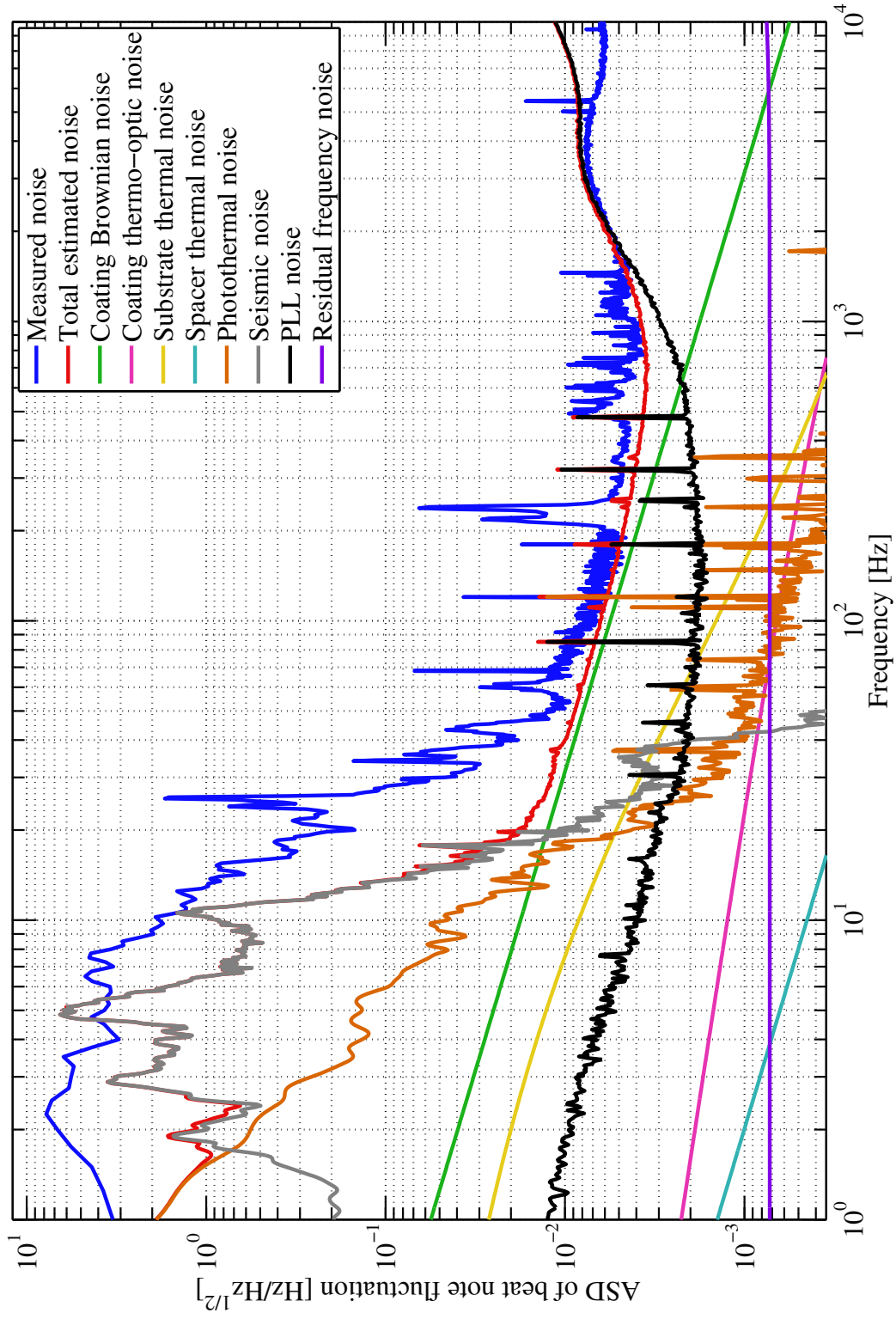


Figure 3.5: Noise budget and the measurement from 8 inch cavities. The estimated coating thermal noise shown in the plot is obtained from Eq. 2.16 with $\phi_c = 4.15 \times 10^{-4}$. Seismic related noise is dominating from DC to 80 Hz. Mechanical related noise around 500 Hz to 1 kHz are from optic mounts and posts in the beat setup.

3.3 Two Laser Setup with 1.45 Inch Cavities

To increase the coating thermal noise, the new setup uses shorter spacers, which are 1.45 inches long, and two lasers, each independently frequency locked to one of the two cavities.

3.3.1 1.45 Inch Reference Cavities

In order to raise the coating noise level, we subsequently constructed two shorter cavities using similar mirrors from the same coating run as those used in the prototype. The shorter cavities will raise the beat frequency noise because of two reasons. First, for mirrors with similar radii of curvature (0.5 m), the shorter cavity results in smaller beam size on the mirror surfaces, and the power spectral density of the displacement noise is inversely proportional to the square of the spot size (cf. Eq. 2.16). For a symmetrical cavity with length L , the spot size on the mirror surface is given by [124]

$$w_0^4 = \left(\frac{\lambda R}{\pi}\right)^2 \frac{L}{2R - L}, \quad (3.5)$$

where R is the radius of curvature of both mirrors. The spot size on the mirror vs. the cavity length is shown in Fig. 3.6. Second, the observed frequency noise increases with inverse of the cavity length (cf. Eq. 3.3).

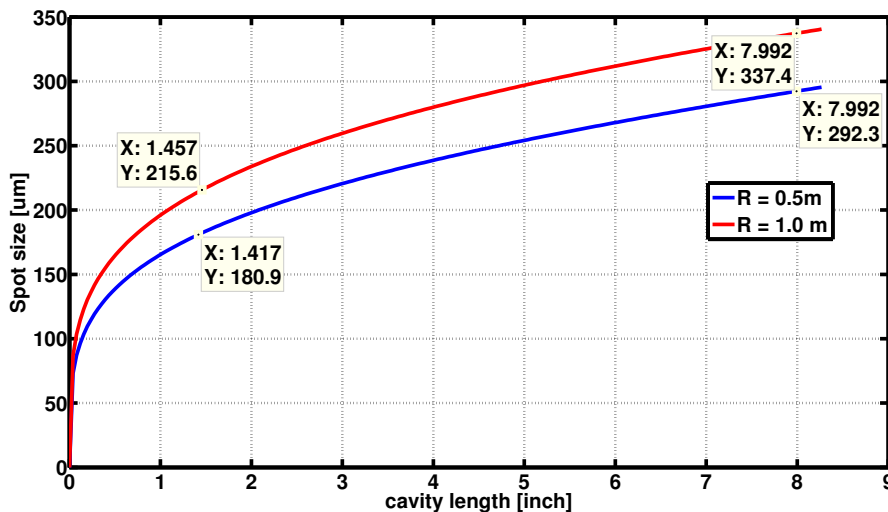


Figure 3.6: The spot size on a symmetrical cavity with length L varied between 0 to 8 inches. The red and blue traces are the spot sizes on mirrors with 1 and 0.5 inch radii of curvature, respectively.

Although the shorter cavity increases the observed frequency noise as discussed above, there are several considerations that place a lower limit for the allowable length of the new cavities. First, it must be possible to use a heater to tune each cavity length by half of a free spectral range, so that the beat note frequency can be brought within the bandwidth of the readout photodiode. A cavity

that is too short would require excessive heating in order to achieve this. Second, the cavity must form a stable optical resonator. Finally, the length must be chosen so that no higher-order transverse laser modes resonate simultaneously with the TEM00 mode. The full detailed explanations for the decision to use 1.45 inch cavities are given in appendix E, and the summary of the cavity properties is shown in Tab. 3.2.

For a 1.45 inch cavity, the frequency noise of the beat note due to the coating Brownian noise will be increased by a factor of ~ 8.7 from that of the prototype. Thus, with the shorter cavity length, and the already achieved sensitivity in the previous setup, the Brownian thermal noise of the quarter wave silica/tantala from the 1.45 inch cavities should be high enough to be observed between 65 Hz and almost 1 kHz.

In order to improve the sensitivity at low frequency which is dominated by seismic noise, the cavities are held at the optimum support positions to minimize the displacement noise due to vibration. See appendix E for more details about the search for the optimum support positions.

Cavity length / FSR	1.45 inch (3.68 cm) / 4.07 GHz
Finesse	9,816
Cavity linewidth (FWHM)/ cavity pole	414.9 kHz / 207.5 kHz
Beam radius on the mirror	$w_0 = 182\mu\text{m}$

Table 3.2: Table of parameters for 1.45 inch cavity.

3.3.2 Overall Explanation of The Two-Laser Setup

Fig. 3.8 is a schematic of the final setup. It is symmetric; the PDH error signal from each cavity is used to actuate on the PZT of an independent NPRO and on a broadband EOM. For each path, 1 mW of light is incident on each cavity. The visibilities of both cavities exceed 0.9, indicating that the incident beams have a nearly Gaussian spatial mode and that the cavities are close to critically coupled. The use of two lasers also allows larger possible range for the beat frequency; in the previous setup, this was constrained by the operational range of the AOM. Typically, an AOM also distorts the beam and thereby reduces the coupling into the cavity and makes the cavity stabilization scheme more sensitive to other noise sources. It also limits the loop bandwidth when it is used as an only actuator for frequency stabilization.

In this setup, the relative intensity noise (RIN) in both cavities becomes uncorrelated, and so an intensity stabilization servo (ISS) is required. In each path, an electro-optic amplitude modulator (EOAM²) is used to suppress the laser’s RIN, and thereby decrease the photothermal noise to be less than the estimated thermal noise of the coatings. Similar to the prototype setup, each cavity is installed with a thermal shield and a heater wire to control the differential length between the two

²Newport 4104, http://assets.newport.com/webDocuments-EN/images/410412F_410X%20Manual_RevF.pdf

cavities via thermal expansion, see Fig. 3.7.

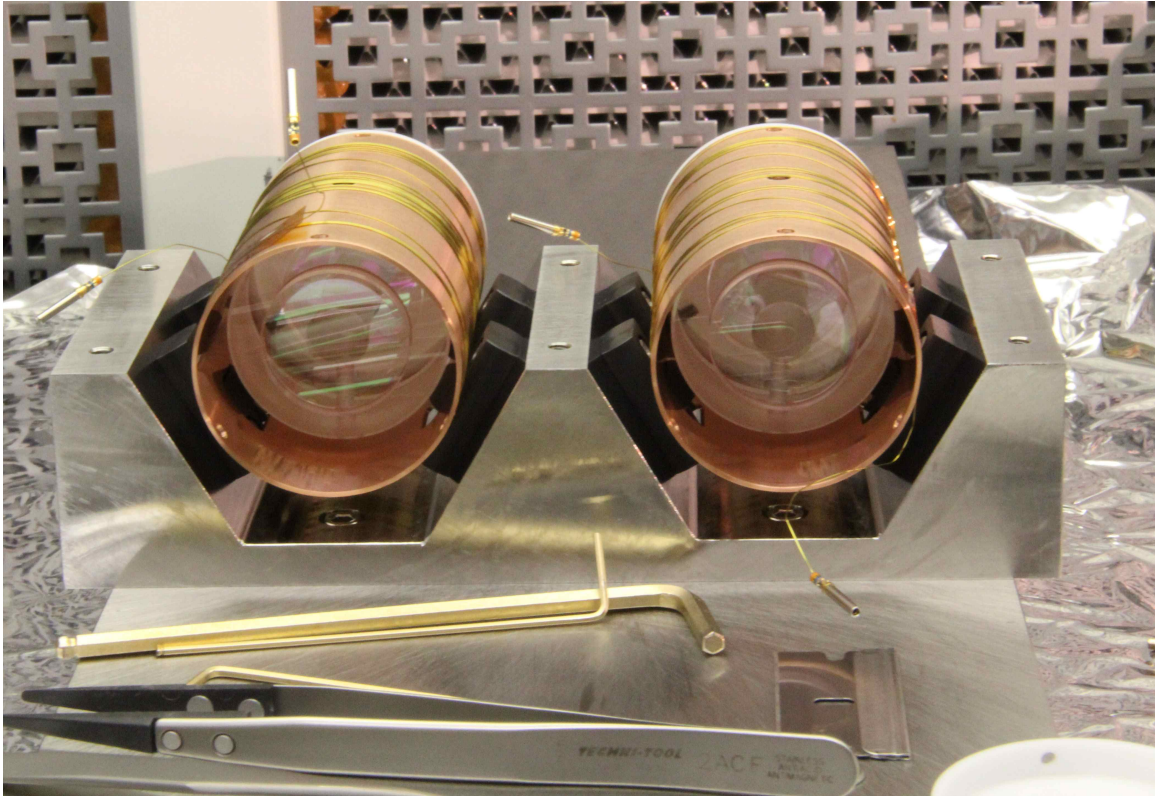


Figure 3.7: Reference cavities with thermal shields and the mount on double seismic isolation stacks. Heater wires are wrapped around the shields. The shields have opening on their sides so that the cavities can sit on the supports.

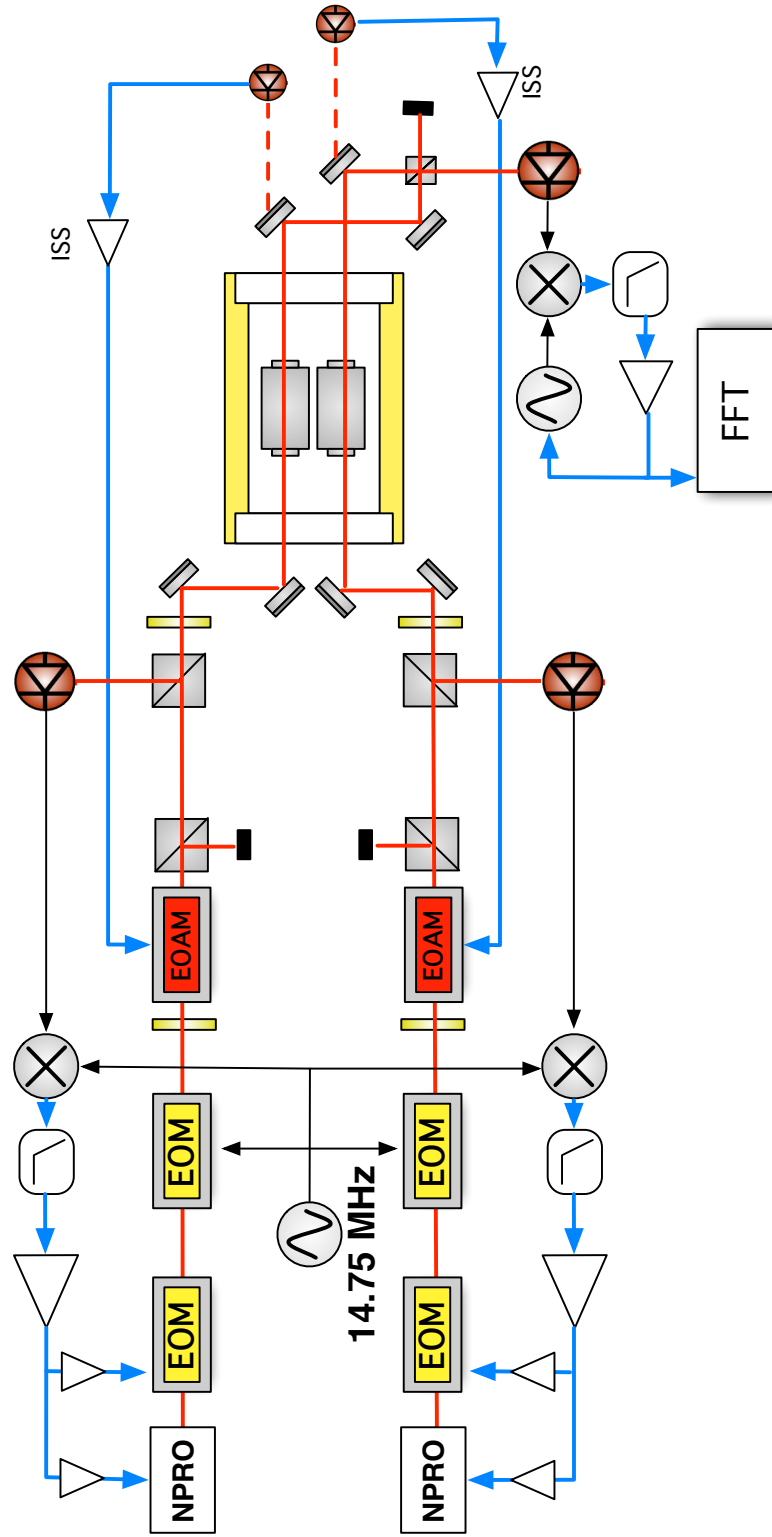


Figure 3.8: Setup for measuring the coating thermal noise using two independent lasers. Each laser is stabilized to one of the two identical cavities. The readout-scheme would be the same: the transmitted beams are used to measure the length noise by comparing their beat signal. One of the NPRs has a Pre-Mode Cleaner cavity which is not shown in the diagram

3.3.3 Result from 1.45 Inch Cavities

Is it Coating Thermal Noise?

The result of this two-laser measurement is shown in Fig. 3.9. The technical and environmental sources which limited the one-laser measurement are now subdominant in the band from 10 Hz to 1 kHz. The measurement is compared to Eq. 2.16, and the fitted coating loss angles ϕ_c is $(4.2 \pm 0.3) \times 10^{-4}$ (the error analysis is given in appendix G.3). When this effective loss is applied to the 8 inch cavity measurement, the estimated result is also comparable to the measurement shown in Fig. 3.5. There are three pieces of evidence that suggest that the observed noise is really the coating thermal noise sensed by a Gaussian beam.

- The slope of the linear spectral density of the frequency/displacement noise is inversely proportional to square root of frequency, cf. Eq. 2.16.
- The extracted loss angle is comparable to the previous direct measurement. Numata et al. [54] also reported the loss angles of QWL SiO_2/Ta_2O_5 on fused silica substrate to be 4×10^{-4} .
- The signal scales correctly with the spot size. As seen in the results between 8–inch and 1.45–inch cavities. Had the signal come from other sources (e.g., substrate, spacer Brownian noise, noise in the bonding between the substrates and the spacer), the scaling would have been different. Substrate thermal noise is inversely proportional to spot size. Spacer thermal noise should be independent from spot size.

This effective loss angle ϕ_c obtained from the data here through Eq. 2.16 should be viewed as a figure of merit and not a real physical loss of the coating, since the equation assumes that elastic properties of the coatings are similar to those of the substrate. The purpose of the fitting data using Eq. 2.16 is to compare the result here with Ref. [54] that uses the same Coating Brownian noise formula.

3.4 Discussion

According to the calculation by Hong et al. [53], coating Brownian noise can be written as a linear combination of ϕ_L and ϕ_H ³ Eq. 2.20 can be rewritten as

$$S_x^{coatBR} = q_L \phi_L + q_H \phi_H, \quad (3.6)$$

³Here we use two assumptions. First, losses of bulk and shear modes are similar in each material. Second, light is promptly reflected at the coating-air surface.

where subscripts L and H denote fused silica and tantala, respectively. Combining the above measurement and the material parameters in Tab. C.1, Eq. 3.6 becomes,

$$\phi_H = -1.41 \phi_L + (9.7 \pm 0.7) \times 10^{-4} \quad (3.7)$$

To extract each loss angle, the equation is compared with a ring down measurement from Ref. [51] with a correction noted in Ref. [99]. The ring down measurement is made on a disc sample. The coating is QWL structure of SiO_2/Ta_2O_5 with the total thickness of 4.66 microns. Both the ring down samples and our mirrors were fabricated around 2000 by the same vendor (REO), so the material formula, depositing process, and treatment techniques should be very similar. Because the coating is much thinner than the substrate, the ring down measurement is associated mostly with the parallel direction of the coating surface [51]. The reported loss angle from such coating is

$$\phi_{\parallel} = (5.2 \pm 0.3) \times 10^{-4}, \quad (3.8)$$

Together with Eq. 2.19, the result can be written as

$$(5.2 \pm 0.3) \times 10^{-4} = 0.58 \phi_H + 0.42 \phi_L. \quad (3.9)$$

Finally, Eq. 3.7 and Eq. 3.9 yield⁴,

$$\phi_L = (1.1 \pm 0.3) \times 10^{-4}, \quad (3.10a)$$

$$\phi_H = (8.2 \pm 0.3) \times 10^{-4}. \quad (3.10b)$$

These numbers are about a factor of 2 higher than the values reported in the literature. The losses of fused silica and tantala in thin-film form (ion beam sputtered, annealed at temperature around 500 C) obtained from ring down measurements [99, 100, 101, 125] are $\phi_L = (0.7 \pm 0.3) \times 10^{-4}$, and $\phi_H = (4.4 \pm 0.4) \times 10^{-4}$. However, our samples were coated by DC sputtering, which might add carbon, iron to the coatings. The samples reported from the ring down measurements with lower losses were fabricated after 2003. It is highly possible that these coating samples were fabricated by better equipment (RF sputtering technique) that introduced less contaminants to the coatings [126].

⁴For more details on extracting ϕ_L and ϕ_H by Bayesian analysis, see appendix G.4.

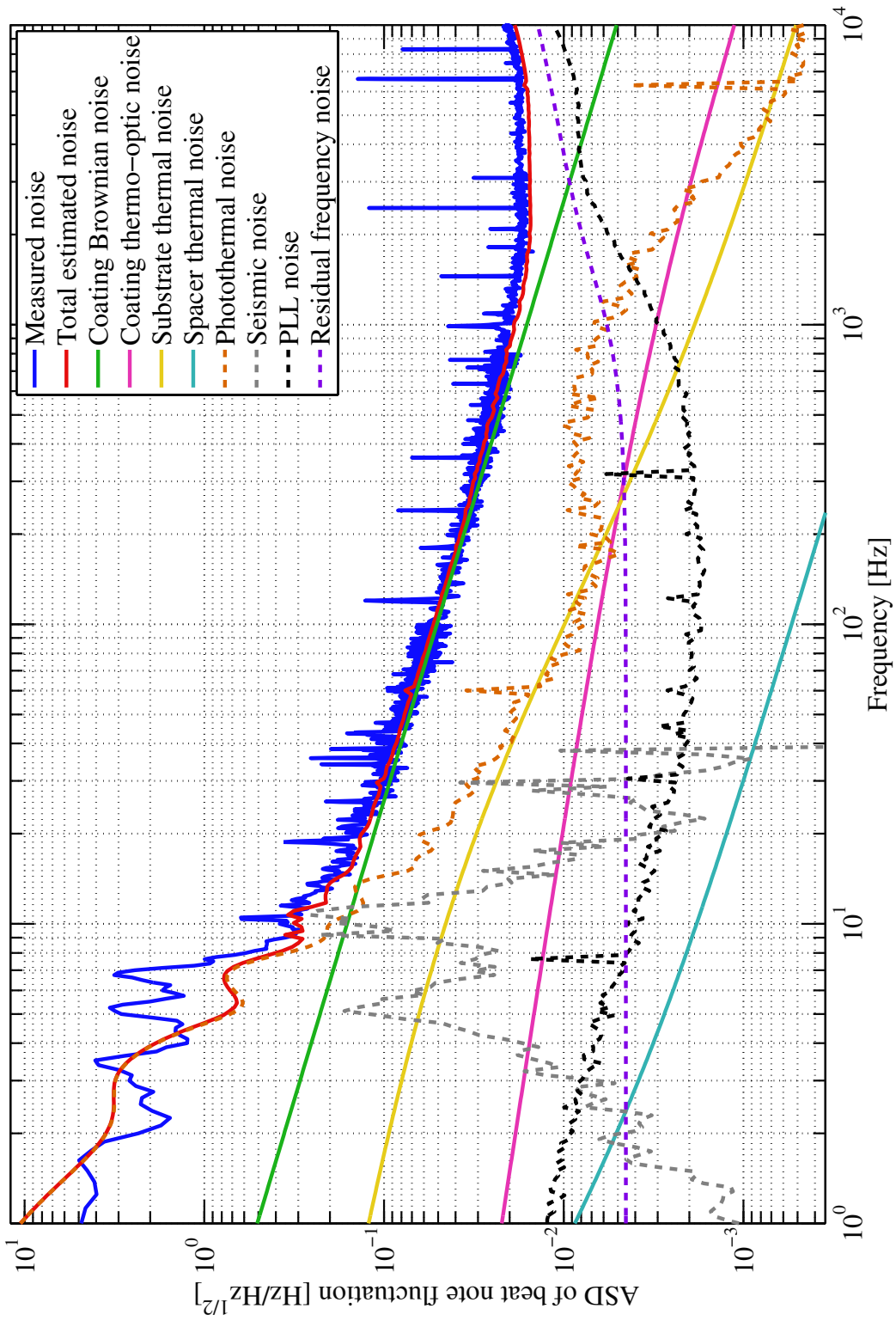


Figure 3.9: result from short cavity :

Chapter 4

Technical Noise in the Setups

Both setups discussed in the previous chapter have similar tools (reference cavity, seismic isolation, vacuum chamber, electronic equipments). They also use PDH method to lock laser frequency to the cavity, and PLL to measure the frequency noise of the beat note. As a result, the technical noise sources associated with these setups are also the same. They can be roughly categorized into three kinds. Some significant ones are the following:

- **Mechanical-Related:** Cavity sagging due to seismic noise, vibrations from mirror mounts.
- **Electronic-Related:** Sensing noise from PDH lock, readout noise from PLL.
- **Optical-Related:** Photothermal noise, ambient temperature changing the cavities' length via thermal expansion.

4.1 Seismic Noise

4.1.1 Coupling from Seismic to Displacement Noise

Cavity bending due to vibration has been known as a significant displacement noise for a reference cavity. Attempting to minimize the effect, some groups reported holding methods by cutting or drilling into a spacer to hold it at the optimum point where the coupling from seismic noise is significantly reduced, or even holding the cavity vertically [127, 128, 129]. We decided to leave the spacer intact and to support it on the outer surface to avoid any extra loss due to a machining process on the spacer. Because of the space limitation, we also hold the cavities horizontally.

The total displacement noise due to seismic is given by

$$S_x(f) = \dot{v}_{\text{table}}(f) TF_{\text{mount}}(f) h_{\text{cavity}} L, \quad (4.1)$$

where $\dot{v}_{\text{table}}(f)$ is the power spectrum of the vertical seismic noise (acceleration) measured on the table [$\frac{m/s^2}{\sqrt{Hz}}$], TF_{mount} is the transfer function of the seismic isolation mount from the table to the

cavity, h_{cavity} is the coupling from the seismic noise to the cavity strain noise computed by FEA (COMSOL), and L is the cavity length.

For the 8 inch cavity held at their Airy position as shown in Fig. 3.3, $h_{\text{cavity}} = 2 \times 10^{-10} [\frac{s^2}{m}]$. For the 1.45 inch cavity, as we changed the supporting method, we also searched for the optimum support points to minimize the coupling. Consequently, the strain due to seismic noise is brought down to $6 \times 10^{-12} [\frac{s^2}{m}]$. Details about how to calculate h_{cavity} and how to search for the optimum support points for the 1.45 inch cavity can be found in appendix E.4.

This h_{cavity} is the coupling from a single cavity. The actual effect could be different because the frequency noise in the beat note is affected by the differential displacement between the two cavities. It also depends on how well both cavities and the support points are positioned, as misplaced support points lead to different coupling.

To estimate the differential coupling, we added random error on the support positions, limited to ± 0.5 mm, then recalculated the coupling on a cavity. The results from simulations are shown in the histogram below.

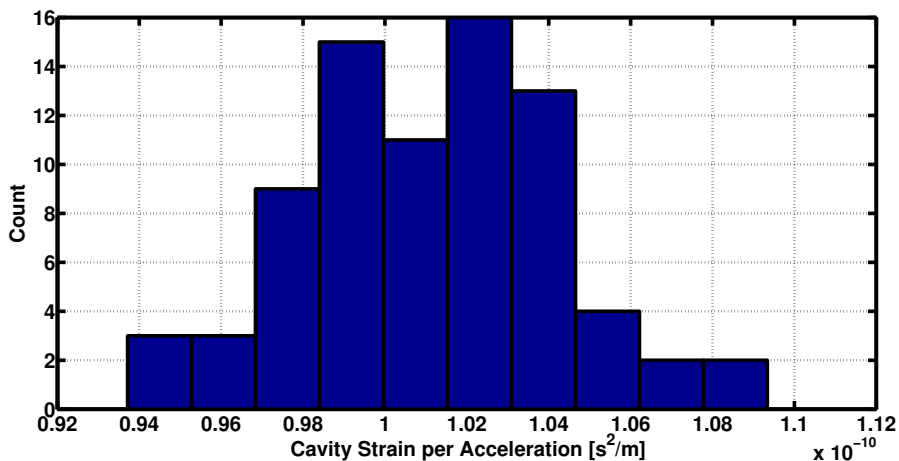


Figure 4.1: Histogram of the vertical seismic to strain coupling with random variations in the support positions on 1.45 inch cavity.

Next, we must take common mode rejection into account. According to the simulation result, most of the time, the strain will fall between 0.98×10^{-10} and $1.04 \times 10^{-10} [s^2/m]$. We can assume an upper bound that one cavity has the strain of 1.04×10^{-10} and another has 0.98×10^{-10} . Thus, the effective coupling for the differential strain is $(1.04 - 0.98) \times 10^{-10} = 6.0 \times 10^{-12} [\frac{s^2}{m}]$. Due to the common mode rejection, our the strain coupling is comparable to other techniques used for minimizing seismic coupling noise, see section A for comparisons with other low noise cavity experiments.

4.1.2 Scattered Light and Seismic Isolation in the Setup

Seismic noise not only shakes the cavity length, but also perturbs the phase of the reflected light consisting of the carrier and the scattered light. This reflected light adds on random phase noise to the error signal of the PDH lock. The FSS will interpret this phase noise as the cavity’s displacement noise causing an extra frequency noise in the beat note. Scattered light occurs at every optic’s surface. The most important ones lie between the RF photodiode for PDH lock and the cavities because of their proximity to the RF photodiode, which is the main sensing equipment. It is complicated to quantify or to directly measured the coupling of this effect in the setup [130]. Hence, it is best to try to minimize the motion of the cavities and the vacuum chamber. A few passive seismic isolation systems are used to reduce the seismic noise in the setup. They will not only decrease the scattered light caused by vibration, but also reduce the transfer function $TF_{\text{mount}}(f)$ in Eq. 4.1. The seismic isolation stages are

- Newport S-2000 Pneumatic Vibration Isolator with Automatic Re-leveling. The table is floated with a set of 4 pneumatic legs. The resonant frequency is around 1 Hz on both vertical and horizontal directions. The legs are supplied with a bottle of compressed air during the measurement.
- Air springs. A set of pneumatic air springs are used to support the vacuum tanks on the optical table. The attenuation is at least a factor of 10 at 20 Hz and above, see Fig. 4.2.
- Double-stage seismic isolation stack. Each stage rests on a set of RTV silicone. This material is vacuum compatible [131]. It acts as a spring for the passive isolation stage.

Aside from the seismic isolation, the scattered light can be minimized by dumping all the stray beams appropriately. These stray beams are the reflected beams from optic components (e.g., photodiodes, beam splitters, vacuum chamber’s window).

4.2 Mechanical Peaks from Opto–Mechanical Components

Motions on the optic mounts perturb the phase of light as it propagates. This mechanically induced phase noise is also added up to the laser frequency noise. These mechanical peaks are not a serious problem if they occur between the laser and the polarizing beam splitter (PBS) for the reflected beam used in PDH lock, since they will be similar to the laser frequency noise and can be suppressed with the FSS. However, if they occur between the reference cavity and the RF photodiode, the effect will be indistinguishable from the real cavity’s displacement noise. The same problem also happens behind the cavities where the beams recombine. We identified the mechanical peaks associated with each optic mounts in the beam path by exciting each one and observing the resulting peak in the

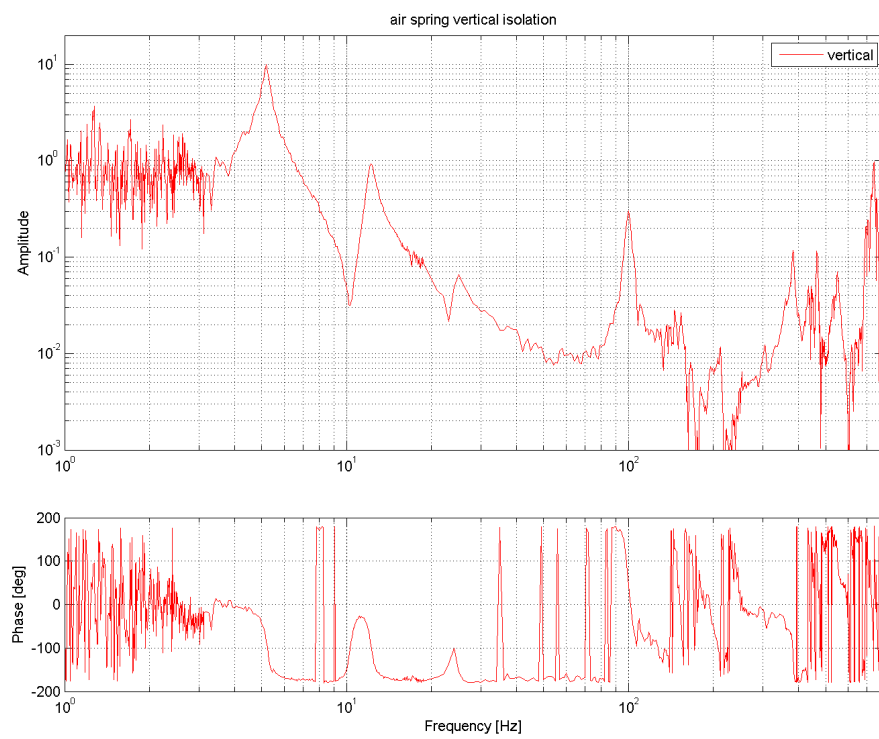
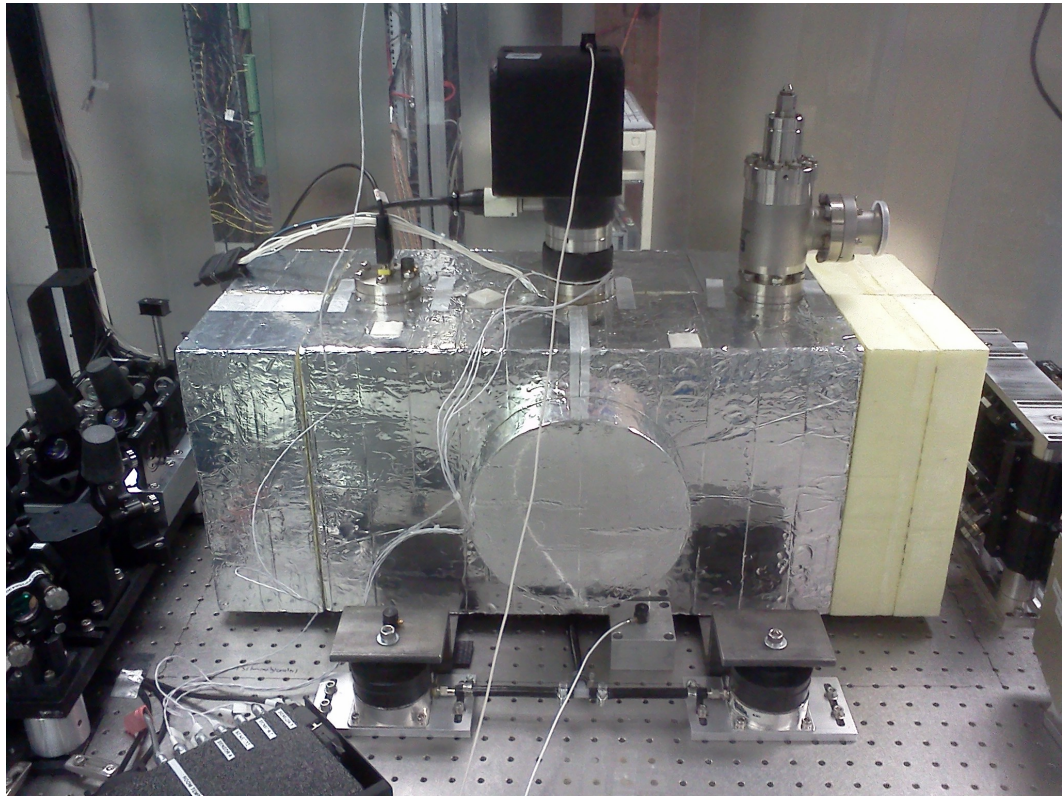


Figure 4.2: Top, the air springs supporting the vacuum chamber. Bottom, the transfer function between the table and the chamber.

power spectrum of the beat readout, see Fig. 4.3. Due to the structure of the components, the most vibration sensitive ones are the periscopes used for directing the beams to the cavities, the beam splitter for recombining the beams, and the quarter wave plates. These resonant peaks vary from 500 Hz to 1.2 kHz. We minimize those peaks by damping them with blocks of rubber. We removed the output periscopes behind the cavities by installing the beat readout path on a raised platform. The mirrors are mounted on pyramid-like bases which are screwed on the table, not clamped. The end beam splitter is mounted in a solid block with no adjustment knobs. These solid bases can reduce the associated mechanical peaks significantly.

4.3 PDH Lock: Shot Noise

When a reference cavity is used for frequency locking via PDH technique, the reflected light from the cavity beats with the sidebands to create the error signal. The slope of the error signal from PDH locking technique can be written as [120]

$$\frac{dP}{dL} = -16P_{in}J_0(\beta)J_1(\beta) \times \frac{Finesse}{\lambda}, \quad (4.2)$$

where P_{in} is the input power, $J_0(\beta)$ and $J_1(\beta)$ are Bessel's functions of the first kind, β is the modulation depth ($= 0.2$ rad for the setup). In other words, the power of the error signal is proportional to the mismatch between the laser frequency and the cavity's length. In general, this method is insensitive to power fluctuations. When P_{in} changes due to some classical fluctuations, the slope changes, but the servo still knows which direction it has to act follow the cavity. However, the incident light that carries information about the cavity length exhibits another fundamental noise, which is shot noise. It arises because of the vacuum fluctuations which occur even though the laser power, P_{in} , is constant. The servo will not be able to distinguish it from the real power change due to the cavity length change and try to compensate for it and create extra frequency noise. The power fluctuation due to the total power on the photodiode is

$$dP_{\text{refl}} = \sqrt{2h\nu P_{in} ((1 - \eta)J_0^2(\beta) + 1.5 \times 2J_1^2(\beta))}, \quad (4.3)$$

where P_{RFPD} is the power falling on the photodiode for PDH lock, η is the visibility (ranging between 0 and 1). The reflected power contains power from a part of the reflected carrier due to mode mismatch and the two side bands. The factor of 1.5 in the sideband term originates from the non-stationary nature of the shot noise produced by the sidebands [132] and the fact that we are using a sine wave demodulation [133]. Combining Eq. 4.2 and Eq. 4.3 together, we get the equivalent

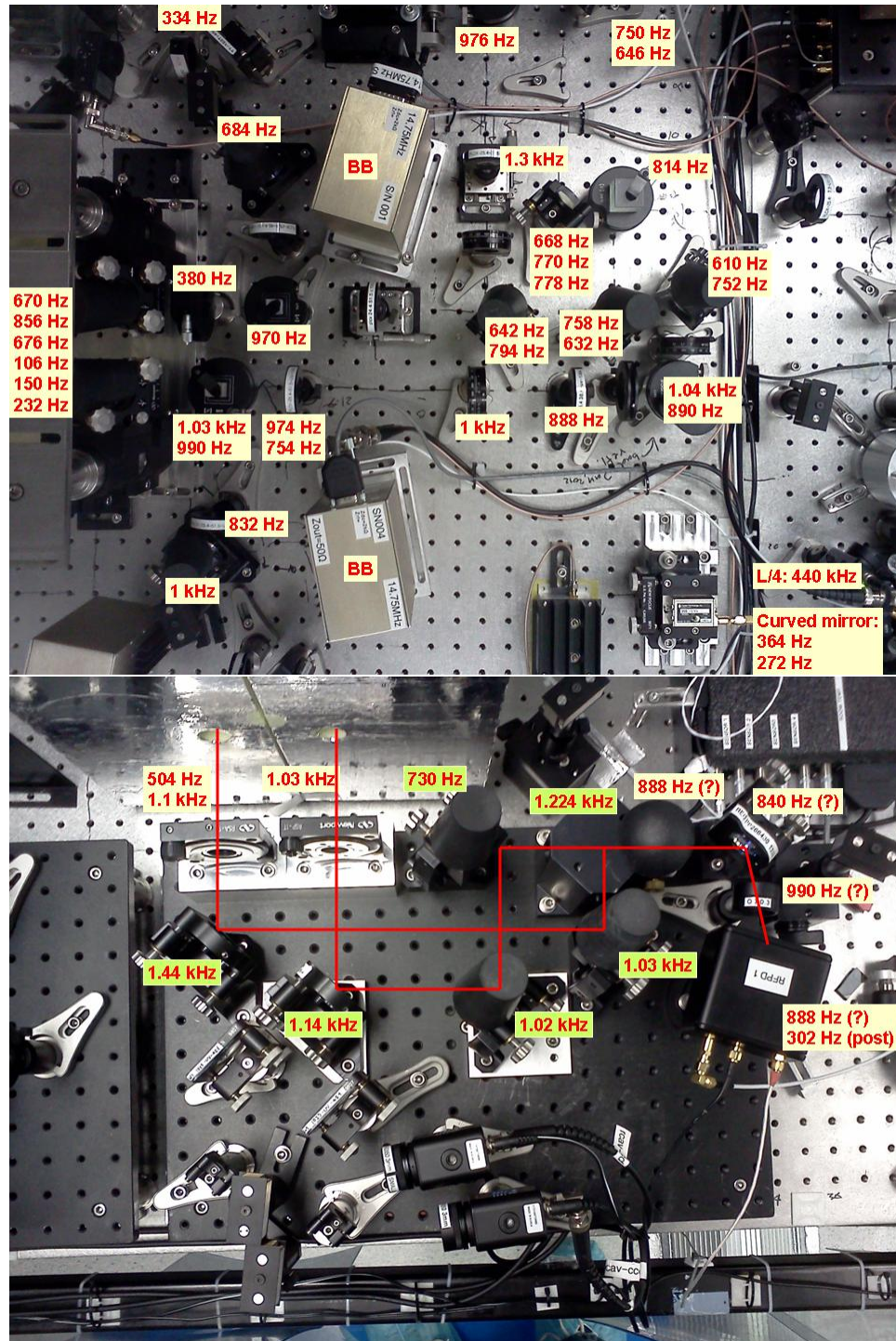


Figure 4.3: Mechanical resonant peaks due to opto-mechanical components. Top, the setup of the input optics. Bottom, the setup behind the cavity where the transmitted beams recombine.

length noise due to the shot noise as

$$dL(f) = \frac{dP_{\text{refl}}}{dP/dL}. \quad (4.4)$$

This is important in the noise optimization aspect. Theoretically, the maximum sensitivity of the PDH lock is achieved when the modulation index is equal to 1.08 [120]. However, the more power allocated to the sideband (term with $J_1(\beta)$), the higher the shot noise. By tuning the modulation index β , we can minimize shot noise. Care should be taken, since it also affects the electronic noise in the PDH lock, as we will see in the next section.

4.4 PDH Lock: Electronic Noise

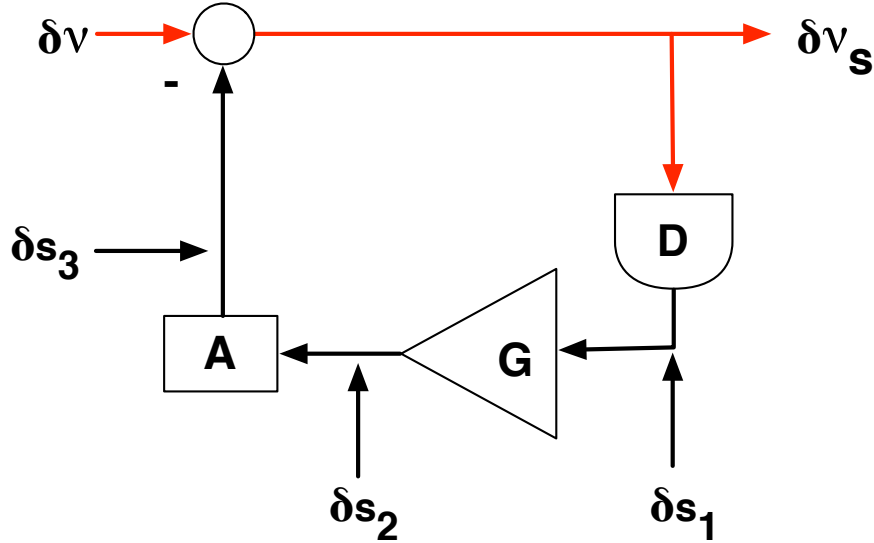


Figure 4.4: Noise in PDH lock technique.

Electronic equipment used in PDH lock contributes electronic noise along the process. Fig. 4.4 demonstrates possible noise sources in each component of the control loop. The suppressed frequency (ignoring the cavity displacement noise) can be calculated as follow

$$\delta\nu_s = \delta\nu - \delta\nu_s DGA \pm \delta s_1 GA \pm \delta s_2 A \pm \delta s_3 \quad (4.5a)$$

$$= \frac{\delta\nu}{1 + DGA} \pm \frac{\delta s_1 GA}{1 + DGA} \pm \frac{\delta s_2 A}{1 + DGA} \pm \frac{\delta s_3}{1 + DGA} \quad (4.5b)$$

$$\approx \frac{\delta\nu}{1 + DGA} \pm \frac{\delta s_1}{D}, \quad \text{when } G \gg 1, \quad (4.5c)$$

where \pm signs denote the incoherent sum from the noises due to their random nature. In the limit of very large servo gain, the noise associated with the frequency discriminator (from RFPD

to the mixer out of the demodulated signal) dominates all other terms and the effective noise is $\delta s_1/D$. δs_1 can be measured from the mixer output when the loop is disengaged and the beam to the RFPD is blocked. The frequency discriminator gain D , can be calculated according to Eq. 4.2, if the modulation index, quantum efficiency of the photodiode, and the impedance of the RFPD are known, or it can be measured directly from the setup by scanning the laser frequency and observing the error signal at the mixer output on an oscilloscope. The slope will be in units of [*Volt/second*] as we record the time domain of the signal. If the scanning is large enough to include the error signal due to the sideband, the time during the scan between the carrier and the sideband frequency will give the conversion from [*second*] to [*Hz*], these will provide the gain of the frequency discriminator in the units of [*Volt/Hz*]. The electronic noise associated with the RFPD and the mixer can be directly measured at the mixer output while blocking the beam.

To reduce the frequency discriminator noise, we can increase the gain D , by increasing the input power, the cavity finesse, the modulation index, or the transimpedance of the RFPD. In practice, the finesse and the transimpedance of the RFPD might not be easily adjusted. So increasing the input power or the modulation depth will be done most of the time during the optimization. But care should be taken since these parameters also affect other noise sources as well (e.g., shot noise limit, and photothermal noise).

In the prototype setup (a single laser with 8-in cavities), where the main beam is already locked to the reference cavity, the frequency noise of the laser becomes $\delta\nu_s$ and the servo will lock the beam to match the analyzer cavity with displacement noise δL_2 , which results in the frequency noise $\delta\nu_{s2}$. If we follow the diagram shown in Fig. 4.4, the noise calculation for the second loop can be written as

$$\delta\nu_{s2} = \delta\nu_s - \delta\nu_{s2}DGA + \delta L_2DGA \pm \delta s_1GA \pm \delta s_2A \pm \delta s_3 \quad (4.6a)$$

$$= \frac{\delta\nu_s}{1 + DGA} + \frac{\delta L_2DGA}{1 + DGA} \pm \frac{\delta s_1GA}{1 + DGA} \pm \frac{\delta s_2A}{1 + DGA} \pm \frac{\delta s_3}{1 + DGA} \quad (4.6b)$$

$$\approx \frac{\delta\nu_s}{DGA} + \delta L_2 \pm \frac{\delta s_1}{D} \pm \frac{\delta s_2}{DG} \pm \frac{\delta s_3}{DGA}. \quad (4.6c)$$

In general, the free running noise of the laser $\delta\nu$ is the highest compared to the others, but for this case, $\delta\nu$ is suppressed and becomes $\delta\nu_s \approx \delta L_2$. Therefore the servo gain G for this loop is not as demanding as that of the first loop. The main concern for the second servo is to suppress all the noise associated with the electronics and the VCO ($\delta s_2, \delta s_3$) below the coating noise level.

4.5 PDH Lock: Residual Amplitude Modulation

Residual amplitude modulation (RAM) usually includes many effects that create amplitude modulation at the frequency of the sideband. RAM causes an offset in the PDH error signal and the

lock becomes susceptible to the other effects (e.g., power fluctuation)¹ One of the most important components that introduce RAM is the EOM used for adding sidebands. The EOM varies the phase and frequency of the beam by changing the refractive index due to the applied voltage. If the alignment of the EOM axis and the polarization of the incident light do not match, the polarization of the beam is changed at the same frequency as the sideband, and as the beam propagates through the setup and encounters polarizing beam splitters (PBS), the varying polarization is converted to the amplitude noise. Meanwhile, the axis of the EOM can also be changed due to the stress-induced birefringence (which occurs due to the temperature change). Thus, to minimize the RAM, the EOM was temperature-stabilized with insulation and a heater, and then the polarization of the beam was adjusted by a half wave plate in front of the EOM so that input polarization matches the electric field axis inside the EOM crystal. To optimize the polarization, the laser frequency is set to be off resonant from the cavity. The power is reflected off of the cavity on to the RFPD, then the amplitude output is monitored. By slightly changing the polarization input to the EOM, the peak in the output at the sideband frequency can be minimized.

4.6 Noise from Phase Locked Loop Readout

A phase locked loop (PLL) is used to measure the frequency noise in the beat signal. In principle, a stable reference signal is controlled so that its phase matches the phase of the target signal, which is the beat note in this case. By observing how much the control signal has to follow the beat note, the noise of the beat note can be measured. A schematic diagram of a PLL setup is shown in Fig. 4.5

From the diagram, we can calculate how the noises from RFPD and VCO show up in the final readout.

$$\delta\nu_s = \delta\nu \pm \delta n \pm \delta V - \delta\nu_s DAG \quad (4.7a)$$

$$= \frac{\delta\nu \pm \delta n \pm \delta V}{1 + DAG} \quad (4.7b)$$

$$V_{fb} = \delta\nu_s DG \quad (4.7c)$$

$$= (\delta\nu \pm \delta n \pm \delta V) \frac{DG}{1 + DAG} \quad (4.7d)$$

$$\approx (\delta\nu \pm \delta n \pm \delta V) \frac{1}{A}, \text{ for } G \gg 1 \quad (4.7e)$$

With sufficient gain G , by monitoring V_{fb} , we can convert it to the beat frequency noise $\delta\nu$ by the actuator gain A . (see Fig. 4.7 for an example of the measurement of the calibration factor A).

However, the noise δV from the VCO, and the noise from the RFPD (δn can represent both shot noise and electronic noise since they combine after the RFPD) show up directly in the beat readout

¹see, e.g., the discussion by Ishibashi et al. [134].

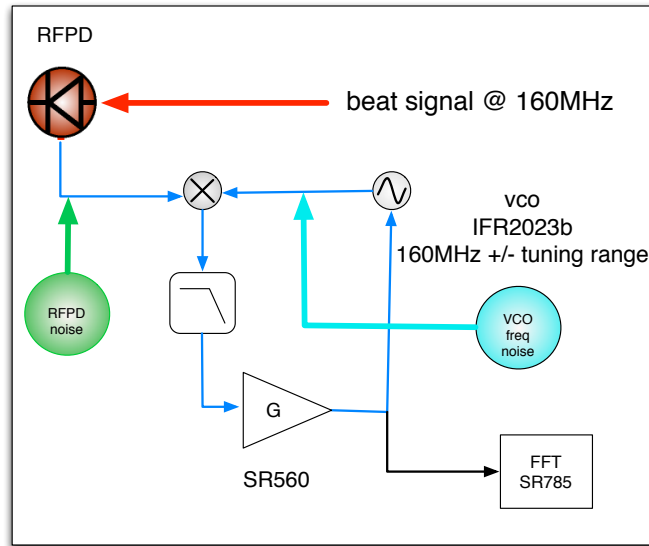


Figure 4.5: A setup of phase locked loop readout. The RF photodiode used in this work is Newport 1811. The beat note is demodulated by a low noise voltage controlled oscillator (VCO) and the error signal is fed back to the VCO. This error signal is amplified by the gain servo (G) and becomes a control signal. It tells the VCO output to match the input beat note. With sufficient gain, this control signal represents the noise in the beat note. For our experiment, the operating setup includes, a level 13 mixer, a low pass filter is at 10 MHz, the servo gain is SR560 with the setup at dc with gain 200. The VCO is IFR2023b with 1 kHz tuning range.

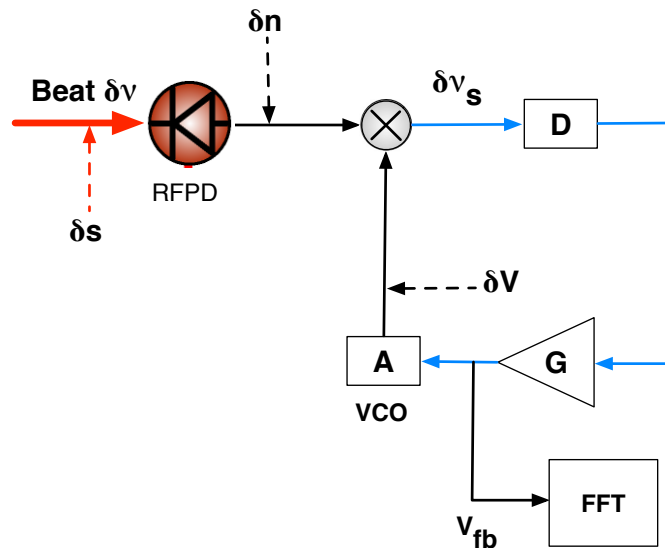


Figure 4.6: A block diagram of PLL. $\delta\nu$ is the frequency noise of the beat note to be measured, δs is the shot noise of the incident beam, δn is the electronic noise from the beat photodiode, and δV is the frequency noise of the oscillator.

(again, the \pm sign denotes the incoherent sum from each noise). We have to characterize them to make sure that their levels are below the expected beat noise.

Frequency Noise from the VCO

The measured frequency noise from the VCO from different settings is shown in Fig. 4.8. The setup is similar to PLL, but the signal from the beat note is replaced by a signal from another VCO. Both oscillators have the same settings (i.e., carrier frequency, tuning range), and are assumed to have the same noise level.

Electronic Noise and Shot Noise

To measure electronic noise in the RFPD, we can observe it at the V_{fb} (with the input light blocked off, and the feedback to the VCO removed). Following Fig. 4.6, we can write,

$$V_{fb} = \delta n DGA. \quad (4.8)$$

But the final noise due to the electronic noise that shows up in the beat signal is $\delta n/A$ (Eq. 4.7). Hence, the electronic noise shows up in the beat noise as,

$$\frac{\delta n}{A} = \frac{V_{fb}}{DGA} = \frac{V_{fb}}{\text{Open Loop Gain}}. \quad (4.9)$$

The open loop gain DGA can be measured from the PLL setup. Similarly, noise due to the shot noise can be measured with the same method. But instead of blocking the light, we use a white light source with the power to match the output level of that from the beat. Then measure the noise due to the white light.

4.7 Photothermal Noise

As discussed in section 2.7, fluctuation in laser power changes the effective cavity length via the thermoelastic and thermorefractive coefficients. In the case of a beam whose intensity fluctuation is shot noise limited, the photothermal noise is negligible compared to Brownian thermal noise and thermoelastic noise [76]. However, for a laser with significant intensity noise above the shot-noise limit, the photothermal noise can be much higher. In the case of the one-laser setup, this excess photothermal effect appears in both cavities as a common-mode noise. However, this is not the case for the two-laser setup, and so the photothermal effect has to be carefully characterized and factored into the noise budget. By using a set of quarter wave plate, EOAM and a PBS, in each path to modulate the input power (see Fig. 3.8), we can observe the corresponding modulation in the beat note frequency using the PLL readout. The results are comparable with the calculations

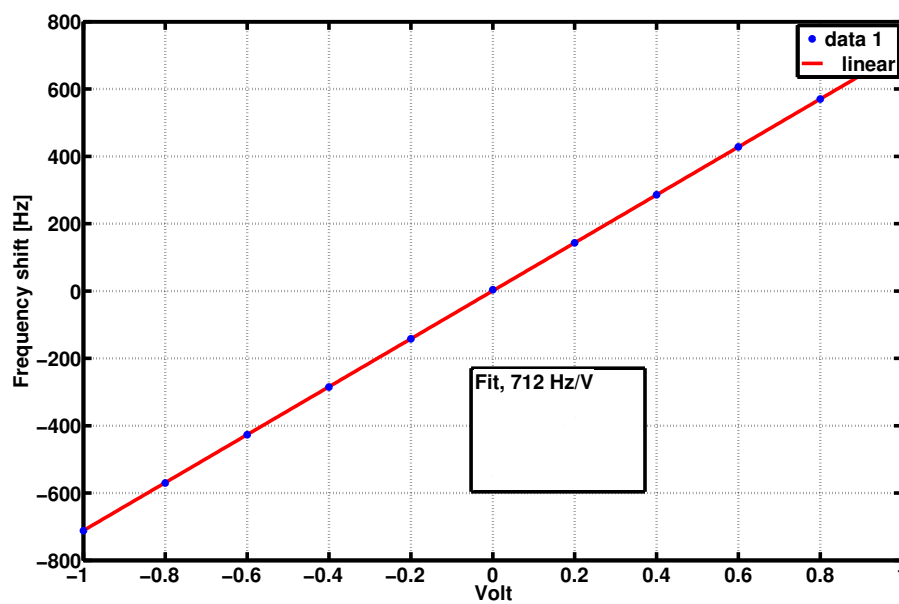


Figure 4.7: An example of a calibration measurement for PLL, the carrier frequency is 160 MHz with 1 kHz tuning range. The output frequency, which can be measured by a spectrum analyzer or a frequency meter, shifts from the central frequency due to the input voltage provided by a low noise voltage calibrator. The fitted slope, 712 Hz/V, is the actuator gain, A , in the block diagram. This actuator gain is approximately flat in our bandwidth of interest. Use this factor to convert the electronic control signal to the beat note frequency noise.

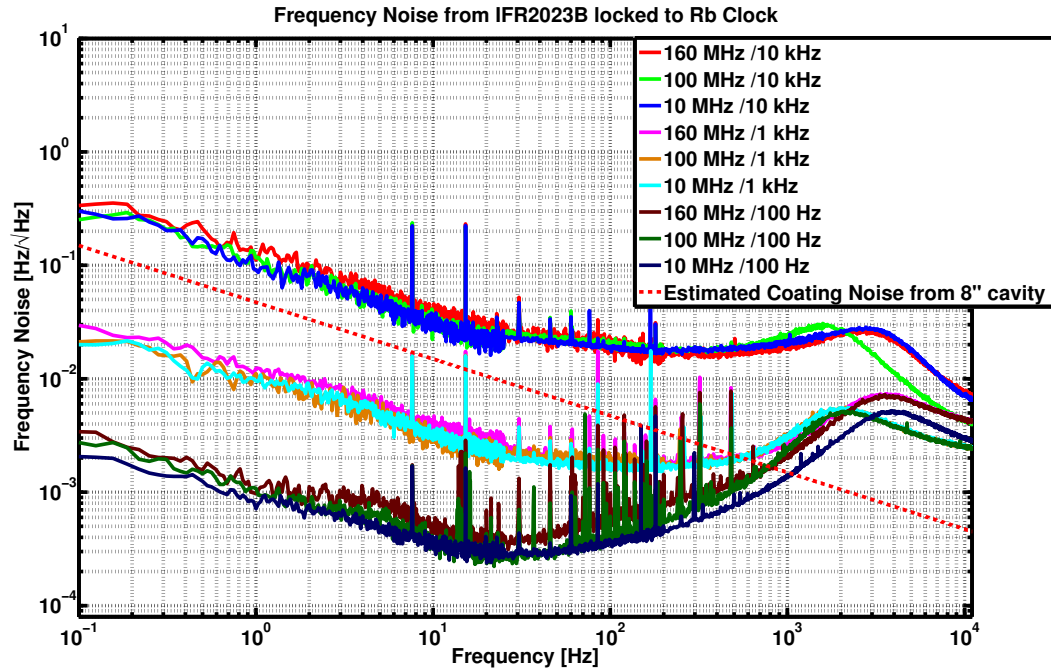


Figure 4.8: Frequency noise from VCO (from IFR2023A and IFR2023B) in PLL setup. The measurements are performed from three carrier frequencies, 10 MHz, 100 MHz, and 160 MHz each with three different tuning ranges at 100 Hz, 1 kHz, and 10 kHz. The setup is similar to what is shown in Fig. 4.5, but the RFPD is replaced by another similar VCO with the same setup. Both oscillators are locked to a 10 MHz Rb clock as a frequency reference to suppress their frequency noise. A transformer is added between the clock and each oscillator to prevent ground loop. The calibration, A (cf. Fig. 4.6), is measured from each setup. For the chosen carrier frequencies, the calibration depends only on the frequency tuning range. From the results, we can conclude that the smaller the tuning range, the lower the noise. However, the noise level seems to be comparable around 1 kHz regardless of the tuning range. We choose 1 kHz tuning frequency range as a default setup because coating brownian noise is still observable up to almost 1 kHz and the phase locked loop can be locked sufficiently long enough.

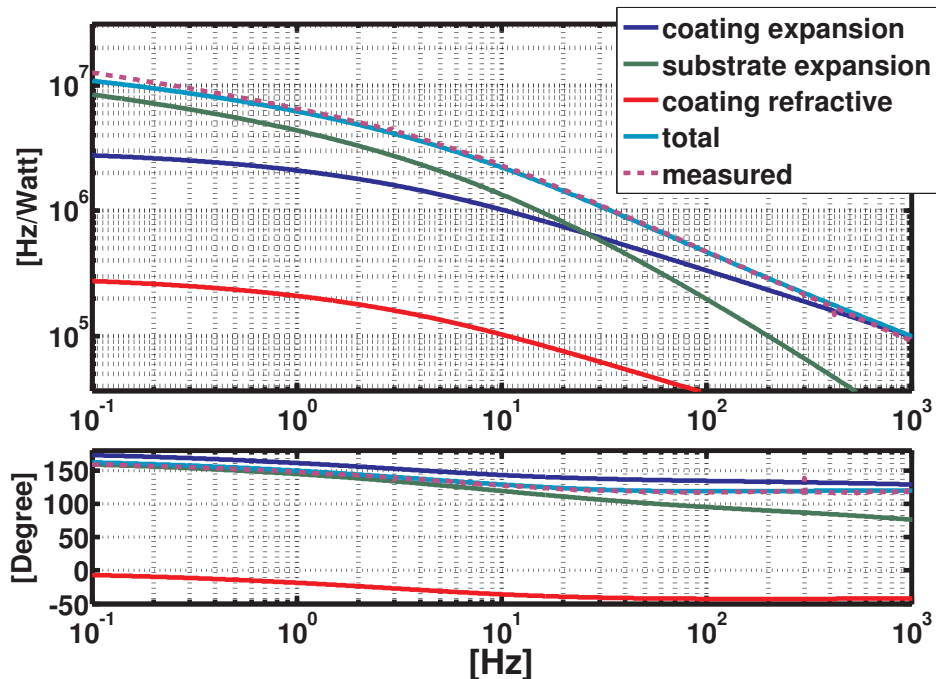


Figure 4.9: A swept sine measurement of beat note frequency fluctuation in response to photothermal noise. Both the amplitude (top) and phase response (bottom) agree with the calculations from Farsi et al. For our coatings, the greatest effects are thermal expansion from substrate and coating. The phase plot shows that the calculation of thermorefractive effect is out of phase with thermoelastic effect from both the coating and the substrate, as one would expect. The measurement is made possible with high SNR because of the PLL is not sensitive to amplitude noise from the modulation.

given in Farsi et al. [85] with the assumption of 5 ppm absorption on each mirror, see Fig. 4.9. Together with the measured RIN in the transmitted cavity beams, the estimated frequency noise due to photothermal noise can be added to the noise budget.

4.8 Noise from Ambient Temperature

The ambient temperature, i.e., temperature fluctuations in the room or the voltage noise in the heater around the vacuum tank, change the cavities length via thermal expansion coefficient. By placing the two cavities side by side, the noise becomes common mode between the two. The frequency of the laser locked to the cavity with length L is

$$\nu_i = \frac{n_i c}{2L_i}, \quad (4.10)$$

where subscript i denotes the two cavities, n is the axial mode number. The deviation in frequency due to thermal expansion of the spacer, to the first order, is

$$\delta\nu_i \sim -\frac{n_i c}{2L_i} \alpha \delta T. \quad (4.11)$$

Then, the frequency noise between the two is

$$\delta\nu_1 - \delta\nu_2 = -\alpha \delta T \left(\frac{n_1 c}{2L_1} - \frac{n_2 c}{2L_2} \right) \quad (4.12a)$$

$$\delta\nu_{beat} = -\alpha \delta T \nu_{beat}. \quad (4.12b)$$

Here ν_{beat} is the frequency of the recombined beams. It is around 160 MHz and 120 MHz in the prototype setup, and in the 2-laser setup, respectively. δT is the ambient temperature fluctuation near the cavities. It can arise from the ambient room temperature or from the voltage noise on the heater. The temperature fluctuations transfers through the heat insulation, the vacuum tank to the cavities. Each stage behaves as a low pass filter with a pole around sub-Hz level making the noise become very small at the bandwidth of interest. To estimate the effect at 1 Hz, δT_{room} is $\sim 10^{-4} K/\sqrt{Hz}$, and δT_{heater} due to the supplying voltage noise is $\sim 10^{-7} K/\sqrt{Hz}$, resulting in the beat frequency noise well below $10 \mu Hz/\sqrt{Hz}$. However, the real effect can be larger because of the temperature gradient due to close by thermal sources from electronic devices or people, or non-uniformity in the shape of the heat insulation or the heater. These factors lead to higher noise level, but it is still not significant compared to other noise sources. Although the temperature noise does not dominate in our measurement band, the beat frequency drift due to the temperature requires a larger tuning range for PLL and this creates a noise floor in the measurement.

Chapter 5

AlGaAs Crystalline Coatings

Gallium arsenide, and aluminum gallium arsenide ($\text{Al}_x\text{Ga}_{1-x}\text{As}$ with x varied between 0 and 1 to indicate the amount of Al) are semiconductor materials. Because of their similar lattice structure, they can be grown in alternated layer form while preserving their structure. Together with their suitable optical properties for light at 1064 nm, coatings fabricated from alternating layer of GaAs and $\text{Al}_x\text{Ga}_{1-x}\text{As}$ can be use as a high reflective coating. Due to their crystalline structure, the mechanical loss is expected to be much smaller than that from amorphous materials like SiO_2 and Ta_2O_5 . This chapter will explore AlGaAs properties as high reflective coatings. We will see that due to its low loss, Brownian thermal noise will not be the limiting noise source anymore. Instead, substrate thermoelastic noise and coating thermo-optic noise will be the dominant sources, for our cavity geometry. This situation lets us study more about coating thermo-optic noise which is not observable in the $\text{SiO}_2/\text{Ta}_2\text{O}_5$ coating. Since thermo-optic noise is a combination of thermoelastic and thermorefractive noise, we can partially cancel it with a careful design of coating structure. A successful design can set a new fundamental limit of displacement noise in a reference cavity.

5.1 History of AlGaAs Usage

Doublets of GaAs and $\text{Al}_x\text{Ga}_{1-x}\text{As}$, or collectively called AlGaAs, grown with molecular beam epitaxial method (MBE), has been used since 1980s as a high reflective device in vertical-cavity surface-emitting lasers (VCSELs) for wavelengths from 650 nm to 1300 nm [135]. Because of its application in laser and optic devices, their optical parameters and material parameters, e.g., refractive indices, thermal expansion coefficients, and thermorefractive coefficients, have been studied extensively [136, 137]. Due to its crystalline structure, AlGaAs is expected to have very low mechanical loss. This makes it a good candidate for a low loss coating material for high reflective mirrors. Nevertheless, their usage was limited to small devices like VCSELs because the structure has to be grown on a lattice-matched material, for example, GaAs or germanium which are not suitable for used as a mirror substrate at 1064nm because of its high optical absorption and cost.

This problem was overcome when the epitaxial lift off (ELO) technique was developed. This allows an AlGaAs wafer structure to be grown on a lattice-matched substrate, then removed and applied on a target substrate. The ELO technique has been widely used, for examples, in solar cell technology [138], LED [139], and lasers [140], where AlGaAs thin films are transferred to silicon, sapphire, glass substrates. As a result, high reflective mirrors with AlGaAs coatings on fused silica substrates are made possible. However, the coatings can only be applied to mirrors with radius of curvature of 1.0 m or larger. The smaller radius of curvature will result in excess stress in the coating which can create dislocation in the lattice structure, and it cannot be bonded on the substrate. Thus, for this dissertation, the radius of curvature of the mirrors for AlGaAs coating will be at 1.0 m.

Since a possibility to use AlGaAs as a coating material had shown up, a study to determine its loss followed. Ring down measurements of thin film AlGaAs had been done. Unlike the ring down measurements performed on SiO_2/Ta_2O_5 where the coating has to be deposited on the substrate, this ring down measurement was performed on a stand-alone thin film AlGaAs. As a result, errors associated with the substrate loss, the dilution factor (see appendix C.2), can be removed, and the loss in the thin film can be measured with higher accuracy. The wafer samples were created with gas-phase etching technique [141], with nodal support to minimize structural loss for each bending mode [142]. The loss angle at room temperature is measured to be 2.5×10^{-5} , and down to 1.1×10^{-5} at 20 K) where the coatings still have low optical loss. Together with the bonding technique, the wafer can be grown, transferred, and attached on a fused silica substrate which, is widely used in high quality optics for 1064 nm wavelength. A direct observation of noise on a Fabry–Perot cavity formed by AlGaAs coatings on fused silica substrates has been measured. The PSD of the displacement noise is around 10 times lower than that of mirrors with SiO_2/Ta_2O_5 coatings [143].

The refractive index of $Al_xGa_{1-x}As$ is a monotonic function of x , cf. Tab. C.1, so it is best to use a heterostructure of AlAs/GaAs for maximum contrast for reflectivity. But AlAs oxidizes quite fast in atmosphere, a small amount of Ga has to be added to make the substance more stable. In this work, the amount of Ga will be 8 percent by molar, and it is addressed as $Al_{0.92}Ga_{0.08}As$. The end layers of the coating wafer have to be GaAs on both sides. A table of AlGaAs material parameters can be found in appendix C.

5.2 Thermo–Optic Noise and Coatings Optimization

Because of the high values of thermal expansion and thermal refraction coefficients of AlGaAs, coating thermo–optic noise, as estimated by Eq. 2.22 become significant for a standard QWL coating structure. In this section, we will discuss about AlGaAs coating thermo–optic noise and a plan to reduce it.

5.2.1 Thermal Noise in AlGaAs Coatings

A noise budget of AlGaAs coatings on a fused silica substrate is shown in Fig. 5.1. Coating Brownian noise is not the dominating noise source in this situation. Coating thermo-optic noise will be the limiting noise source around 100 Hz and above.

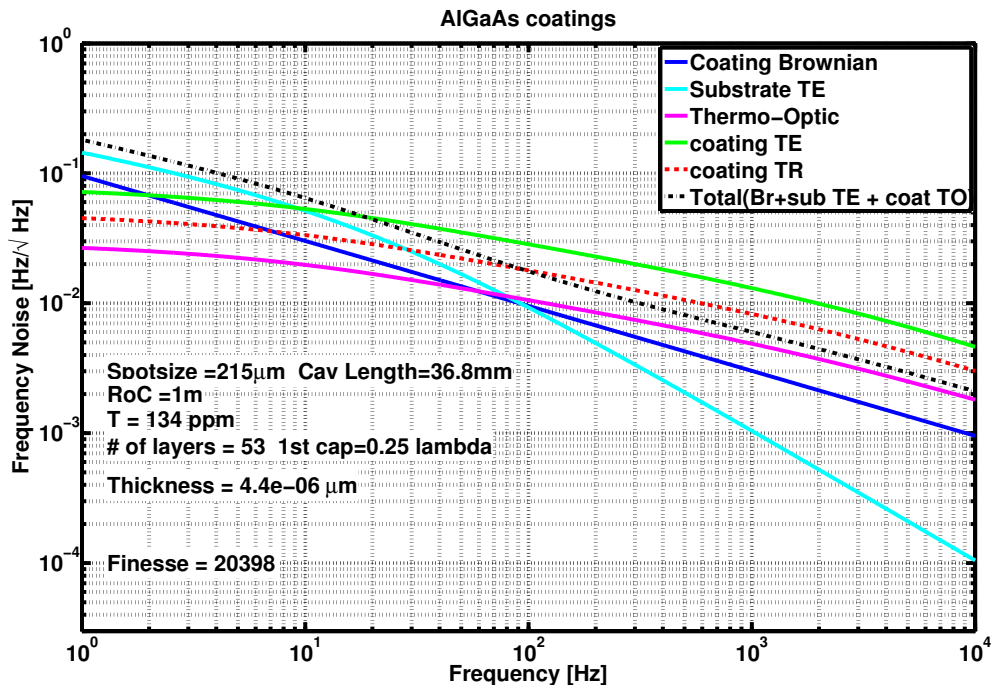


Figure 5.1: Noise budget for AlGaAs coatings with quarter wavelength structure, 53 layers. Due to the low mechanical loss, thermoelastic from substrate is dominating at low frequency while thermo-optic noise in coating becomes dominant at frequency above 100 Hz. The total noise is plotted in black dashed line. Other relevant optical properties are shown in the plot.

As discussed in Ref. [74], the effects from thermoelastic and thermorefractive noise in coating layers cancel each other. By carefully designing the coatings layers thickness, we can reduce the total thermo-optic noise while achieving the desired reflectivity of the coatings.

Before we proceed to the optimization discussion, let's investigate if TO cancellation is possible with a QWL structure. The contributions from thermoelastic and thermorefractive are proportional to $\bar{\alpha}_c d$ and $\bar{\beta} \lambda$, respectively, cf. Eq. 2.22. So thermoelastic effect is proportional to the coating thickness, while thermorefractive effect is roughly independent from the coating thickness (the effect is mostly contributed from the top layers). For the QWL structure with 53 layers, thermoelastic noise is higher than thermorefractive noise. By reducing the total number of layers, thermoelastic noise can be varied until it is comparable to thermorefractive noise to achieve thermo-optic cancellation. This is possible at 33 layers. The noise budget is shown in Fig. 5.2. However, the transmission is around 3000 ppm, and it results in a rather low cavity finesse (around 1,000).

Another method is to add a half-wave cap of AlGaAs on the top layer of a QWL structure to mitigate thermo-optic noise [143]. This method is intended for a low transmission mirror (81 layers, 5 ppm). The cap changes the effective β (cf. Eq. D.7) while maintaining the correct inference condition. However, AlGaAs is not suitable to be used as an end cap because it can oxidize and change its optical properties.

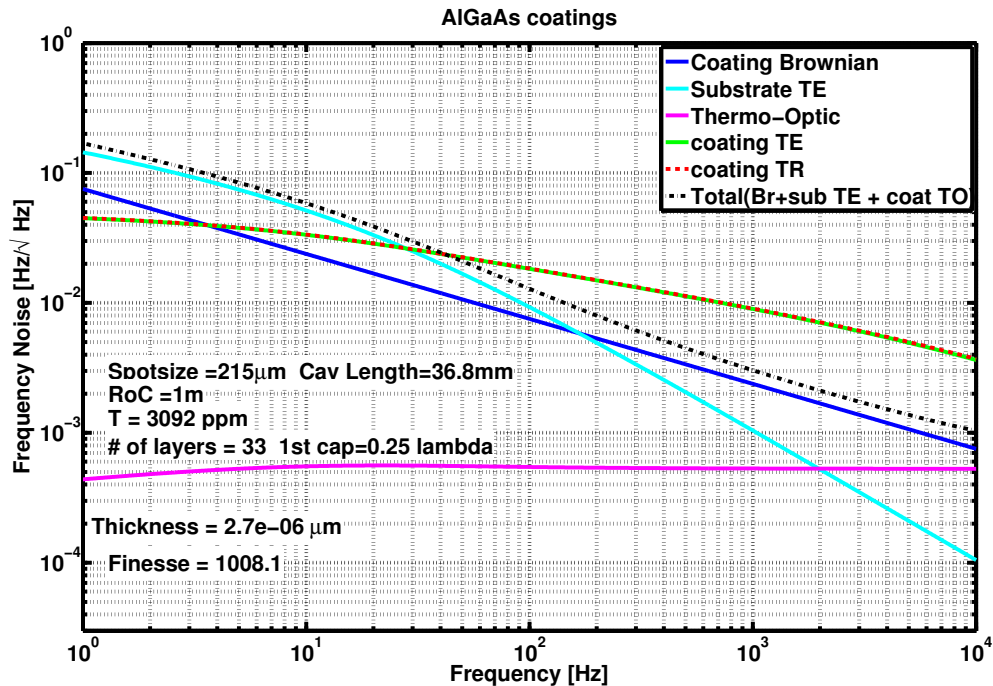


Figure 5.2: Noise budget of AlGaAs coating QWL structure, 33 layers in total.

5.2.2 Optimization Consideration

The main goal of the optimization is to make thermo optic noise below other noise sources which cannot be adjusted (e.g., coating Brownian noise, substrate thermoelastic noise), and to demonstrate that such coating is possible. However, as we alter the layer thickness to reduce thermo-optic noise, other optical properties of the coating is changed too. Here we explain some considerations that have to be monitored during the optimization.

- **Transmission:** The desired transmission has to be around 100 ppm to 300 ppm. Smaller transmission (more reflectivity) leads to more power build up in the cavity and higher photothermal noise, cf. sections 2.7 and 4.7. The transmitted power also depends on the mirrors' transmission when the mirrors have loss (from absorption or scatter). Lower transmission means that the light will circle in the cavity more often, and lose power each time it reflects

of the mirrors. The transmitted power from the cavity is given by [144]

$$P_{trans}/P_{in} = \frac{T^2 Re^{-\alpha}}{R(1 - Re^{-\alpha})^2}, \quad (5.1)$$

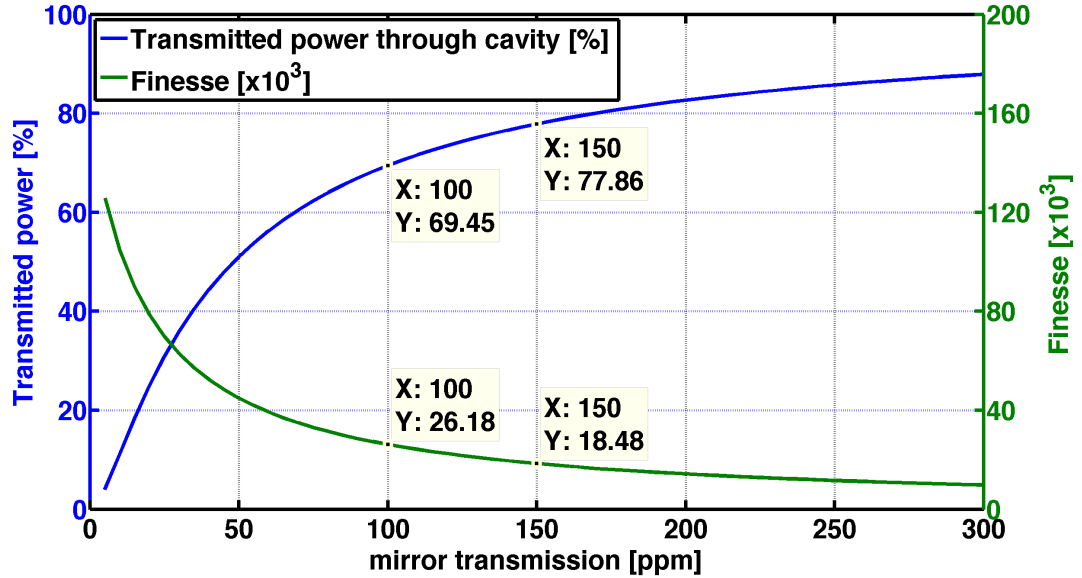


Figure 5.3: Transmitted power behind the cavity (left y-axis), and cavity finesse (right y-axis) as a function of mirror's transmission. The calculation assumes each mirror has 10 ppm loss.

where T is the power transmission, α is the roundtrip loss. Higher transmission results in a low finesse cavity which reduces the gain of the frequency discriminator (see sections 4.3, and 4.4) and compromises the frequency stabilization performance.

- Phase of the reflected light at the top surface:** to avoid surface burning, the reflected phase at the surface must cancel the incoming phase, the node of the standing wave formed in the cavity is at the coating surface. In general, for a normal incident wave reflecting from the interface between medium 1 and 2, the reflected light will have a phase shift of 0 or 180 degrees depending on the refractive indices of the two medium. For reflection from multiple medium with various thickness, the back reflection from other interfaces will sum up at the first surface resulting in a complex value of reflectivity r . Generally, for a coating with QWL structure, the reflection phase will be close to 180 degrees, see different cases of end caps with n_H or n_L in appendix D. The optimization will change the path length in coating layers and the effective phase of the coating reflectivity will not be close to 180 degrees. When that happens, the node of the standing wave will move away from the coating surface (see Fig. 5.4) and certain power can build up on the surface during the light circulation. If there are any impurities on the surface, they might be burnt from the intra-cavity power. These burnt impurity will create

more contamination in the system.

This issue prevents us from optimizing the coating by altering only the cap layer thickness and leave the rest of the layers in QWL structure. Remember that tuning the cap thickness can change β of the coating effectively [145]. But the reflected phase will be wrong.

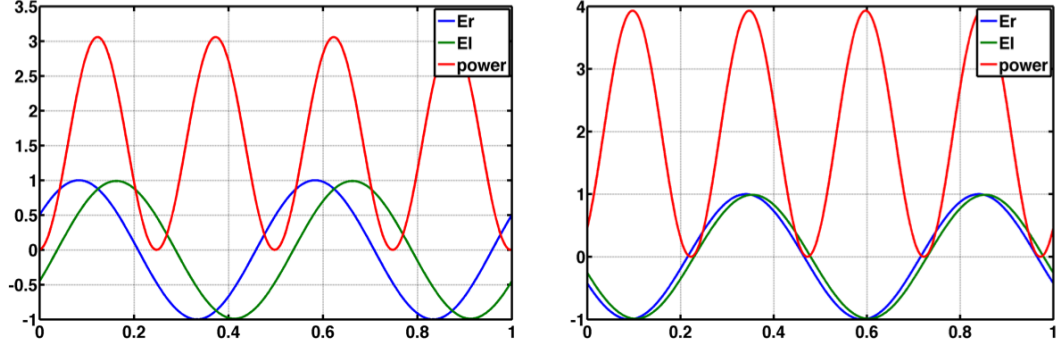


Figure 5.4: The power inside a cavity shown in red which is the square of the sum of two electrical fields propagating from left and right directions. The x-axes are the cavity beam line position normalized by the cavity length such that the coating surfaces are at 0 and 1. In this case, the cavity length is twice the beam wavelength. The y-axes represent the electric field and power in arbitrary units. Left, when the reflected phase of the mirror is close to 180 degrees, the power at the mirror surfaces (at 0 and 1 on the x-axis) will remain close to zero at all time. Right, when the reflected phase is off by 40 degrees, the power on the mirrors' surfaces will not always be zero.

In case of reflectivity with phase shift away from 180 degrees, the power build up on the cavity can be approximated as

$$E_{tot} = E_r + E_l \quad (5.2a)$$

$$\approx E_r + rE_r = E_r(1 + r) \text{ for high reflectivity mirror} \quad (5.2b)$$

E_r and E_l are electric fields circulating the cavity in right and left directions. The reflectivity can be written as $r = |r|e^{i\pi}e^{i\delta}$, where δ represents the phase shift away from 180 degrees. If $\delta \ll 1$ and $|r| \approx 1$ the reflectivity can be approximated as $r \approx -e^{i\delta}$. Then the power on the surface is

$$P_{tot} = |E_{tot}|^2 \approx |E_r|^2 |1 - e^{i\delta}|^2 \quad (5.3a)$$

$$\approx |E_r|^2 (\delta)^2 \quad (5.3b)$$

$$\approx \frac{\text{Finesse}}{\pi} E_{in}^2 \delta^2 = \frac{\text{Finesse}}{\pi} P_{in} \delta^2. \quad (5.3c)$$

For our parameters, the finesse is around 20,000, $P_{in} = 1 \text{ mW}$, and $\delta \approx 6$ degrees, the power on the coating will be $\approx 70 \text{ mW}$. With the spot size around $200 \mu\text{m}$, the intensity is around 1 MW/cm^2 (with a safety factor of 2). This intensity level is acceptable for general lab optics (the damage threshold can go up to 10 MW/cm^2 for general laser optics¹), and the risk of burning any contamination on the surface should be low.

5.2.3 Uncertainties in Material Parameters

Uncertainties in material parameters also lead to deviations from the desired coating properties. For example, variations in α and β will directly compromise the cancellation in thermo-optic noise. Refractive indices are also one of the most important factors coming into the calculation. The amplitude of the reflected phase depends on the refractive indices values. In addition, they also change the optical path length in the layers. Since the optimization deals with the optical thickness in each layer, the associated physical thickness is given by

$$t = \text{dOpt} \times \frac{\lambda}{n_0}, \quad (5.4)$$

Where n_0 is the nominal refractive index. Typically, the physical thickness is being controlled during the crystal growth. As a result, if the actual value of refractive index is $n' \neq n_0$, the optical thickness becomes

$$\text{dOpt}' = \text{dOpt} \times \frac{n'}{n_0}, \quad (5.5)$$

and the error in optical thickness directly affects the phase of the reflected beam. For the optimized coating, we have to make sure that the coating properties will still be acceptable even with some uncertainties in the material parameters, see Tab. 5.1 for the approximated uncertainties of AlGaAs properties.

Parameters	GaAs	Al _{0.92} Ga _{0.08} As
Heat capacity, C ($\times 10^6$) [J/Km^3]	$1.754 \pm 5\%$	$1.698 \pm 5\%$
Thermal conductivity, κ [W/mK]	$55 \pm 5\%$	$70 \pm 5\%$
Young's modulus, Y [GPa]	$100 \pm 20\%$	$100 \pm 20\%$
Poisson's ratio, σ	$0.32 \pm 10\%$	$0.32 \pm 10\%$
Thermal expansion, α ($\times 10^{-6}$) [$1/K$]	$5.7 \pm 5\%$	$5.2 \pm 5\%$
Thermorefractive, β ($\times 10^{-6}$) [$1/K$]	366 ± 7	179 ± 7
Refractive index, n @1064nm	3.51 ± 0.03	3.0 ± 0.03

Table 5.1: AlGaAs material parameters and the estimated uncertainties.

¹<https://marketplace.idexop.com/store/IdexCustom/PartDetails?pId=145>

5.2.4 Errors Due to Manufacturing Process

Besides the uncertainties from material parameters, the coating fabrication process introduces errors in the coating properties in a few following ways:

- **Thickness Control:** Thickness calibration might be off causing the layers thickness to deviate from the desired value. As a result, the error is not random among each layer. It is rather constant in each layer type, i.e., all the layers from the same material (n_L or n_H) have the same percentage of error. The errors will have the same sign, that is, if one material is thicker, another is also thicker, but the magnitudes are uncorrelated. In addition, GaAs has better thickness control than $\text{Al}_{0.92}\text{Ga}_{0.08}\text{As}$. The standard deviation of GaAs is about 0.5 %, while that of $\text{Al}_{0.92}\text{Ga}_{0.08}\text{As}$ is about 1 % [146].
- **Truncated Thickness:** The thickness control during the coating process can be controlled down to 0.5 angstrom [146]. The specification in the design with smaller resolution has to be rounded up to the nearest 0.5 angstrom. This is similar to random variations in the thickness control, see Fig. 5.5. Fortunately, the effect is much smaller than the averaged coating layer (around 800 Å), and it will not be a problem for the optimized structure.

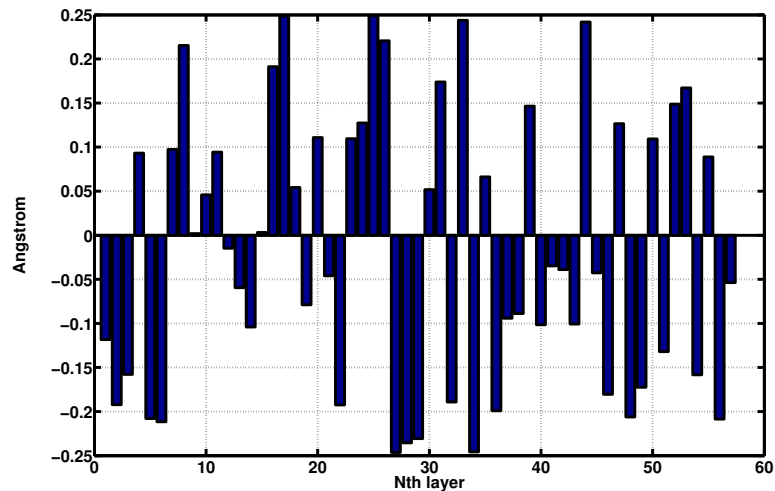


Figure 5.5: Thickness deviation from the design due to the truncation for the optimized coating structure.

- **Error in the Al content:** The material properties of $\text{Al}_x\text{Ga}_{1-x}\text{As}$ are usually dependent on x (the amount of Al), see Tab. C.1. According to the coating vendor, the variations in Al content is $x = 92\% \pm 0.6\%$ [146]. For the optimization, one of the most important parameter is the refractive index. It can be extrapolated as $n(x) = 3.48 - 0.578x$ [147, 148]. If x is altered by 6%, the refractive index changes by 0.0035. This value is almost a factor of ten smaller

than the standard deviation of n_L and n_H used in the calculation, cf. Tab. 5.1. This is also true for other parameters. Hence, the effect from the uncertainty in Al amount is negligible.

5.2.5 Optimization Method

The optimization can be done by varying the layers thickness while minimizing a cost function which is defined by the properties we want to control (i.e., thermo-optic noise level, transmission, and reflected phase). In general, the cancellation will not work at all frequencies due to the finite thickness of the coating. So, the optimization can be chosen at a single frequency range. For our calculation, the target frequency f_0 of the thermo-optic cancellation was set to 100 Hz, which is about the central frequency of our detection band. The cost function y is given by

$$y(S^{TO}, T, \delta) = S^{TO}(f_0) \cdot w_1 + \left(\frac{T - T_0}{T_0}\right)^2 \cdot w_2 + \delta^2 \cdot w_3, \quad (5.6)$$

where w_1, w_2 , and w_3 are weights assigned to each parameters, T_0 is the target transmission set around 200 ppm, δ is the reflected phase shift from π .

To search for the optimized structure, we used a MATLAB built in function *fmincon*² that is used for finding minimum of a constrained nonlinear multivariable function.

This method will give us the coating structure with the minimized cost function. Note that the question about whether the solution will return the absolute minimum is not the main concern here. Rather, we want to ask if the coating will work even if there are uncertainties in the material parameters. One of the important parameters for the coating properties are the refractive indices. To make sure that the designed structure is relatively insensitive to the parameters, we modified the cost function to be

$$y_2 = \sum_{n_H} \sum_{n_L} y(S^{TO}, T, \delta; n_H, n_L) \quad (5.7)$$

The new cost function is the sum of cost functions from different values of n_H and n_L . This will ensure that the optimized coating's properties will still not be compromised even though the values of refractive indices have some small errors. For our optimization, $n_H = \{3.47, 3.50, 3.53\}$, and $n_L = \{2.97, 3.00, 3.03\}$. As a result, the optimized structure with the modified cost function becomes less sensitive to the variations of refractive indices compared to another optimized structure with a simple cost function, see Fig. 5.7 and Fig. 5.8. Finally, we checked how the optimized coating changed with all uncertainties discussed in section 5.2.3 and section 5.2.4. By running a Monte Carlo simulation when random errors were added to the parameters. The histograms of coating properties are shown in Fig. 5.12. Around 70 % of the results, the coating properties will meet the requirements ($100 < T_0 < 300$, $\delta < 7$ degrees, and $S_{TO} < 1.5 \times 10^{-39} m^2/Hz$). Details of the final

²<http://www.mathworks.com/help/optim/ug/fmincon.html>

optimized design are reported in Fig. 5.10 and Tab. 5.2. Coating thermo-optic noise is predicted to be well below other noise source from DC to a few kHz, see Fig. 5.9.

One way to verify how well the cancellation works it to measure photothermal response of the coatings. This is similar to the measurement discussed in section 4.7. If the cancellation works, the effect will mostly be thermal expansion in the substrate. If the cancellation does not work as expect, the shape of the transfer function should provide a better hint than the direct observation from the cavities displacement noise, see Fig. 5.13.

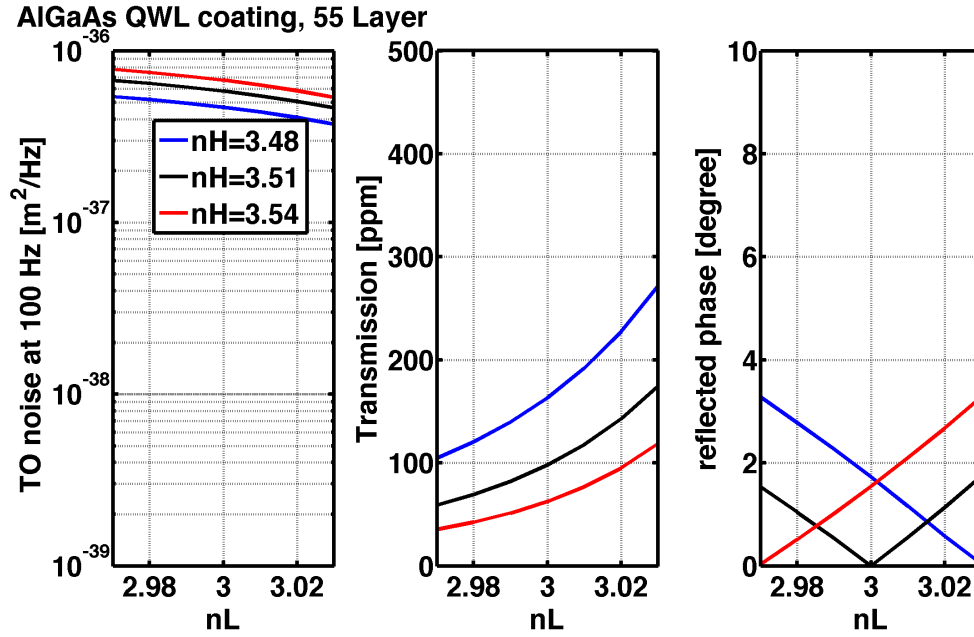


Figure 5.6: Optical properties of QWL structure with 55 layers as a function of n_H and n_L . These plots serve as baseline values used for comparison with other optimized coatings shown in Fig. 5.7 and Fig. 5.8.

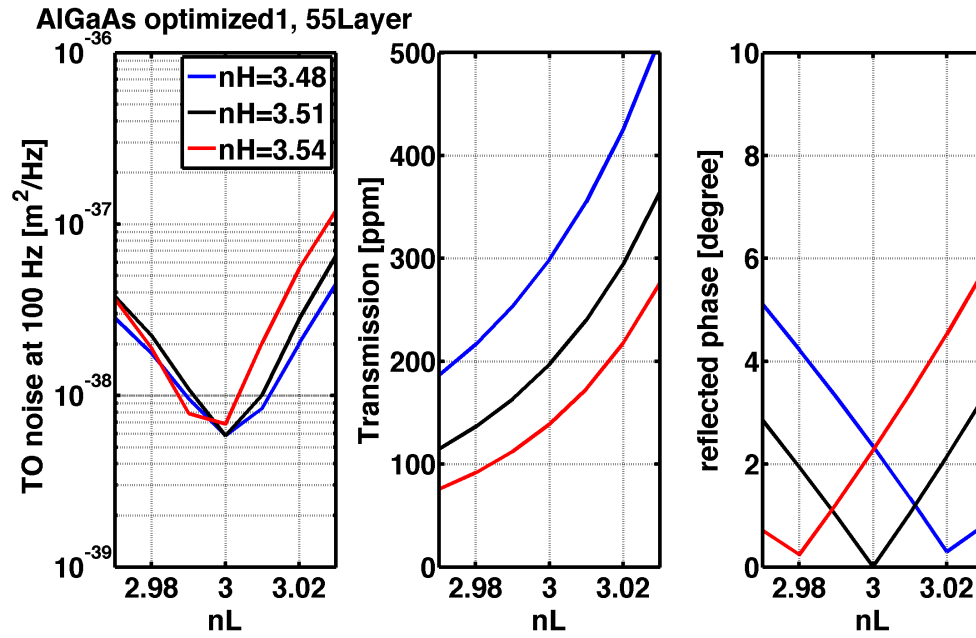


Figure 5.7: This optimization was done with a single cost function (cf. Eq. 5.6). Note that the detail of this structure is not reported here. Although, for nominal values of refractive indices, the thermo-optic cancellation is good, and the transmission is close to the required value (200ppm), the properties change rapidly as the refractive indices vary from the central values.

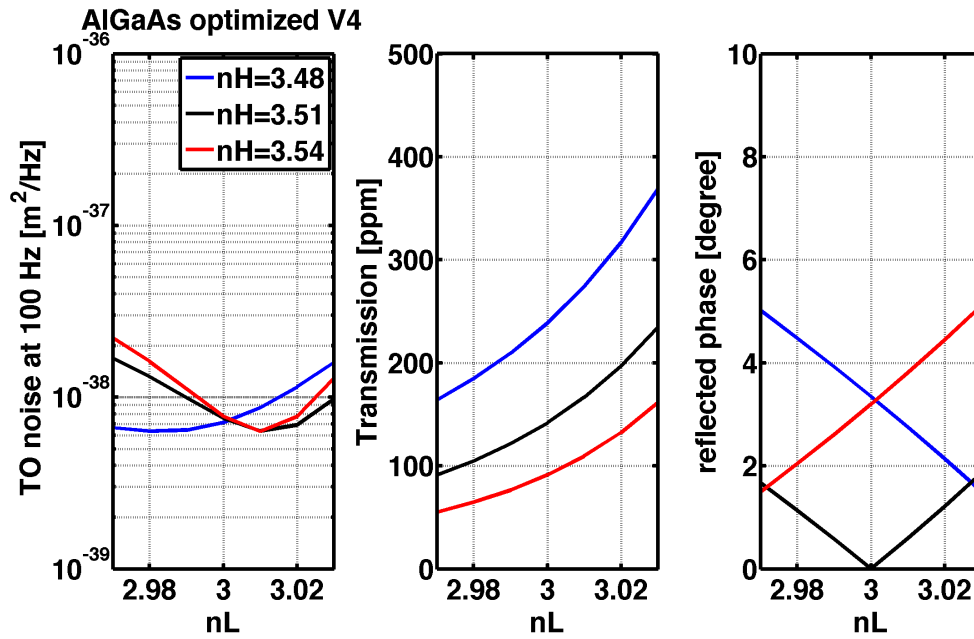


Figure 5.8: This optimization is the final design. It was done with the modified cost function (Eq. 5.7). The cancellation for thermo-optic noise is less sensitive to variations in refractive indices, and the transmission will mostly stay in the acceptable range (100–300 ppm).

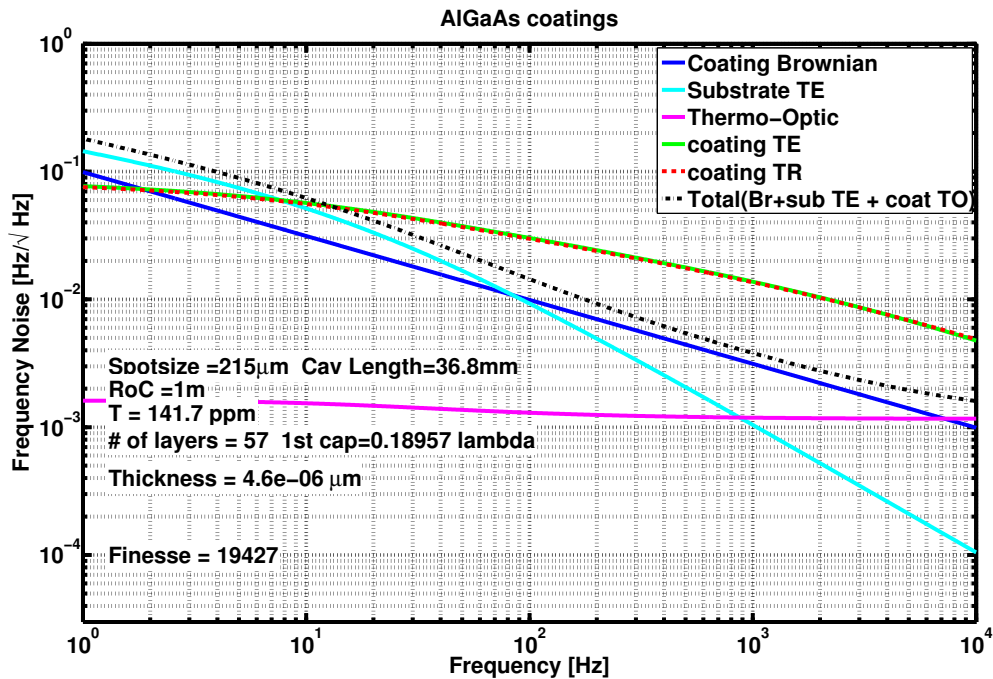


Figure 5.9: Noise budget from the optimized structure with 57 layers in total. Due to the low loss, substrate thermoelastic noise will be the dominating source from DC to around 100 Hz.

Nth Layer	optical thickness [wave-lengths]	n	physical thickness [nm]	Nth Layer	optical thickness [wave-lengths]	n	physical thickness [nm]
1(cap)	0.1896	3.480	57.95	31	0.2528	3.480	77.30
2	0.1121	2.977	40.05	32	0.2457	2.977	87.80
3	0.4995	3.480	152.4	33	0.2539	3.480	77.65
4	0.1	2.977	35.75	34	0.2447	2.977	87.45
5	0.4995	3.480	140.55	35	0.2549	3.480	77.95
6	0.1695	2.977	60.55	36	0.2439	2.977	87.15
7	0.2760	3.480	84.4	37	0.2556	3.480	78.15
8	0.2145	2.977	76.7	38	0.2433	2.977	86.95
9	0.2510	3.480	76.75	39	0.2562	3.480	78.35
10	0.2388	2.977	85.35	40	0.2427	2.977	86.75
11	0.2403	3.480	73.5	41	0.2566	3.480	78.45
12	0.2508	2.977	89.5	42	0.2423	2.977	86.60
13	0.2368	3.480	72.4	43	0.2571	3.480	78.6
14	0.2553	2.977	91.25	44	0.2420	2.977	86.50
15	0.2375	3.480	72.6	45	0.2574	3.480	78.70
16	0.2571	2.977	91.9	46	0.2417	2.977	86.35
17	0.2391	3.480	73.15	47	0.2577	3.480	78.80
18	0.2564	2.977	91.65	48	0.2414	2.977	86.25
19	0.2414	3.480	73.8	49	0.2579	3.480	78.85
20	0.2550	2.977	91.15	50	0.2412	2.977	86.20
21	0.2437	3.480	74.5	51	0.2581	3.480	78.90
22	0.2533	2.977	90.50	52	0.2409	2.977	86.10
23	0.2459	3.480	75.2	53	0.2585	3.480	79.05
24	0.2515	2.977	89.90	54	0.2405	2.977	85.95
25	0.2480	3.480	75.85	55	0.2587	3.480	79.10
26	0.2498	2.977	89.3	56	0.2401	2.977	85.80
27	0.2498	3.480	76.35	57	0.2556	3.480	78.15
28	0.2482	2.977	88.7	substrate			
29	0.2514	3.480	76.85				
30	0.2469	2.977	88.25				

Table 5.2: Structure of optimized coating. The physical thickness is truncated to the next 0.05 nm for the manufacturing process.

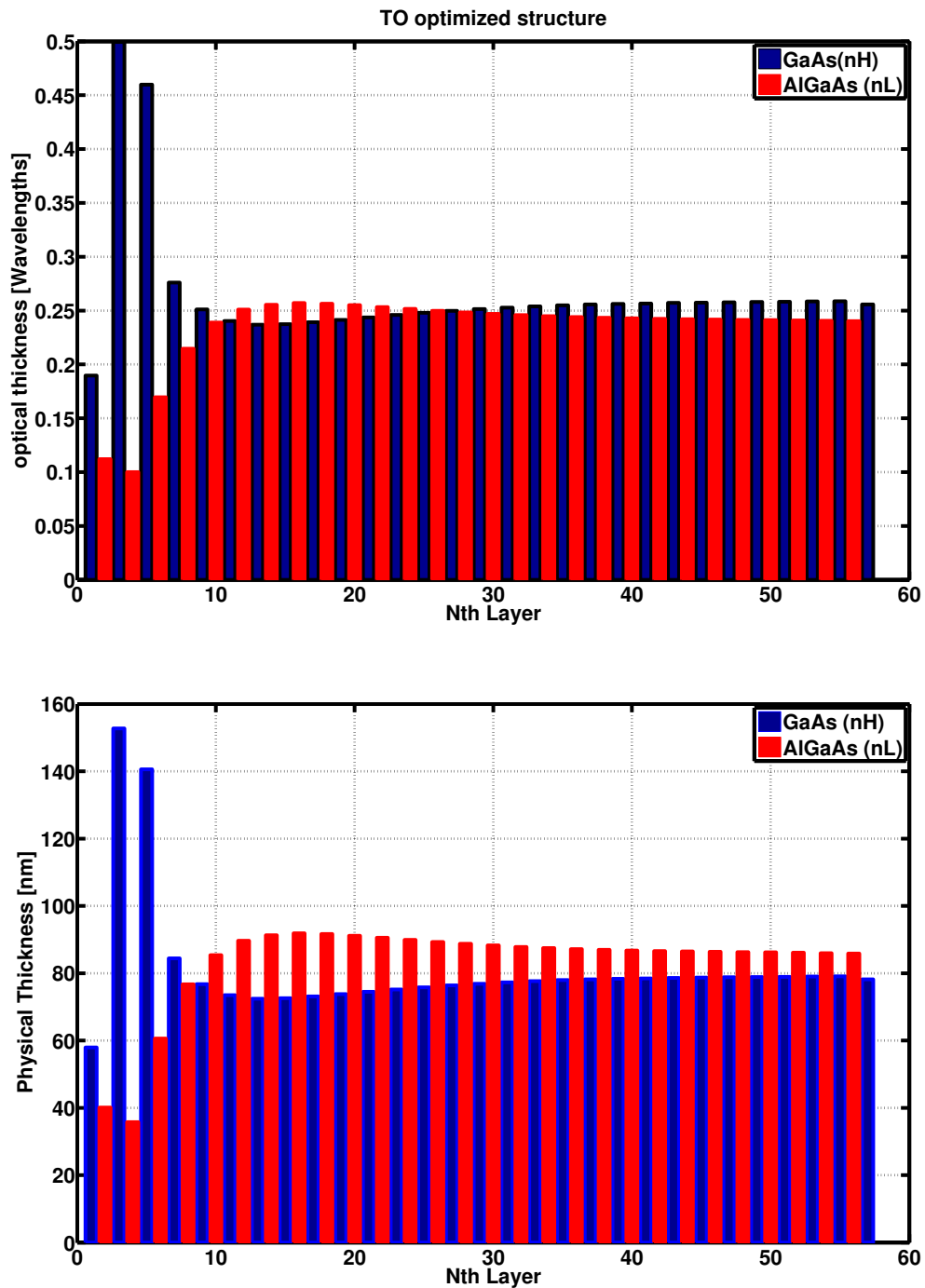


Figure 5.10: Above, the optimized structure as shown in optical thickness. Below, the same structure as shown in physical thickness. The first layer is the air-coating surface, the 57th layer is the coating-substrate surface. The plots are taken from the data in Tab. 5.2 below. From the plot, it can be seen that the first few pairs are altered away from quarter wave the most. This is expected as most of thermorefractive effect is from the very top layers, while all the coating layers contribute equally to thermoelastic effect.

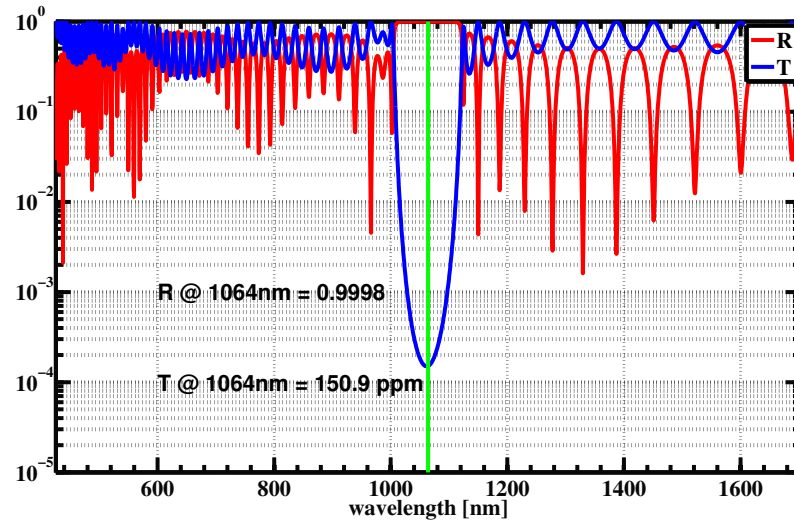


Figure 5.11: Reflectivity and transmission of the designed coating.

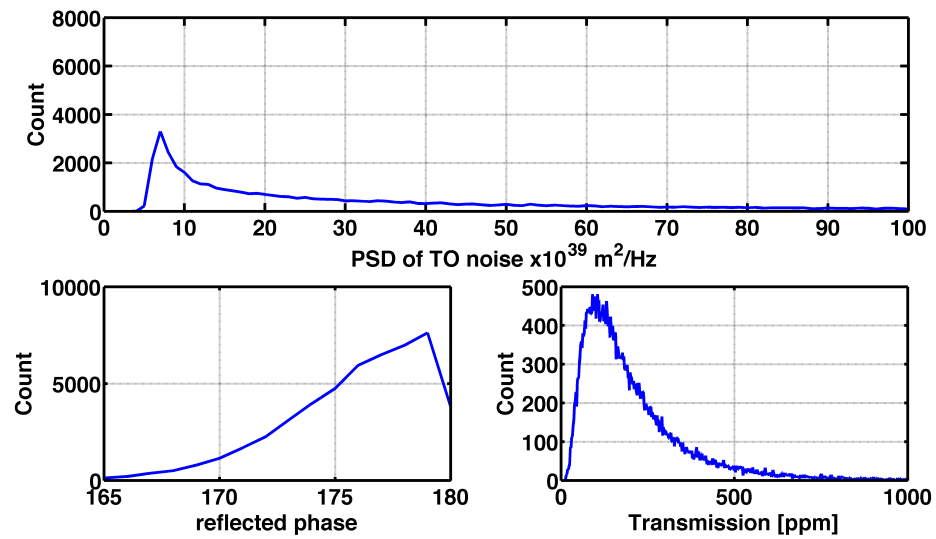


Figure 5.12: Histograms of the Monte Carlo simulations to determine optical properties of the optimized structure. Uncertainties from all considerations are added to the calculation.

5.2.6 Cavity Parameters

Cavity length / FSR	1.45 inch (3.68 cm) / 4.07 MHz
Finesse	20,267
Cavity linewidth (FWHM)/ cavity pole	201 kHz/ 100 kHz
Beam radius on the mirror	$w_0 = 215 \mu\text{m}$
mirror coatings	AlGaAs optimized coatings
mirror transmission	150 ppm
Loss in each mirror	5 ppm
Mirror radius of curvature	1.0 m

Table 5.3: Table of parameters for 1.45 inch cavity and the mirrors with AlGaAs coatings.

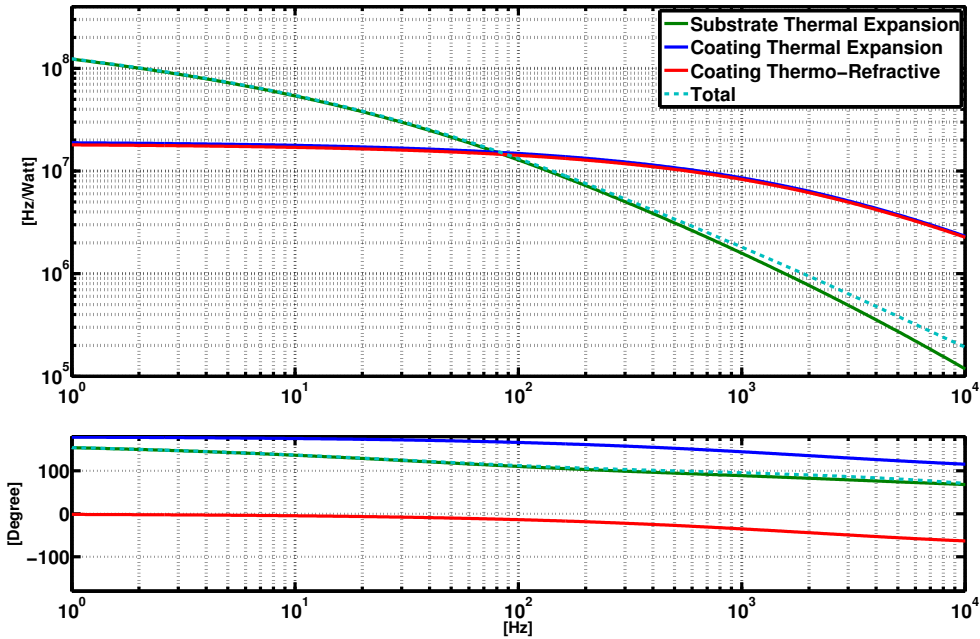


Figure 5.13: An estimated result of a swept sine measurement for photothermal effect on AlGaAs optimized coating.

5.3 Implications for Advanced LIGO

If the limiting noise of the proposed optimized coating structure is measured and the cancellation does work, we can apply the above method to find optimized structures for Advanced LIGO's test masses. The transmissions of an Input Test Mass (ITM) and an End Test Mass (ETM) are 1.4 percent and 5 ppm, respectively. The optimized structure for ITM and ETM are shown below. Here

the results are only preliminary without any Monte Carlo test. Thorough checks on uncertainties in parameters are required. The complete noise budget for Advanced LIGO with AlGaAs optimized coating is shown in Fig. 5.16. The calculation is done at room temperature with fused silica substrate.

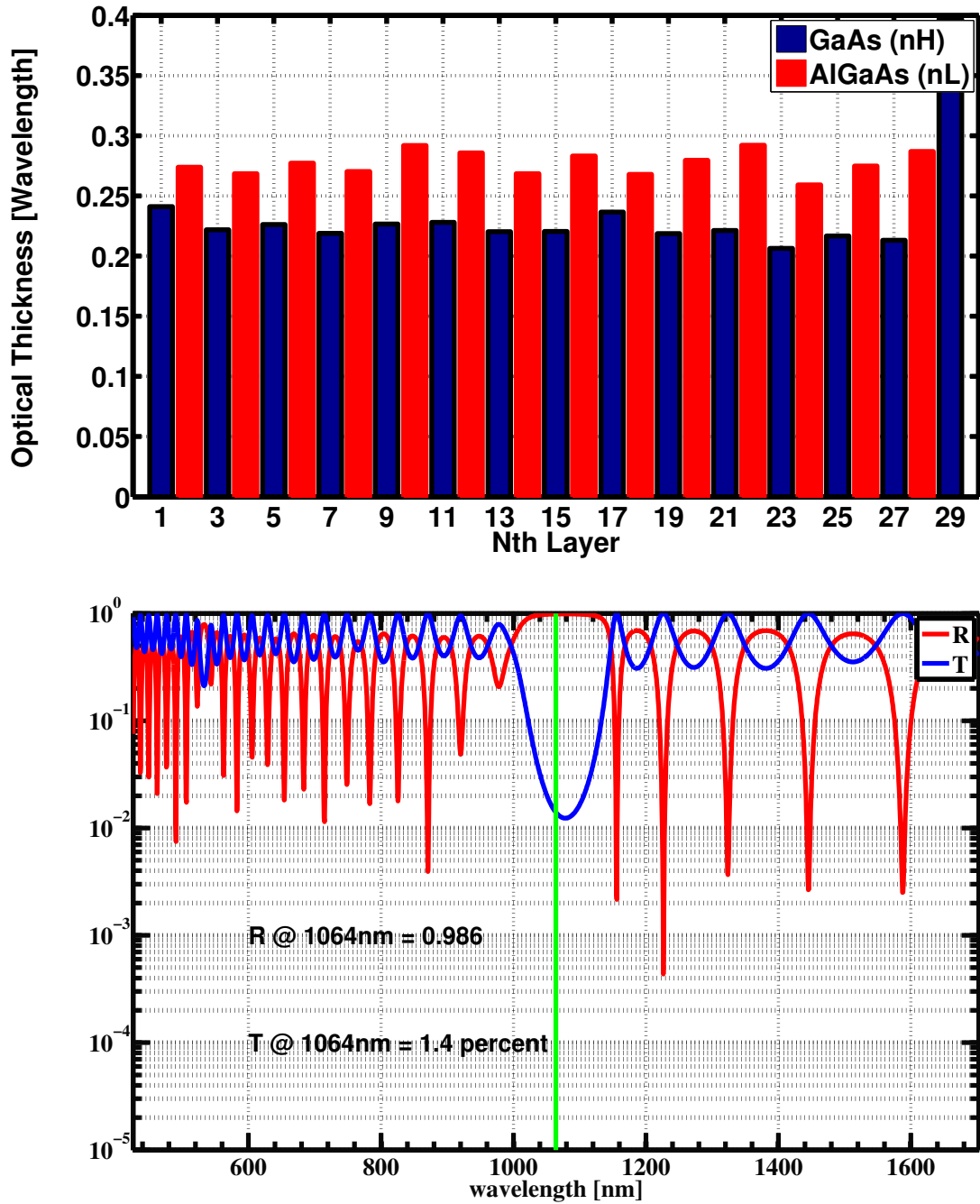


Figure 5.14

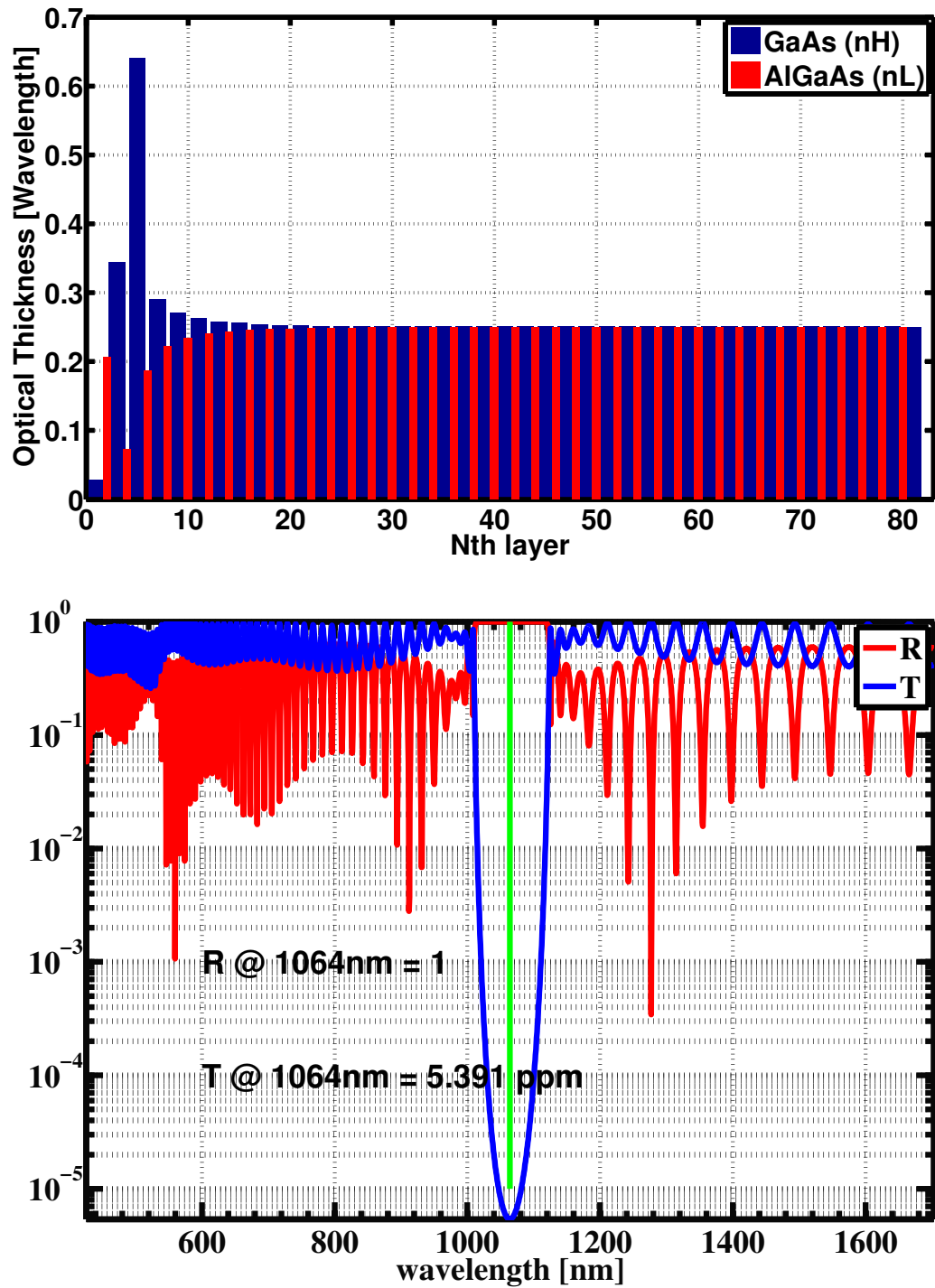


Figure 5.15

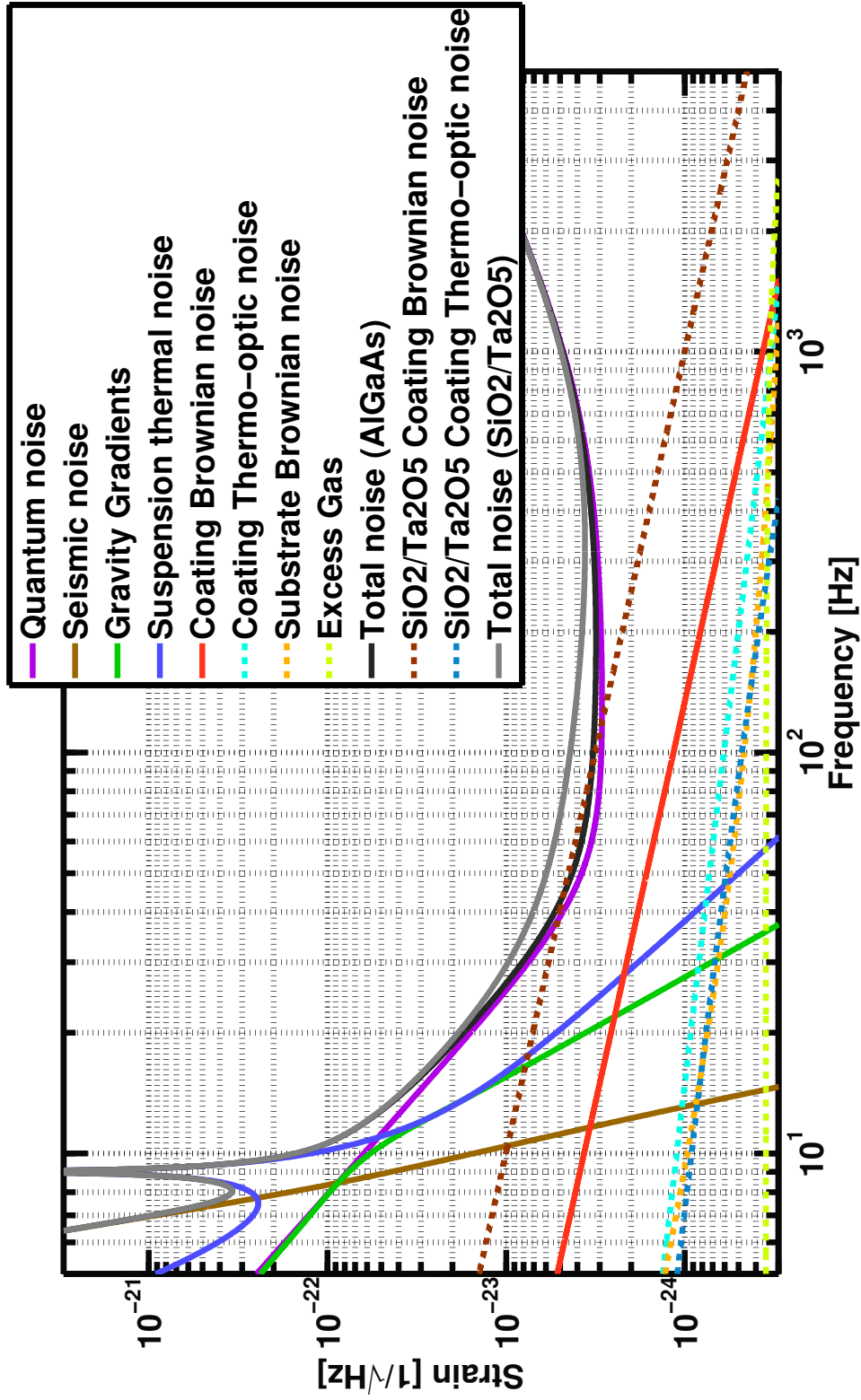


Figure 5.16: The estimated noise budget of Advanced LIGO with TO optimized AlGaAs coatings. The confidence plot as shown in Fig. 1.4 is removed to display the noise level more clearly. Coating Brownian noise level of SiO_2/Ta_2O_5 coatings and the corresponding total noise are plotted in dashed brown and grey, respectively. Coating Brownian noise level of AlGaAs coatings and the corresponding total noise are plotted in red and black, respectively.

Chapter 6

Future Upgrade and Application

In this chapter, we will discuss about some possible upgrades for the experiment and its application as a frequency stabilized light source.

6.1 Future Upgrade

The main goal for the upgrade is to expand the measurement bandwidth. As Mechanical losses in bulk SiO_2 and in thin film SiO_2/Ta_2O_5 from ring down measurements exhibit frequency dependent behavior [100, 101]. But the frequency dependent component is much smaller than the constant loss (for example, $\phi_{SiO_2} = 0.4 \times 10^{-4} + f(2.7) \times 10^{-9}$ [100]) and it is hard to be able to observe this subtle change in a narrow frequency band. With a wider measurement band, we might be able to study more about how the frequency dependent loss affects the noise level. To do this, we have to minimize the relevant technical noise sources as discussed in chapter 4. The measurement from Fig. 3.9 shows that from DC to around 10 Hz, the current sensitivity is limited by photothermal noise, while, from 1 kHz and above, the sensitivity is limited by shot noise, PLL readout noise and residual frequency noise. Plans to improve the sensitivity in each regimes are discussed in the following sections.

6.1.1 Improvement in Sensitivity at Low Frequency

To improve the sensitivity at low frequency, we have to

- **Upgrade ISS:** A better intensity stabilization servo with higher gain and output is required to suppress more intensity noise. The current servo gain uses an SR560 low noise preamplifier with the output of 10 Vpp¹. This output range limits the dynamic range of the current ISS to about $\pm 5\%$.
- **Improve long term beat measurement:** To measure the beat note at low frequency, the PLL has to be locked for a long time. Usually, PLL is out of lock because the beat

¹<http://www.thinksrs.com/downloads/PDFs/Catalog/SR560c.pdf>

frequency drifts beyond the tuning range. Currently, the drifts around sub Hz level are from photothermal noise, which is driven by not only the laser intensity noise, but also the beam position fluctuations. Temperature variations during the day, can cause the optic mounts, and the table to warp from their original positions, resulting in the mismatch beam-cavity position. The power drop due to this effect can be larger than 30 % which is more than the range of the current ISS can compensate. A better controlled air conditioning in the lab should be able to resolve the issue, because the time constant of the setup can be in the order of a few hours.

- **Minimize scattered light** Since noise from scattered light adds random phase noise to the signal, its effect usually shows up as a bump in the low frequency region. For this setup, two places that are most likely to create scattered light are the vacuum window, and the beat PD. The current 10 inch vacuum window is not high quality optics. The anti-reflective coating is poor and there are several scratches. Thus, using a high quality optic should reduce the scattered light. Instead of using a big window, we can install two 1 inch windows on a modified blind flange, see Fig. 6.1, for the two beams entering the chamber. Not only the cost for the window can be reduce, the windows can be easily replaced with commercially available optics. However, the design should be review, as the usage of o-rings on small windows may compromise the vacuum pressure.

The second place causing scattered light is the beat PD. The current PD is Newport 1811 (125 MHz bandwidth). Because of its high response time, the detector diameter has to be small (100 microns²). For this tiny PD diameter, we may not be able to precisely focusing the beam down to 30 microns³ and directing it to the PD without scattering off the nearby casing. As a result, a photodiode with larger detector is preferred, for example, Newport 2053-FC with 0.9 mm diameter (10 MHz bandwidth). This means that the beat frequency has to be below 10 MHz. Temperature stabilization for the two cavities has to be improved in order to keep the two cavities at the right temperature. One possible way is to use the PLL control signal as a feedback signal for controlling. With this feedback signal, we can avoid adding two temperature sensors in the vacuum chamber and have enough pins on the feedthrough for the heaters.

- **Redesign Seismic Isolation System:** The current double stage seismic isolation that holds the cavities inside the vacuum chamber have resonant frequencies around 10 Hz. This resonant frequency is the highest compared to other resonant frequencies from the seismic isolation stages (air springs and pneumatic table legs). As discussed above, seismic motion introduces not only displacement noise due to the bending of the cavities, but also scattered lights.

²<http://search.newport.com/?x2=sku&q2=1811-FC>

³The beam's diameter has to be smaller than the PD's diameter to prevent any scattered light and noise from beam pointing fluctuations. A factor of 3 is generally acceptable for a Gaussian beam profile.

Unless we can decrease the resonant frequency of the seismic stack, the measurement will be contaminated by scattered light around this frequency. One possible way is to use a suspended platform to hold the cavity mount. This might push the resonant frequency down to a few Hz level.

6.1.2 Improvement in Sensitivity at High Frequency

At high frequency, the limiting noise sources are PLL readout noise, shot noise, and residual frequency noise.

- **Different Readout Technique:** Two main sources that introduce noise in PLL are the VCO's frequency noise and the electronic noise from the photodiode (PD). VCO's frequency noise can be reduced by using another VCO with lower intrinsic noise or using different readout technique. Homodyne detection (delay line technique)⁴ can be used to observe the frequency noise in the signal. An analog circuit for the homodyne detection can be simple. It includes a power splitter, cables with different lengths, a mixer, and a low pass filter. However, this makes the measurement rather sensitive to intensity noise. Sophisticated electronic equipment has been designed to overcome the problem, for example, see LISA phase meter that is used as a readout tool in another thermal noise experiment [149].

Another way is to remove the VCO is to measure the beat off-line. The beat signal can be demodulated using a low noise reference (e.g., Rb clock) to reduce the beat frequency below the bandwidth of DAQ. The recorded data can be used to extract the frequency noise of the beat without any frequency noise introduced by the VCO.

However, electronic noise from the PD will still be a problem. Although electronic noise is usually flat, the noise that shows up in the frequency measurement is proportion to temporal frequency. This effect is very undesirable for measuring the signal at high frequency. It is unavoidable no matter what readout techniques we use. Although the SNR can be improved by increasing the input power, the saturation level of the PD will limit the maximum input power.

- **FSS with higher UGF** In order to measure coating noise at high frequency, the unity gain frequency (UGF) of the servo has to be increased more. Sideband frequency is one of the factors that determine the UGF of the servo. The error signal from PDH locking can contain a term that varies at the same frequency as the sideband. To make sure that it will not be fed back to the laser, the maximum UGF has to be roughly a factor of 10 smaller than the sideband frequency. For instance, the maximum UGF of the FSS servo with the sideband frequency

⁴For a review on homodyne detection, see Ref. [121].

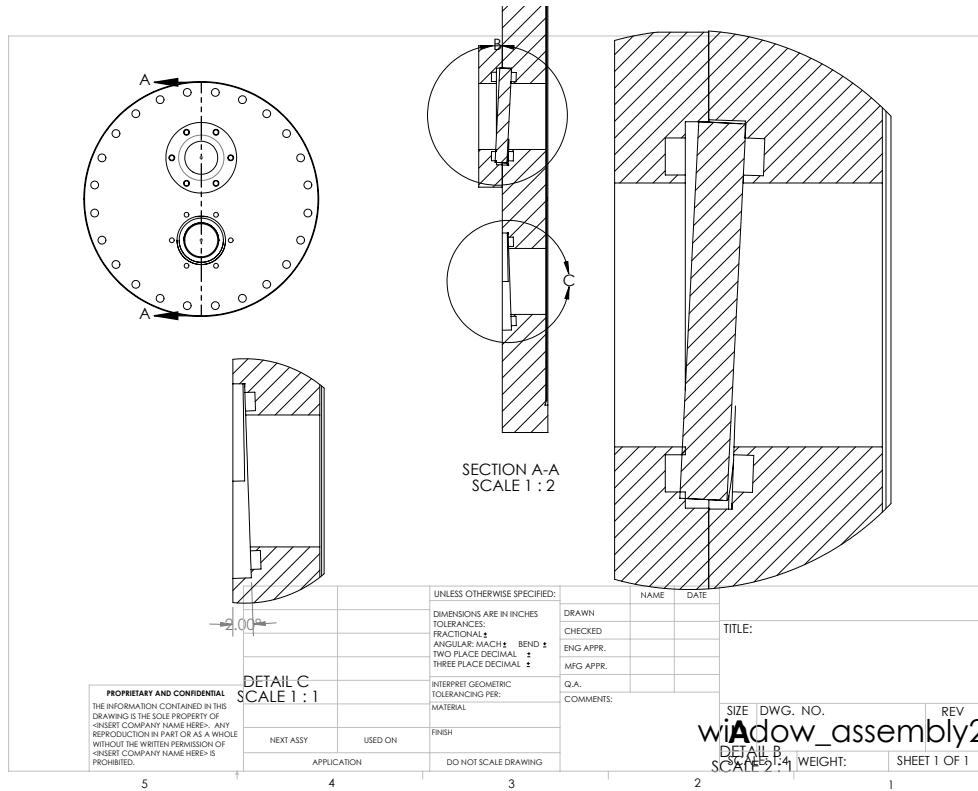
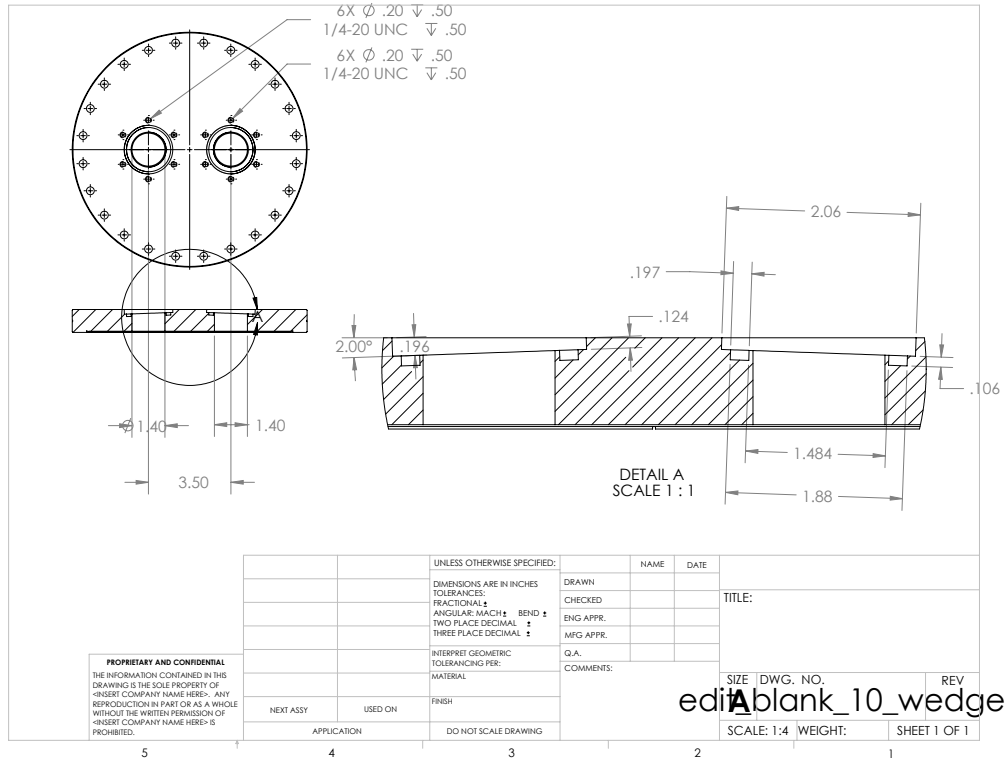


Figure 6.1: Drawings of new vacuum window. Two smaller windows (1 inch diameter, AR coated) are installed on the blank. Both windows will be tilted to reduce back reflection from the window surfaces. The grooves on the windows will be filled by O-rings.

at 14.75 MHz might be only around 1 MHz. By selecting a higher sideband frequency, for example at 35.5 MHz, we can increase the measurement band by roughly a factor of 2.

6.2 Application: Frequency Stabilized Light Source

A frequency stabilized light is useful as a stable reference. It can be used for diagnosing noise in a system using interferometric technique. The setup of this work stabilizes laser frequency to the reference cavity's thermal noise limit and uses only small beam power for the measurement. Thus, the byproduct of this experiment is a frequency stabilized laser source. Although the short cavity is designed for coating thermal noise measurement⁵, the laser frequency noise is still much better than the NPRO's free running noise. This frequency stabilized light can be provided as a reference signal for other experiments. The light can be picked off from the setup and distributed to nearby labs via optical fiber. Here is a brief discussion on a few experiments at Caltech LIGO labs that can benefit from having a stable light source.

6.2.1 Laser Gyroscope

Motions on the ground due to shaking and tilting are indistinguishable for a conventional mass-spring seismometer. If the conventional seismometer is used as a sensor in a feed forward system (e.g., LIGO suspension system), tilt motions, interpreted as seismic motions by the seismometer, will introduce extra noise to the system. To resolve the issue, tilt meters were developed to monitor only tilt motion. One example of a tilt sensor is a laser gyroscope (GYRO) which is an interferometer using Sagnac effect. The setup consists of a single laser, and a ring cavity. The beam from the laser is split into two beams, each enters the cavity in opposite directions. If the ring rotates, the frequencies of the two beam will be shifted due to the Sagnac effect. The frequency differences between the two beam is given by [150]

$$\Delta\nu = \frac{4}{\lambda S} \vec{A} \cdot \vec{\omega}, \quad (6.1)$$

where S is the cavity perimeter, \vec{A} is the cavity area vector, and $\vec{\omega}$ is the angular velocity of the earth rotation. As the surface of the ground tilts, \vec{A} rotates and causes the frequency shift which can be monitored as a tilt sensor.

The setup for GYRO [151] is conceptually similar to the prototype setup discussed in this work. The main beam is locked to the ring cavity via PDH lock, the second beam is frequency shifted and locked to the cavity by an AOM. The frequencies of the two beams are one free spectral range apart (100 MHz).

⁵The frequency noise of the laser will be less if it is locked to a longer one, cf. Eq. 3.3

Similar to other reference cavities, the ring cavity is subject to displacement noise, for example, mirror vibrations. Although the noise is common between the two beams and should not affect the read out, the frequency shifts (due to the displacement noise) from different axial modes are not the same. The frequencies of the two beams are $\nu_1 = n \frac{c}{2S}$ and $\nu_2 = (n + 1) \frac{c}{2S}$. The frequency noise due to the displacement noise δS for each beam is

$$\frac{\delta\nu_1}{\nu_1} = \frac{\delta\nu_2}{\nu_2} = \frac{\delta S}{S}, \quad (6.2)$$

so

$$\delta\nu_{fake} = \delta\nu_2 - \delta\nu_1 = \frac{\delta S}{2S^2} c. \quad (6.3)$$

This creates a fake GYRO signal $\delta\nu_{fake}$. If the laser for GYRO is compared to another stable reference signal. The signal due to the cavity displacement noise can be observed and subtracted of the GYRO signal to achieve better sensitivity.

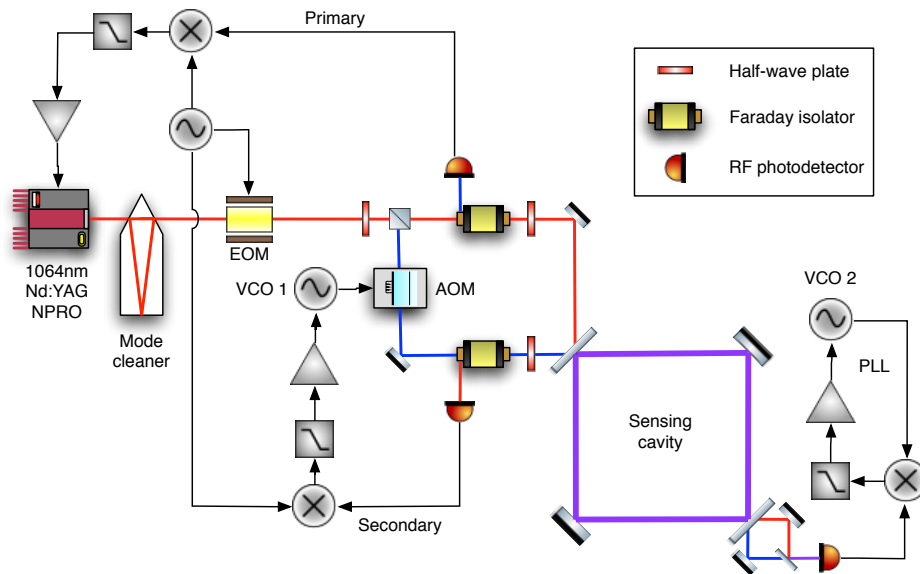


Figure 6.2: A schematic diagram of GYRO setup. Picture credit: William Z. Korth.

6.2.2 Crackle

Maraging blades that are used for suspending LIGO test masses may be susceptible to crackle noise, which originates from dislocations in the blades. The noise can be up-converted into the audio frequency band due to sub-Hz driving motions. To study the phenomenon, a Michelson interferometer with both end mirrors attached to the device under test (the blades) can be used. Each arm is driven simultaneously at low frequency. The output can be observed for any incoherent crackle noise between the two arms. The frequency noise of the light source masks the output of the

the grating, the angle of the grating with respect to the incident beam) [154]. A stabilized frequency light source can be very useful during the setup configuration of the ECDL. By beating the ECDL output with the reference light and extracting the signal with PLL or delay-line technique, the ECDL wavelength can be tuned to the desired value, and its frequency noise can be optimized for better performance.

Appendix A

Comparison with Other Experiments

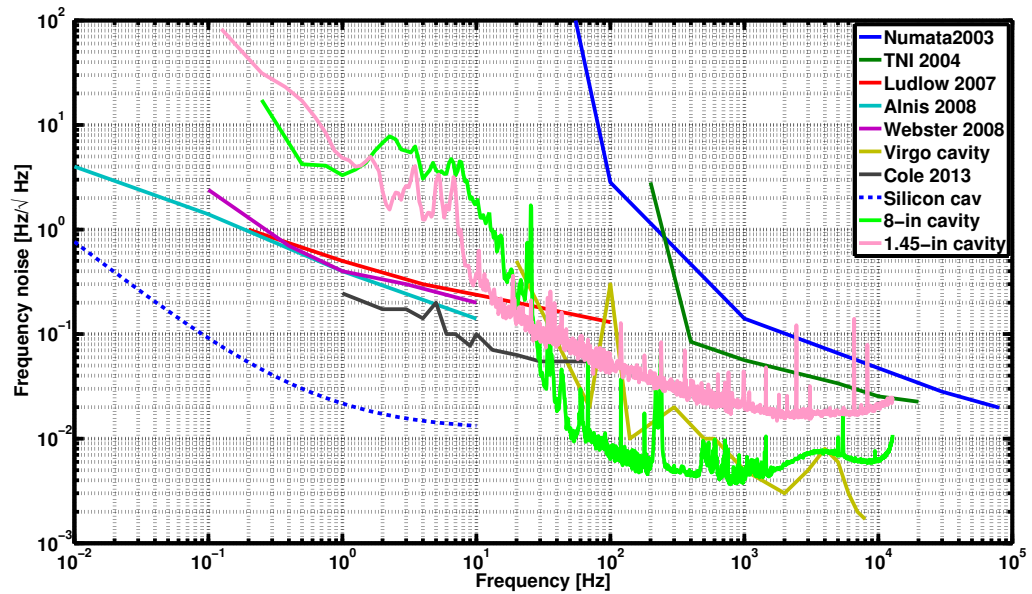


Figure A.1: Results from several experiments shown in frequency noise.

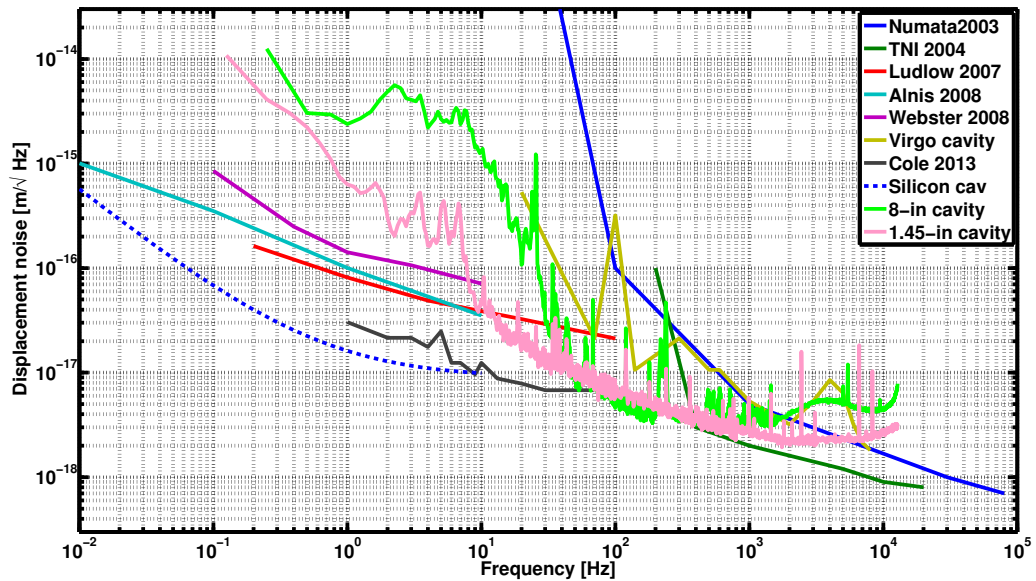


Figure A.2: Results from several experiments shown in displacement noise.

trace	cavity length	λ [nm]	Ref.
Numata 2003	1 cm	1064	[54]
TNI 2004	1 cm	1064	[55]
Ludlow 2007	7 cm	698	[56]
Alnis 2008	7.75 cm	972	[57]
Webster 2008	10 cm	1064	[58]
Virgo cavity	30 cm	1064	[155]
Cole 2013	3.5 cm	1064	[143]
Silicon cavity	21 cm	1550	[156]

Table A.1: Note about each trace on the plots above.

- **Numata and TNI:** These two experiments were designed to measure coating thermal noise measurement. The noise plot shows the differential noise between the two cavities.
- **Ludlow 2007:** The cavity was supported vertically. The substrates and spacer were made of ULE. The seismic strain coupling is around $5 \times 10^{-11} [1/ms^{-2}]$
- **Alnis 2008:** Beat between two ECDLs independently stabilized to two FP cavities. The cavities were supported vertically. The mirror substrates and spacer were made from ULE, with SiO_2/Ta_2O_5 coatings.

- **Webster2008:** Two identical cavities were operated around 10 C for zero thermal expansion coefficient. The spacers were machined and held horizontally for vibration insensitivity. ULE spacer and substrates. The strain due to seismic isolation is $3 \times 10^{-12}[1/ms^{-2}]$
- **Virgo cavity:** A reference cavity for pre-stabilizing the main laser frequency used for VIRGO detector. The substrates and spacer were made of ULE.
- **Cole 2013:** The cavity were formed by AlGaAs coatings with fused silica substrate and Zerodur spacer at room temperature. The laser frequency locked to the cavity was measured by beating (via frequency comb) with another laser frequency locked by JILA ultrastable cavity.
- **Silicon cavity:** The cavity noise was measured at 124 K. The cavity spacer and the mirror substrates were constructed from single crystal silicon. The coatings were SiO_2/Ta_2O_5 The cavity was supported vertically. The measurement was reported in modified Allan variance. The equivalent result in frequency noise shown in the plot was done by David Yeaton-Massey. The estimated strain $\Delta L/L$ is less than $10^{-11} [1/ms^{-2}]$.

Often, other similar experiments report their results in time domain using the Allan variance $\sigma_y^2(\tau)$, or the modified Allan variance $\text{Mod } \sigma_y^2(\tau)$ (the square root of these values are called Allan deviation and Mod Allan deviation). The modified Allan variance is used to improve the estimate frequency stability of the source when the dominant noise type in the short term is flicker phase modulation ($S_\nu \propto f$) of white phase modulation ($S_\nu \propto f^2$). The relation between the two is given by [157]

$$\text{Mod } \sigma_y^2(\tau) = \frac{2}{n^4(\pi\nu_0\tau_0)^2} \int_0^{f_h} \frac{\nu_0^2 S_\nu(f) \sin^6(\pi\tau f)}{f^2 \sin^2(\pi\tau_0 f)} df, \quad (\text{A.1})$$

where f_h is the cutoff frequency of the measured S_ν , $\tau = n\tau_0$ where n is the number of samples averaged, and ν_0 is the carrier frequency. In general, each frequency noise spectrum with different dependent on f results in $\text{Mod } \sigma_y^2(\tau)$ with different dependent on τ . The table for converting the modified Allan variance to power spectrum of frequency noise is taken from Ref. [157].

Noise Type	$S_\nu(f)$	$\text{Mod } \sigma_f^2(f)$
Random walk frequency	$\nu_0^2 h_{-2} f^{-2}$	$5.42 h_{-2} \tau$
Flicker frequency	$\nu_0^2 h_{-1} f^{-1}$	$0.936 h_{-1}$
White frequency	$\nu_0^2 h_0 f^0$	$h_0/4\tau$
Flicker Phase	$\nu_0^2 h_1 f^1$	$\frac{3.37}{4\pi^2} h_1 \frac{1}{\tau}$

Table A.2: Conversion Factors for $S_\nu(f)$ and $\text{Mod } \sigma_f^2(f)$. ν_0 is the carrier frequency.

For example, if the measured Mod $\sigma_y^2(\tau)$ can be written as

$$\sigma_y^2(\tau) = \frac{C_1}{\tau} + C_2 + C_3\tau, \quad (\text{A.2})$$

where C_1 , C_2 , and C_3 are constants. The corresponding power spectrum of frequency noise, using the conversion factor in the above table, will be

$$S_\nu(f) = \frac{\nu_0^2}{4C_1} + \frac{\nu_0^2 C_2}{0.936f} + \frac{\nu_0^2 C_3}{5.42f^2}. \quad (\text{A.3})$$

The frequency bandwidth where this conversion is valid will depend on the sampling time and τ_{max} of the measurement and any cut off frequencies of the low pass filters used in the measurement.

Appendix B

Frequency Stabilization Servo

- TTFSS setup:** Schematic of the table top frequency stabilization servo (TTFSS) used in this work can be found in LIGO document control center ¹. The implementation of TTFSS on the setup with relevant calibrations is shown in Fig. B.1 below. The servo controls the laser frequency via two actuators, the PZT on the NPRO crystal, and the EOM. The error signal goes through a common path, then separated to two. The *PC path* sends the control signal to the EOM. The *Fast path* sends the control signal to the NPRO. We pick off the *Fast* signal, low pass it, and use it as an error signal for temperature control on the laser crystal (not shown in the diagram) for long term lock.
- Performance of TTFSS:** To characterize the servo performance, we measure the open loop gain transfer function (OLG) and compared it with the calculated OLG from the schematic. The calculation can be done by computing the transfer function of each stage and multiply them together. For *Fast path* only simple low pass stages are used and they are easy to calculate. For *PC path*, the schematic becomes more complex. One way to find the transfer function is by using LISO to simulate the shape of the transfer function, then use a fit function to determine all poles and zeroes in the servo. For example for the second stage of PC path in diagram we include the capacitance of the EOM, about 20 pF, as given in the manual. The transfer function result is shown in Fig. B.2. Finally, the calculated results from the two paths are combined to get the whole OLG. Then it is compared to the measurement. They agree well and meet the requirements for reference cavities used in this work. See Fig. B.3. The requirement is calculated by setting the residual frequency to be 0.3 of the expected signal, then calculate what would be the necessary gain to push the noise down to that level. From , Eq. 3.4 one gets,

$$\text{required OLG} \approx \frac{\text{free running noise}}{\text{residual noise}} \quad (\text{B.1})$$

¹The schematic is on <https://dcc.ligo.org/LIGO-D040105>. See the test plan on <https://dcc.ligo.org/LIGO-E1000609>

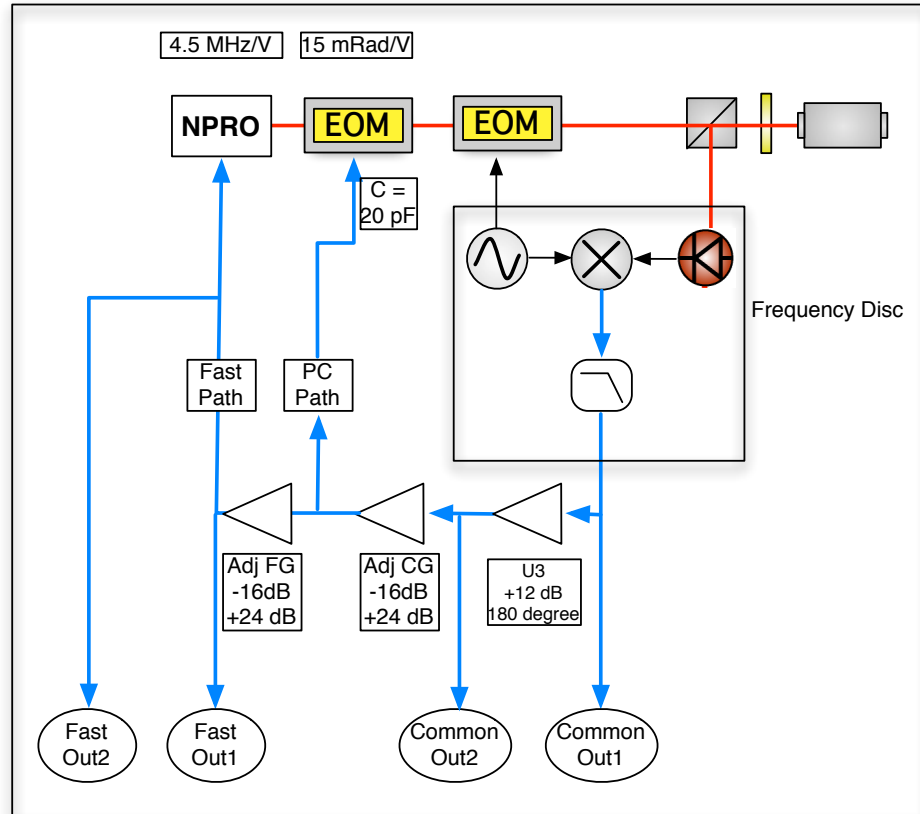


Figure B.1: A schematic explaining how TTFSS is implemented in the setup. The servo has two actuators, one is the PZT on the NPR0 that changes the refractive index via elastic called Fast Path. The PZT has flat response from DC up to around 1 kHz, with gain around 4.5 MHz/V. Another actuator is the Electro-Optic modulator which changes the phase of the output beam called Pockell cell path (PC). The gain is 15 mRad/V or 15 MHz/V $[\frac{f}{1\text{Hz}}]$. Two adjustable gains are for common path (CG) and for Fast path (FG). The gains are adjustable between -16 dB and +24 dB. The common gain adjusts the overall magnitude of the servo, while the fast gain alters the shape of the servo. There is a flip sign switch on the fast path to match the phase between the two paths. The frequency discriminator, D_v , in the setup is around 5.5 V/MHz. This can be measured from the slope of the error signal during the cavity scan.

The requirement for a longer cavity is higher because of the smaller signal. It requires higher servo gain to suppress the free running noise down to the cavity's displacement noise.

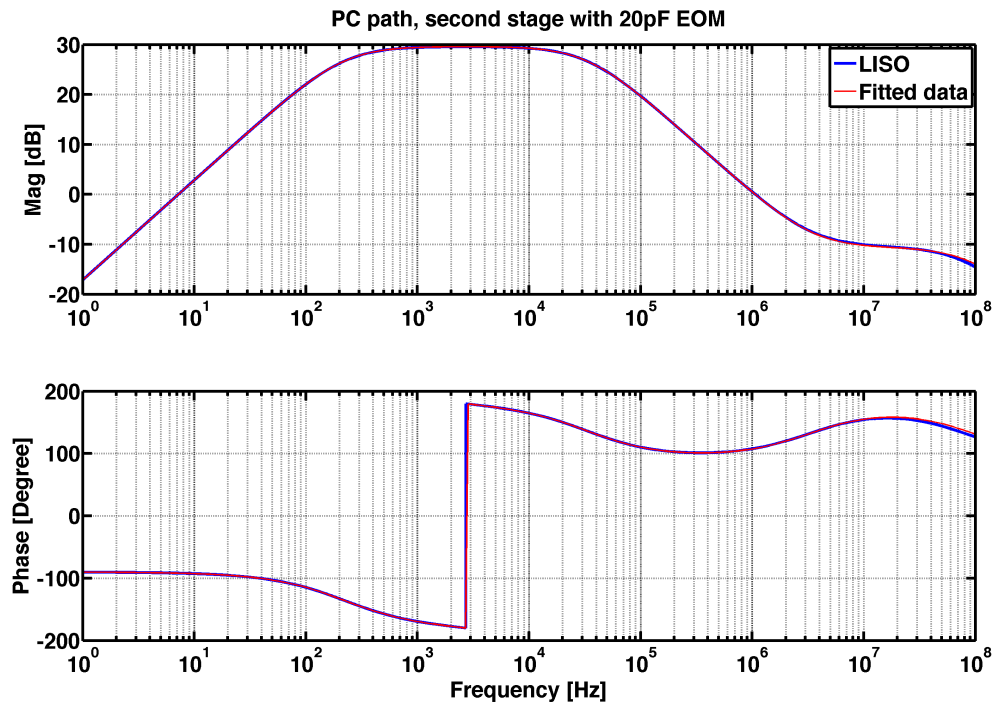


Figure B.2: Transfer function of *PC path* as obtained from LISO model, the blue plot is the result from the simulation. The red plot is the calculation from poles and zeros obtained from the fit.

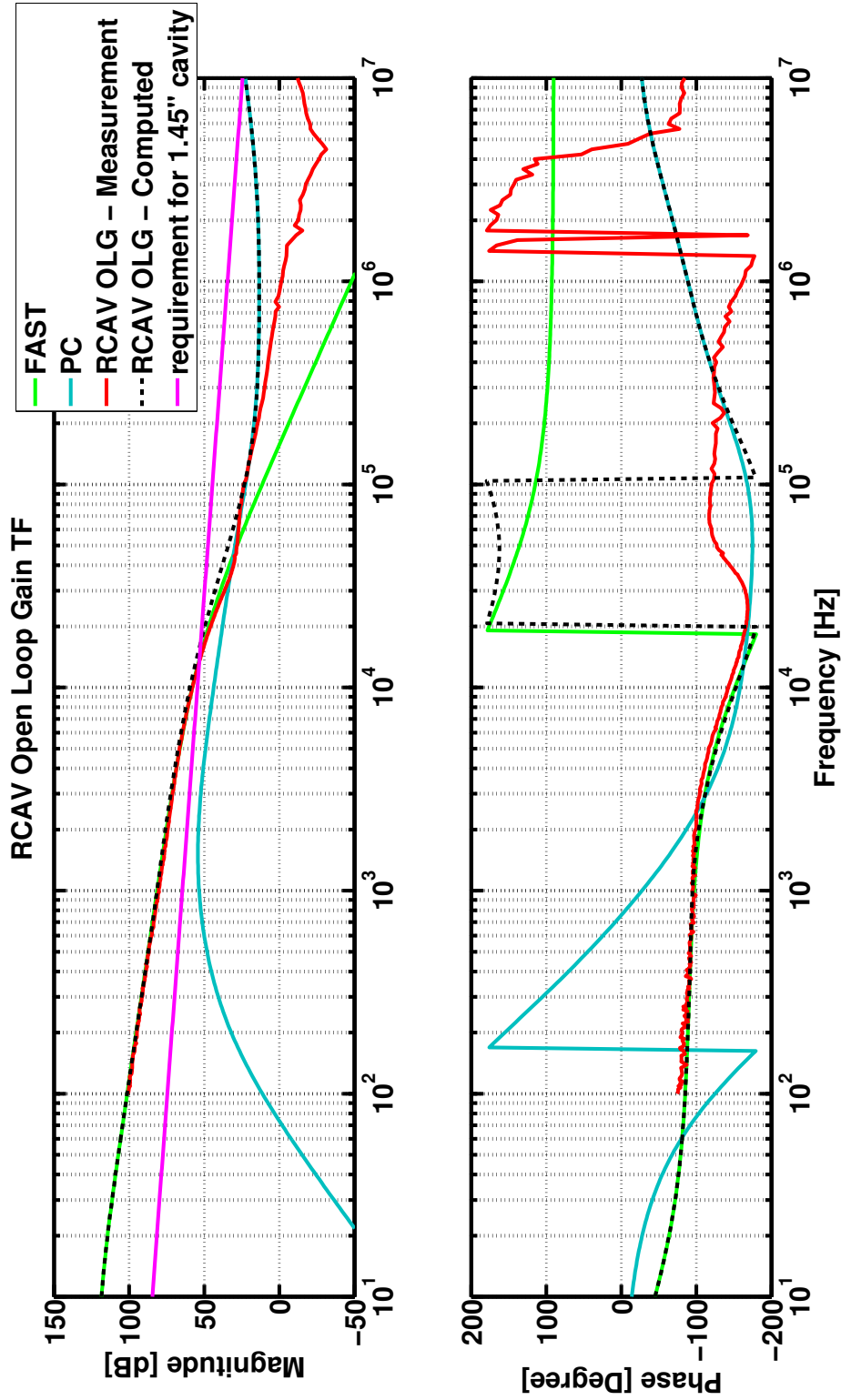


Figure B.3: Open Loop Gain transfer function of TTFSS, 1mW input power. The requirements assume that the residual noise is within 5 percent of the suppressed frequency noise. The boost, which is an integrator stage with a zero at 4.6 kHz is turned off during the measurement. From the plot, the servo is good enough up to 1 kHz for the setup with 1.45 inch cavities. The inconsistency between the measurement and the calculated TF might come from the PC path. We could not measure the TF of this path individually due to the limited accessibility of the test points. The calculated TF might be different from the real situation due to incorrect model and non-ideal behavior of the op amps. Also, the TF of the RFPD for PDH lock is not taken into account. This will result in the deviation of the measured phase at frequency around 10 MHz an above due to the resonant circuit in the RFPD.

Appendix C

Material parameters for SiO₂/Ta₂O₅ and AlGaAs

C.1 Table of Parameters

Parameters	SiO ₂	Ta ₂ O ₅	GaAs	Al _{0.92} Ga _{0.08} As	Al _{1-x} Ga _x As
Heat capacity, C ($\times 10^6$) [J/Km^3]	1.64	2.1	1.76	1.69	$1.76 + 0.114x - 0.19x^2$
Thermal conductivity, κ [W/mK]	1.38	33	55	70	$55 - 212x + 248x^2$
Young's modulus, Y [GPa]	72	140	100	100	-
Poisson's ratio, σ	0.17	0.23	0.32	0.32	-
Thermal expansion, α ($\times 10^{-6}$) [$1/K$]	0.51	3.6	5.7	5.2	$5.73 - 0.53x$
Thermorefractive, β ($\times 10^{-6}$) [$1/K$]	8	14	366	179	$366 - 203x$
Refractive index, n @1064nm	1.45	2.06	3.48	2.98	$3.48 - 0.578x$
Mechanical loss angle, ϕ ($\times 10^{-4}$)	1	4	0.25	0.25	0.25

Table C.1: Material parameters used in this work.

C.2 Uncertainties in Parameters

Errors in the material parameters will cause error in thermal noise calculation. For a high reflective dielectric mirror where Brownian thermal noise in coating dominates, uncertainties in loss angles will be the most significant parameters to determine the noise level accurately. Loss angles are usually obtained from a ring down measurements. The coating is applied on a blade or a disc with low loss. The system is excited and the ring down is measured. The coating loss and the whole system loss is related as

$$U_{tot}\phi_{tot} \approx U_s\phi_s + U_c\phi_c, \quad (C.1)$$

where U is the elastic energy in each ring down mode. Note that if ϕ_{bulk} and ϕ_{shear} are different, Eq. C.1 has to be separated in bulk and shear modes accordingly. The dilution factor U_s/U_c can be calculated analytically, or by FEA. For example, the energy loss from a disc with a thin coating can be written as:

$$\phi_{tot} = \phi_s + \frac{U_c}{U_s} \phi_c. \quad (\text{C.2})$$

ϕ_s is the loss of the substrate that can be measured before applying the coating, ϕ_{tot} is the total loss of the coating-substrate system. For each mode, the dilution factor will be different. For the first drumhead mode the dilution factor is given by [158]

$$\frac{U_c}{U_s} = 3 \frac{Y_c d}{Y_s t}, \quad (\text{C.3})$$

where d is the coating thickness, and t is the substrate thickness, Y_c is the averaged Young's modulus of the coating. For a wafer structure of the coating, the bending mode is mostly stretching and compressing along the surface layer. Y_c can be calculated as

$$Y_c = \frac{Y_1 d_1 + Y_2 d_2}{d_1 + d_2}, \quad (\text{C.4})$$

where d_1 and d_2 are the total thickness of material 1 and 2. This calculation is similar to a system of connected springs. The dilution factor obtained from this analytical result agrees with the calculation from FEA (as reported in Ref. [99]) within 5%. Hence, uncertainties in Young's moduli lead to uncertainty in the dilution factor which is used for extracting the coating loss angle from ring down measurements. These errors in Young's moduli propagate through the extraction of ϕ (Eq. C.2) and show up in the errors of the loss angle. The result can be much larger than the error in the coating calculation due to uncertainties in Young's moduli alone (as done in Ref. [53]).

Development in nano-indentation technique allows us to measure Young's modulus in thin film form with better accuracy although the samples used are still much thicker, from 500nm to a few microns, than a single layer of the dielectric coating (around 200 nm or less). Young's moduli of SiO₂ and Ta₂O₅ are measured to be 70 GPa and 140 GPa respectively [159].

C.3 Note for AlGaAs

The elastic parameters of AlGaAs are taken from Ref. [160, 148]. However, due to the crystalline structure of AlGaAs, these parameters are directional dependent. The values here are only averaged values intended to be used in the amorphous coating calculation as an approximation.

Appendix D

High Reflective Coating Structure and its Average Properties

D.1 Why Half Wave Cap?

For quarter wave layer stack (QWL) SiO₂/Ta₂O₅ coatings, SiO₂ and Ta₂O₅ are materials with low (n_L) and high refractive indices (n_H), respectively. Due to the stronger structure of SiO₂, a cap of SiO₂ as a protective layer is usually on top. However, if the SiO₂ cap is 1/4 thick, the first reflected beam at the air–cap interface layer will destructively interfere with the rest of the reflected beams, causing the reflectivity to go down, see Fig. D.1(A).

If the cap has thickness of 1/2 wave length, the reflected beam from the interface between the cap and all the following layers will be in phase with the first reflected beam at the air–coating surface, see Fig. D.1(B).

For a cap with high index material, it can be 1/4 wave length thickness, and the phase from every reflected beams still interferes constructively, see Fig. D.1(C).

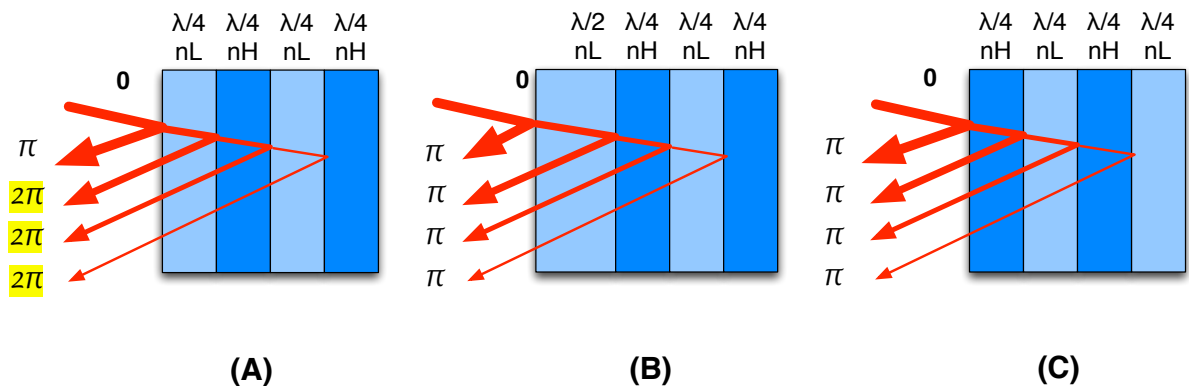


Figure D.1: Reflection phase from a few top layers of different coating structures. (A) QWL with low index material (light blue) on top. (B) QWL with a half wave cap of low index material. (C) QWL with high index material (blue) on top

For Fig. D.1(B) and Fig. D.1(C), the incoming beam and the reflected beam are 180 degrees out of phase. It means that the electric field at the coatings surface will always be zero. This prevents the burning on the surface of the coating. With this, the standing wave in a Fabry–Perot cavity formed by two such mirrors will always have zero electric field at the surfaces.

For AlGaAs coatings, the situation is different from SiO_2/Ta_2O_5 coatings. The cap has to be GaAs (nH) because $Al_{0.92}Ga_{0.08}As$ will oxidize and change its material properties. With the high index cap, the thickness has to be 1/4 wavelength.

If the substrate's refractive index is smaller than both nH and nL, the last layer at coating-substrate interface has to be the high index material to have constructively interfere reflected beam. However, the effect is smaller as the numbers of the layer increase.

D.2 Averaged Material Parameters for Coatings

With the length scales of ω_0 , and r_T are large compared to the layer thickness, we can use averaged material properties to represent the coating. The equations here are taken from Ref. [78, 74]. We include them here for completeness. The thermal expansion coefficient for a given layer k in the coating is

$$\bar{\alpha}_k = \alpha_k \frac{1 + \sigma_s}{1 - \sigma_k} \left[\frac{1 + \sigma_k}{1 + \sigma_s} + (1 - 2\sigma_s) \frac{Y_k}{Y_s} \right] \quad (D.1)$$

and the volume average coefficient for a coating with N layers each of thickness d_k is

$$\bar{\alpha}_c = \sum_{k=1}^N \bar{\alpha}_k \frac{d_k}{d} \quad (D.2)$$

where d is the total coating thickness

$$d = \sum_{k=1}^N d_k \quad (D.3)$$

The heat capacity calculated by volume averaging,

$$C_c = \sum_{k=1}^N C_k \frac{d_k}{d}, \quad (D.4)$$

the average thermal conductivity,

$$\kappa_c = \sum_{k=1}^N \frac{1}{\kappa_k} \frac{d_k}{d}, \quad (D.5)$$

the effective β used here follows the notation in [74] where β is chosen to be positive and the negative sign is written explicitly. An effective TF coefficient, $\bar{\beta}$ is defined such that

$$\frac{\partial Z_{TR}}{\partial T} = -\bar{\beta}\lambda. \quad (D.6)$$

For $\bar{\beta}$ made of 1/4-wave doublets (SiO_2/Ta_2O_5) with a 1/2-wave SiO_2 cap layer (or any coating materials with n_L as a cap), $\bar{\beta}$ can be approximated by

$$\bar{\beta} \simeq \frac{B_H + B_L(2(n_H/n_L)^2 - 1)}{4(n_H^2 - n_L^2)}. \quad (D.7)$$

Where B_X is the fractional change in optical path length with respect to temperature in material X,

$$B_X = \beta_X + \bar{\alpha}'_X n_X, \quad (D.8)$$

where

$$\bar{\alpha}'_X = \alpha_X \frac{1 + \sigma_X}{1 - \sigma_X} \quad (D.9)$$

is the correction for the fractional path length change due to thermal expansion inside a layer [161].

For the cap with arbitrary thickness, $\bar{\beta}$ can be found in Ref. [145]. The numerical calculation for $\bar{\beta}$ is given in Ref. [74] which is used for the TO optimized coating in this thesis.

Appendix E

1.45 Inch Reference Cavity: Design and Assembly

E.1 Choosing Cavity Length

To raise the coating Brownian thermal noise level, we need to decrease the beam size. This can be done by shortening the cavity length while keeping the same mirrors. However, there are other considerations to choose the optimal length of the cavity. Mainly, we have to

- Be able to tune the cavity length by changing the temperature. The shorter the cavity, the higher the temperature required to change the length through thermal expansion, see Fig. E.1.
- Keep the cavity stable.

The condition where the beam can propagate repeatedly without running off from the cavity is given by [124]

$$0 < \left(1 - \frac{L}{R_1}\right) \left(1 - \frac{L}{R_2}\right) = g_1 g_2 < 1, \quad (\text{E.1})$$

Where L is the total length, R_1 and R_2 are the radius of curvature of the mirrors. The value of $g_1 g_2$ vs cavity length is shown in Fig. E.2.

- Make sure no higher order modes will be in resonance simultaneously with the carrier. The allowed resonant frequencies for the cavity is given by Eq. 3.1. However, the incident beam does not consist of only a single frequency, it also has two sidebands. Additionally, the other modes besides TEM00 (from the carrier and the sidebands) can be in resonance with the cavity's other axial modes due to the Gouy's phase shift is [124]

$$\Phi_{mn}(z) = (2m + n + 1) \arctan(\lambda z / \pi w_0^2), \quad (\text{E.2})$$

where m , n are integers denoting the mode number in Hermite–Gaussian modes. The phase velocity increases with higher mode number and leads to differences in the resonant frequencies.

The one-way Gouy's phase shift written as a function of g-parameters is

$$\delta\phi_{mn} = (2m + n + 1)\arccos(\sqrt{g_1g_2}). \quad (\text{E.3})$$

This phase shift is related to the frequency shift as

$$\delta\phi_{mn} = \frac{2\pi\delta f}{c}L = \frac{\pi}{\text{FSR}}\delta f_{mn}. \quad (\text{E.4})$$

If any of these modes are in resonance simultaneously with the carrier, the PDH error signal will be disturbed and becomes unstable. This problem can be avoided by choosing the right cavity length or the right sideband frequency that does not allow other higher order mode frequencies to be close to the cavity's allowed frequencies, see Fig. E.3.

The sensitivity gain due to the shorter cavity is shown in Fig. E.4. With all the considerations discussed above, the length of the cavity is chosen to be 1.45 inch (36.83 mm). The outer diameter and the inner diameter are 1.5 inch (38.1 mm), and 0.375 inch (9.525 mm), respectively, see Fig. E.5. The outer radius is chosen based on how the cavity will be mounted, see section E.4.

E.2 Assembling Reference Cavity with Optical Contact

Optical contact method is used for joining mirrors and a spacer to form a cavity. The jointed objects becomes monolithic through covalent bonds, and the associated noise should be minimum compared to other available bonding techniques. Furthermore, the method is relatively easy and can be done in a lab with a flow bench. Here is an instruction for optical contacting process.

- Clean the flow bench area.
- Prepare isopropanol, methanol and acetone (should be spectrophotometric/reagent grade). The solvents should be stored in glass containers. Use glass syringes with needle metal to dispense the solvents on cleaning wipe. Do not use rubber droppers.
- Clean the target surfaces thoroughly by drag wipe method. For cleaning optical surface in general, wipe the surface with acetone first, follow by methanol. Finally, use isopropanol to finish off any residue. The reason for this solvent order is that acetone is good to remove organic compound, but it dries up quickly and redeposits the contaminants. Thus, methanol is used to dissolve the pre-cleaned surface. Isopropanol can be used to rinse methanol and acetone and to remove any particles on the surface because of its relatively slow evaporation. Make sure not to use excessive amounts of isopropanol. Otherwise it can leave drying marks on the optic. If the stain on the surface still persists, use a pair of forceps to hold a folded

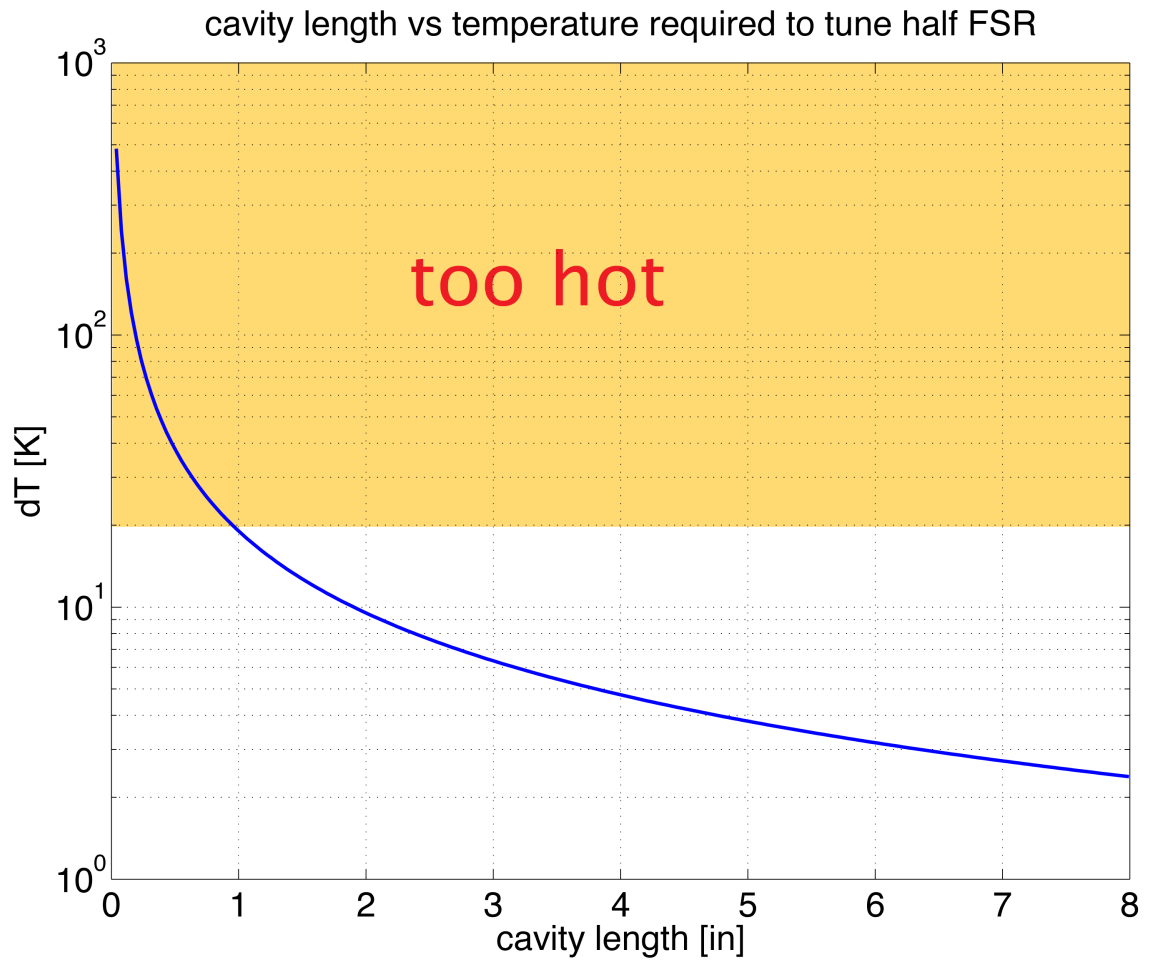


Figure E.1: Changing temperature is required to tune the allowed frequency by one FSR. Generally, shorter cavities require more heating power to change the allowed frequency via thermal expansion. We would like to avoid heating the cavity up more than 20 K (for 1/2 FSR tuning). These conditions set a lower bound for the cavity length to 1 inch. (thermal tuning coefficient for a fused silica $\approx 14 \frac{nm}{K*in}$ ($\alpha = 5.5e-7 \frac{1}{K}$)).

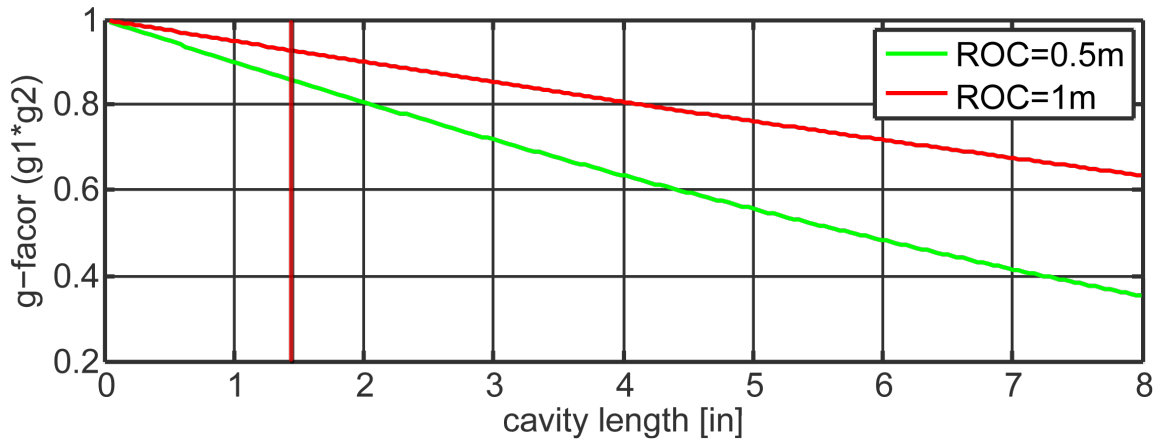


Figure E.2: Cavity g-factor vs cavity length for a 2-mirror FP-cavity with identical mirrors for ROC=0.5m and ROC=1m. There will be no stability issues for the mirrors.

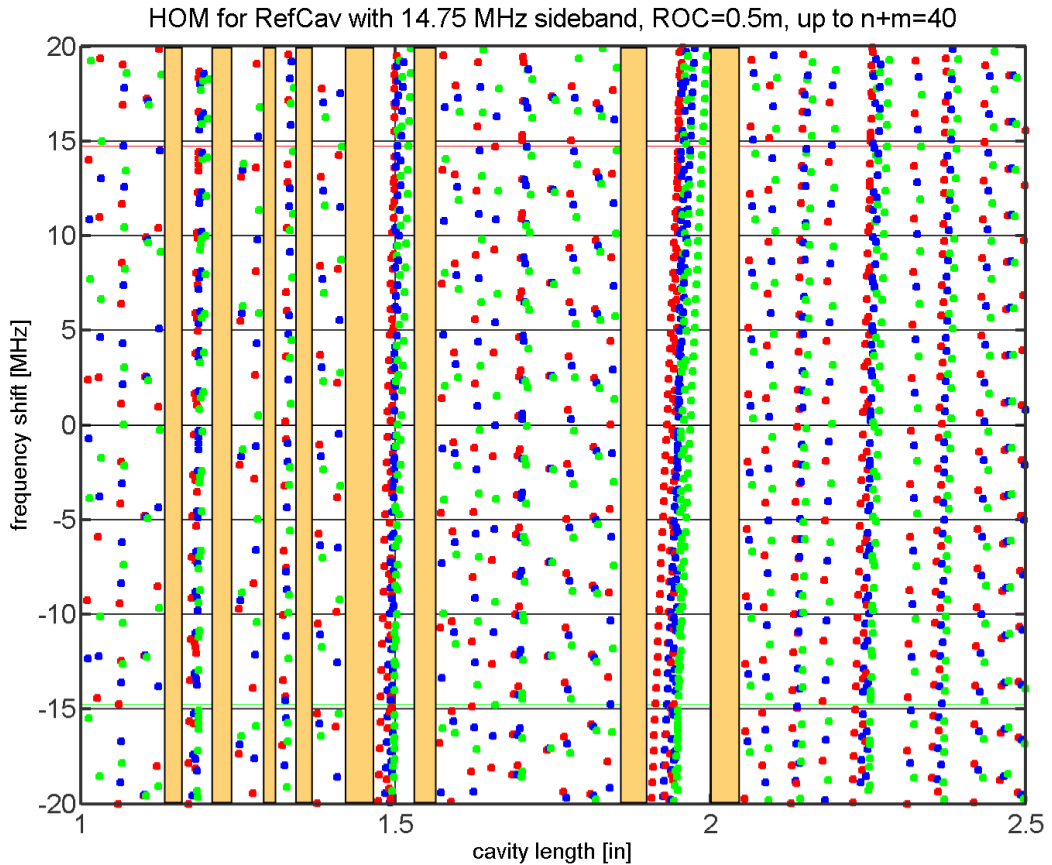


Figure E.3: Higher order modes up to $n+m=40$ for cavities with a length of 1 in to 2.5 in (mirrors ROC=0.5 m). The sideband frequency is 14.75 MHz. Yellow shaded areas are preferred as they are free of higher order modes for any sideband frequency up to 20 MHz. The three widest areas (and so less sensitive to tolerances in spacer fabrication and changes in mirror curvature) are 1.45 ± 0.02 in, 1.88 in and 2.02 in. Legend: red-upper sideband; green-lower sideband; blue-carrier

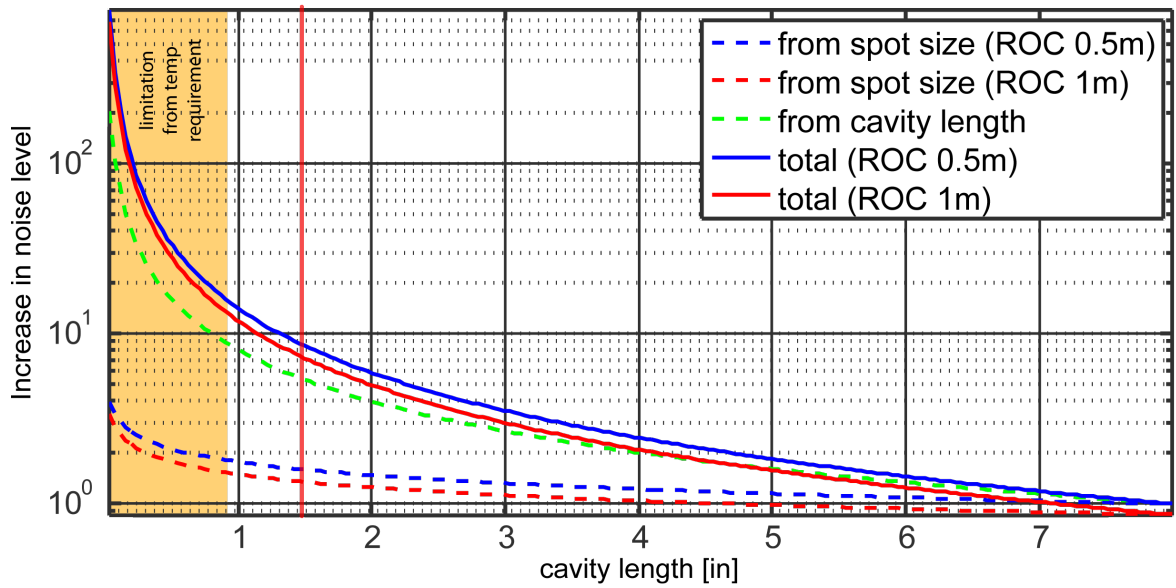


Figure E.4: Coating thermal noise level ratio between the shorter cavity, and the existing LIGO reference cavities (length=8 in, mirrors ROC=0.5 m, concave-concave configuration). The plot shows the results from two different ROC (0.5 m and 1 m) . The lower limit in length is given by the thermal tuning requirement (see Fig. E.1). At 1.45 inches, the total increase in thermal noise is a factor of 8.7

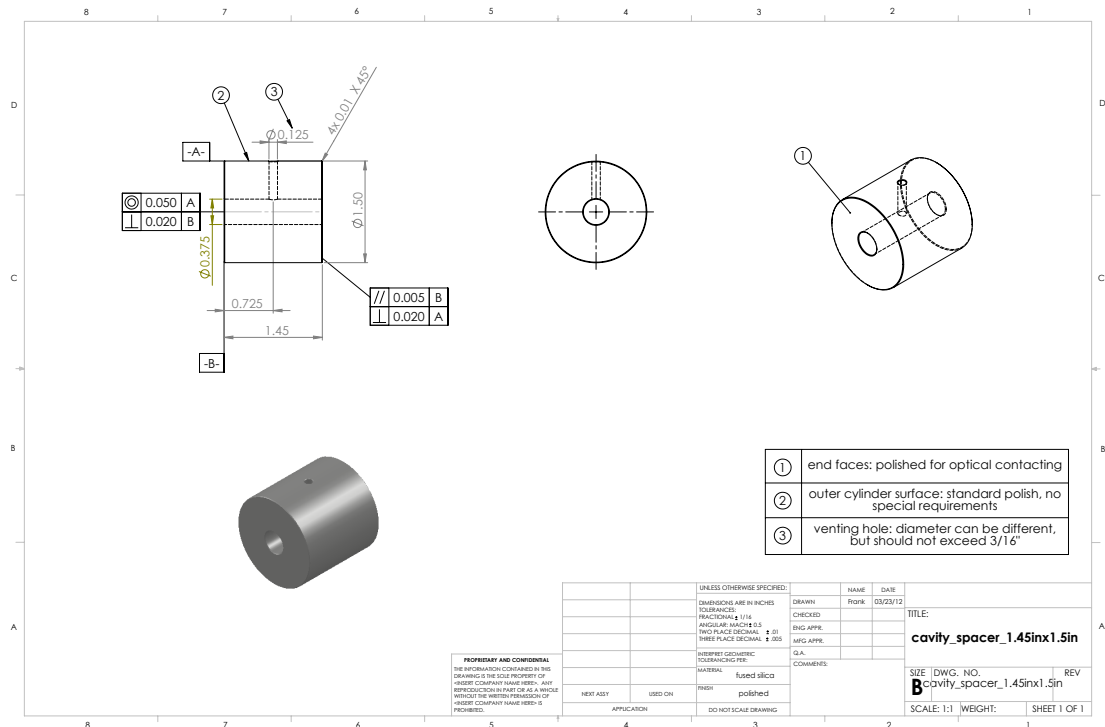


Figure E.5: A drawing of 1.45 inch spacer

cleaning wipe to apply slight pressure while cleaning the surface with the solvents. Then repeat the process with the drag wipe method. For more details on how to clean optics, see Ref. [162, 163, 164].

- Place the two pieces together, for our case, a cavity and a mirror. A temporary fixture to guide the two pieces in contact should be used, as the surface is very slippery. We use a piece of Delrin (Polyoxymethylene plastic) with diameter a few in thousand inch larger than the mirror and the spacer to hold them together coaxially, see Fig. E.6 a.
- Apply slight force to keep the bond going. If the two surfaces are sufficiently clean and smooth, the bond should be formed instantly. If there is a dust particle on the surface, fringes on the bonding area will appear, see Fig. E.6 b. Remove the parts and clean the surfaces again.

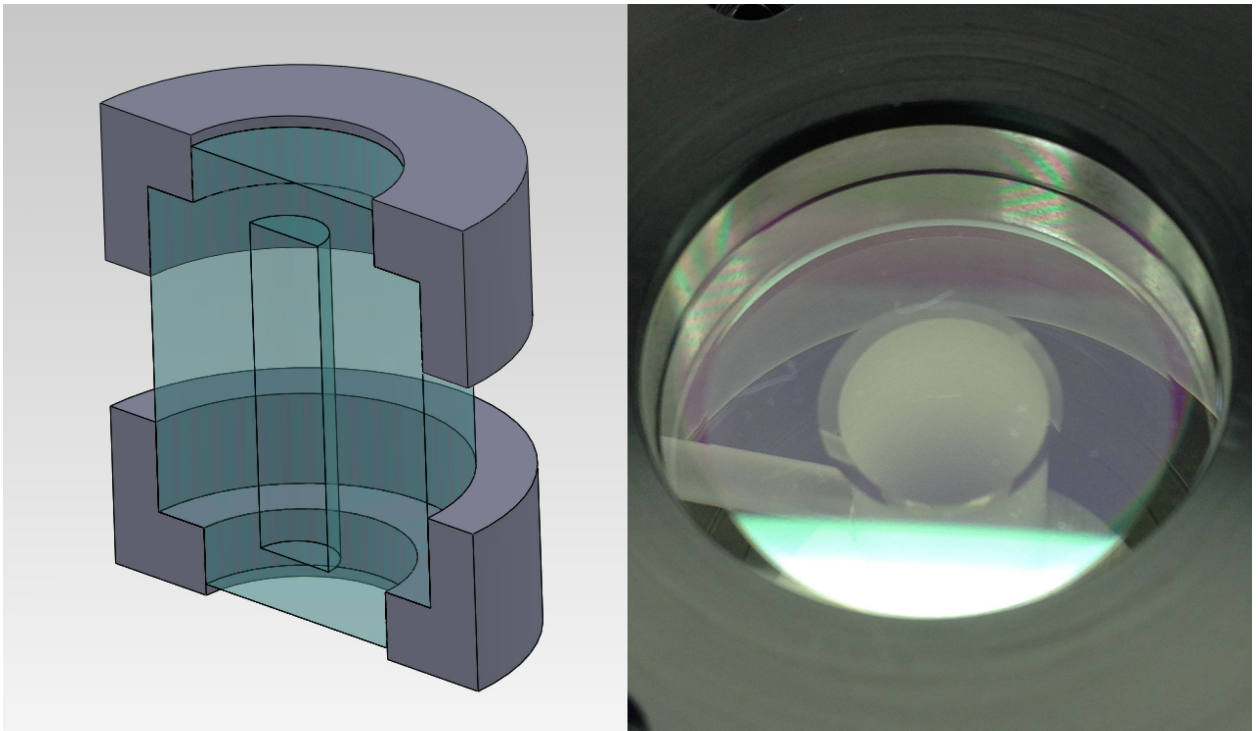


Figure E.6: a) A pair of fixtures made from Delrin keep the mirrors and the spacer in place during the bonding process. b) Unsuccessful bonding attempt can be seen from the fringes on the outer edge of the mirror.

- Leave the assembly for several hours, as the bond becomes stronger as time passes [165, 87]. It is possible that the pieces fall apart from one another due to thermal change, vibration after the bonding process. Make sure to check that the pieces are well contacted before install them in a setup.
- To remove the bonded pieces, use a razor blade and try to wedge in between the contacted surfaces. Apply a lot of isopropanol when the blade presses on the contact area.

E.3 Eigenmode study

Since all the thermal noise calculations from all parts of the cavity are done under the quasi-static assumption. This means that the thermal noise in the frequency of interest has to be lower than the first body mode of the reference cavity. It is important to calculate the eigenfrequency of the lowest body mode to make sure that the measured bandwidth is below the first eigenfrequency. COMSOL can calculate eigenmodes and associated eigenfrequencies of a body. First we try a cylindrical shape to compare the results between COMSOL and an analytical result given in situation 7b, table 16.1 of Ref. [166] as

$$f_1 = \frac{1.57}{2\pi} \sqrt{\frac{Y}{\rho l^2}}. \quad (\text{E.5})$$

Where Y is the Young's modulus of the material (72 GPa for fused silica). ρ is the mass density (2200 kg/m^3). We use l as half of the cavity length because our case has both ends of the cavity are free while the formula is for a bar with one end fixed, another end free. The first longitudinal mode frequency obtained from both methods are 74 kHz and 77 kHz, respectively, see Fig. E.7.

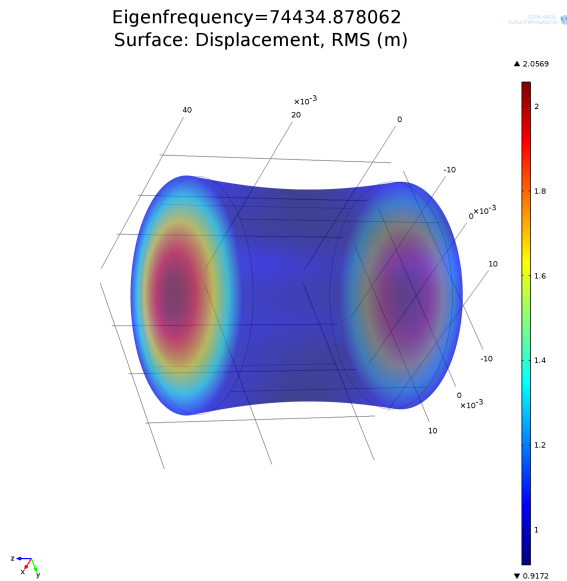


Figure E.7: COMSOL simulation for the first longitudinal mode of a cylindrical object with the same dimension as the spacer. The frequency is at 74 kHz. The color on the surface represents the rms displacement from all directions.

Once we verify that the result from COMSOL is reliable, we simulate the complete cavity with COMSOL. The lowest body mode is a radial mode at 46 kHz, and the first longitudinal mode is at 60, kHz, see Fig. E.8. The frequencies are high enough that the thermal noise calculation with quasi-static assumption is still valid.

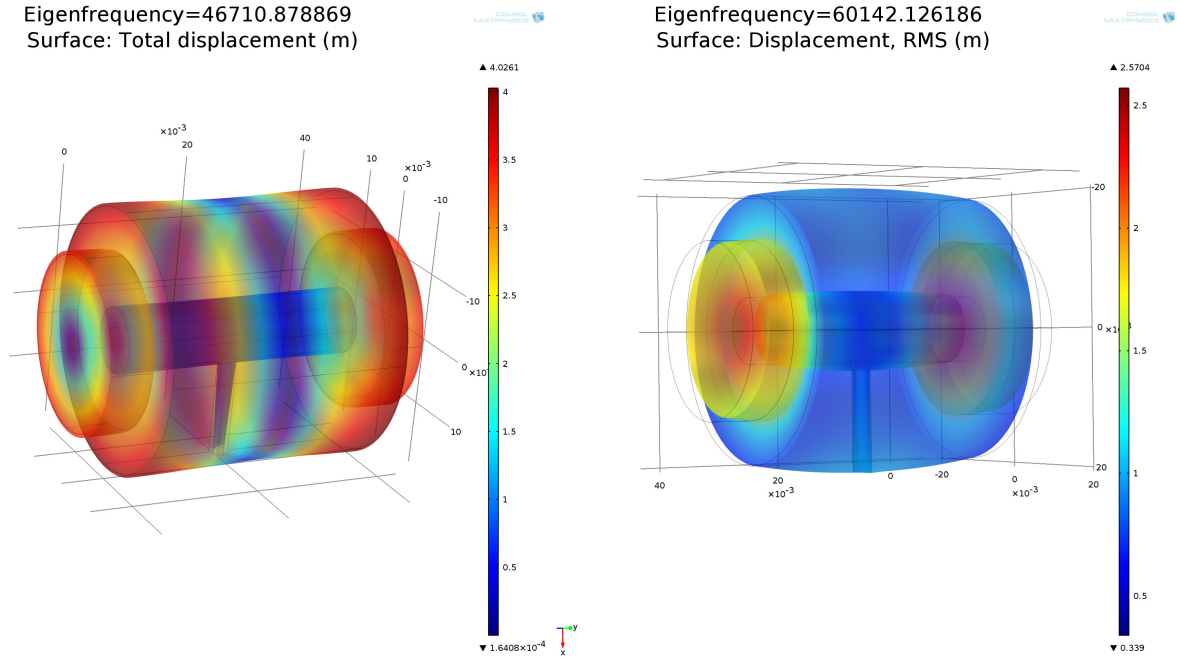


Figure E.8: COMSOL simulation for eigenfrequencies of the cavity. Left, the lowest body mode, which expands and contracts radially along the beam line, at 46.7,kHz. Right, the first longitudinal mode at 60.1,kHz. The result from the first longitudinal mode is included here because this mode directly couples into the displacement noise of the cavity and can limit the bandwidth of the frequency stabilization servo.

E.4 Searching for Optimum Support Point with COMSOL

To find the optimum support point, we ran simulations on COMSOL to compute the bending effect from different support points on the surface of the cylindrical spacer. Since the first body mode of the spacer is up to 46 kHz, cf. section E.3, we can use quasi static study for the FEA to calculate the strain at DC response and apply the result to the noise budget at frequency lower than the first body mode. The FEA results show that there is no way to completely cancel the displacement along the beam-line axis. However, tilting of the mirror can be canceled, see Fig. E.10. Our support position is chosen to be 1.17 inches apart at 30 degrees measured down from the horizontal plane.

E.5 Mount Design and Assembly

The main components of the cavity mount assembly are the following:

- **Holder:** The cavity holders keep the cavity above the stainless steel mount. They are made from Polyether ether ketone (PEEK). It is chosen for its thermal insulation and vacuum compatible [131]. They are cut from a cylinder rod and placed orthogonally to the spacer to achieve point contact support, see Fig. E.11.

Ice: Displacement field, X component (m)

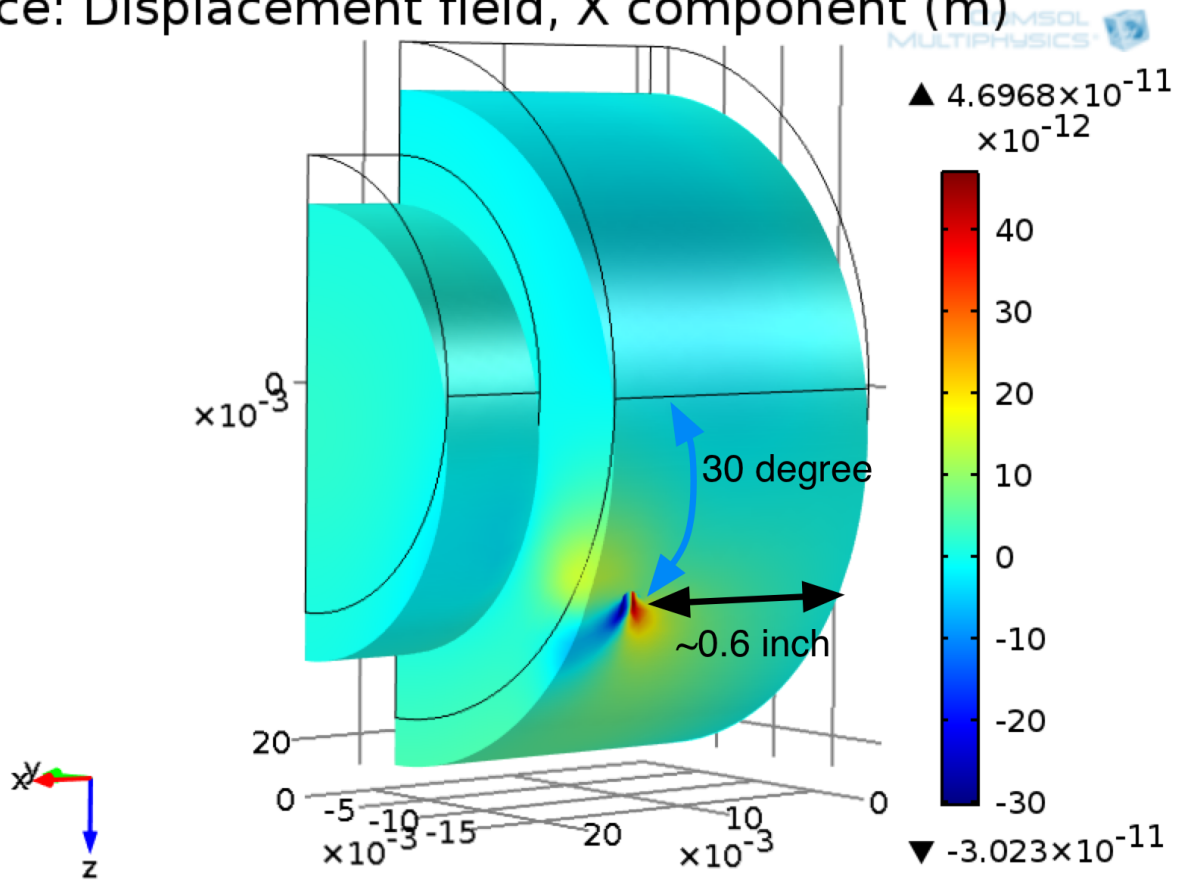


Figure E.9: COMSOL simulation for the cavity on the support bending under its weight. The simulation can be done on 1/4 of the cavity due to its symmetries. The support position is shown in the picture. The color represents the displacement along the beamline axis measured from its original position. Numbers without unit are in meter.

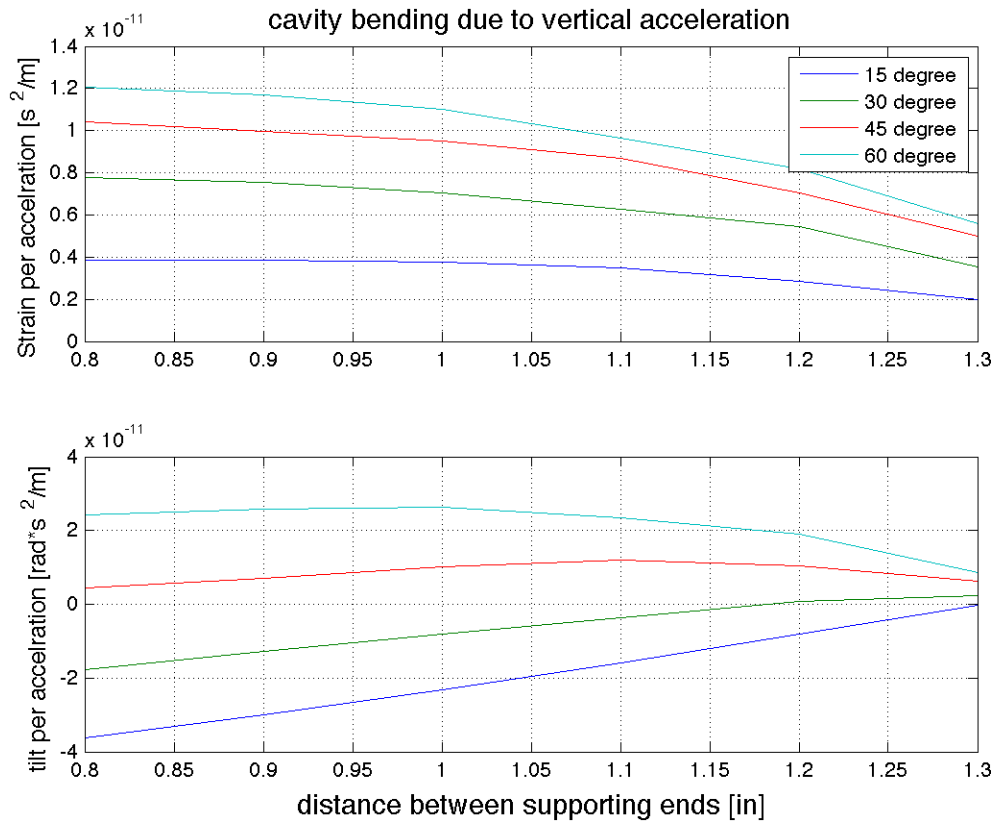


Figure E.10: Results from COMSOL simulations. The top plot shows the displacement along the beam line, the bottom plot shows how much the mirror tilt due to vertical acceleration. The plots have results from four different angle positions, 15, 30, 45, and 60 degrees. From the plots, it appears that with smaller angle (the support position is closer to the horizontal plane), the cavity will be less susceptible to the applied acceleration. However, there are a few major drawbacks. It is not practical for the design of the mount, the force between the mount and the cavity is increased and it might lead to extra loss on the spacer surface, and the tilt cannot be cancelled anymore. Hence, the chosen support position is at 30 degrees, 1.17 inch apart. The strain sensitivity to vertical acceleration is about $6 \times 10^{-12} \frac{s^2}{m}$

- **Thermal shield:** A copper tube with a heater wire wrapped around the outer surface is used as a temperature control on the cavity. The tube has four slots to let the peek supports touch the cavity.
- **Mount base:** The main structure that holds the PEEK holders, thermal shields and the cavities together. It is screwed down to the seismic isolation stack. The geometry of the mount is based on the optimum support design. The drawing is shown in Fig. E.12.

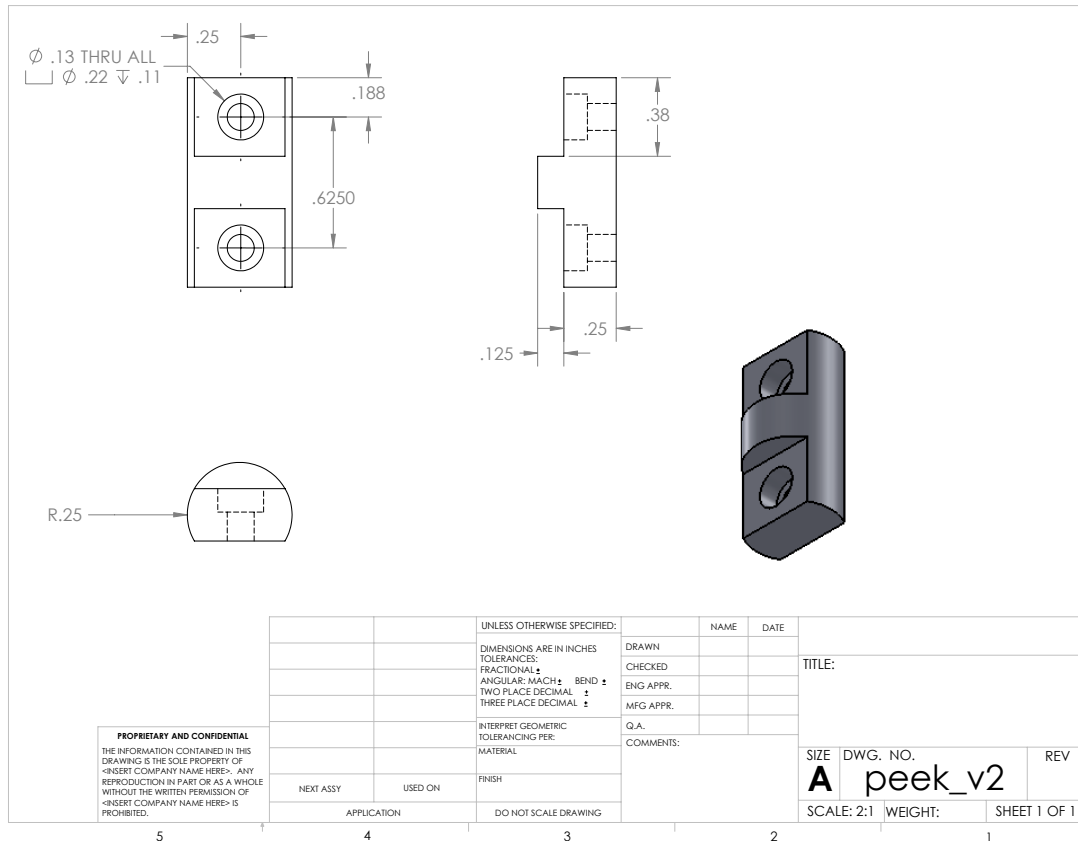


Figure E.11: A drawing of PEEK support. A piece can be cut from a commercially available PEEK rod.

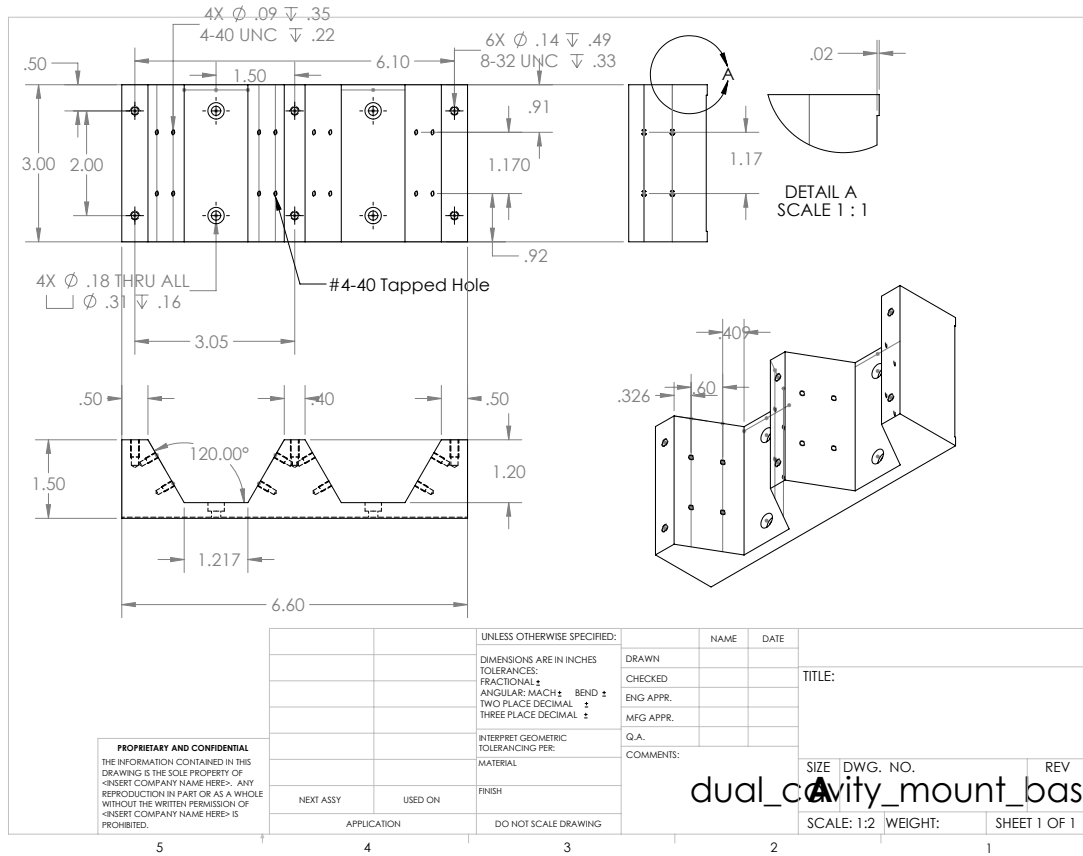


Figure E.12: A drawing of dual cavity mount base.

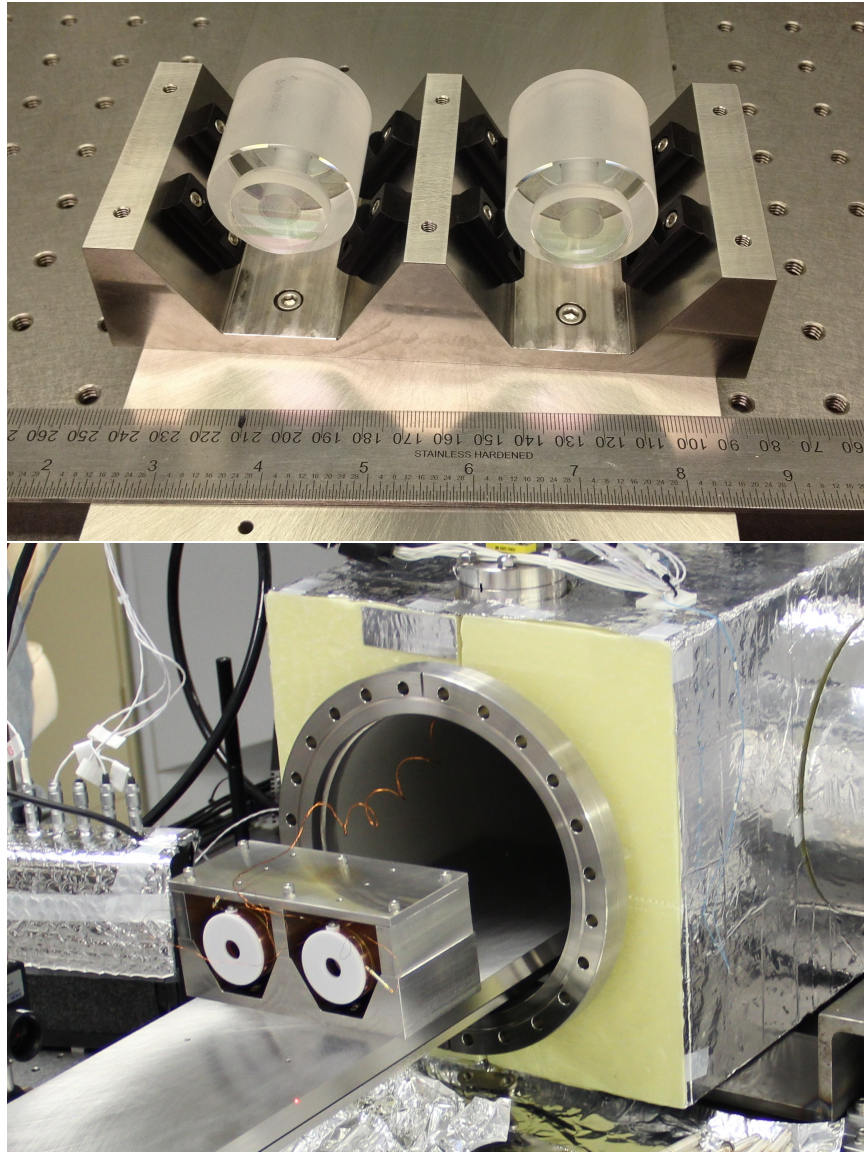


Figure E.13: Top, the cavity mount during assembly. Note: the shields are not shown here. Below, the final assembly during the final installation. The walls are for preventing thermal coupling between the two cavities.

Appendix F

Pre-Mode Cleaner Cavity

The pre-mode cleaner is used for filtering the beam profile, intensity filtering. It also acts as a stable reference for beam position. The design parameters of the PMC is shown in the table below [167].

Round trip length / FSR	0.42 m / 357 MHz
Finesse	50 (designed for P-polarization)
Cavity linewidth (FWHM)	14 MHz
Higher order mode suppression (power)	TEM ₀₁ (vertical):200, TEM ₁₀ (horizontal):780
Actuator range	PZT:2.7 FSR for 0–375V
Actuator bandwidth	First resonant of mounted PZT 10 kHz
Beam waist radius	$w_0 = 370 \mu m$
Pointing relative to optical table	$\epsilon = \sqrt{\left(\frac{dx}{w_0}\right)^2 + \left(\frac{d\alpha}{\Theta_D}\right)^2} < (3 \times 10^{-5}/f)\sqrt{Hz}$ at $f > 10Hz$

Table F.1: Design parameters of the first prototype PMC w_0 is the beam radius, Θ_D is the half angle beam divergence, dx is the displacement fluctuations, $d\alpha$ is the angular fluctuations.

F.1 Eigenmode Study

The eigenmode study is done on the PMC in order to determine its body mode frequency on the first longitudinal mode. Since the PZT actuator that keeps the cavity length moves in this direction, the highest unity gain frequency (UGF) is affected by the resonant frequencies of the PMC body and the PZT. In this case, the first resonant frequency of PZT is around 10 kHz, and 17 kHz for the PMC body. This limits the UGF to around a few kHz.

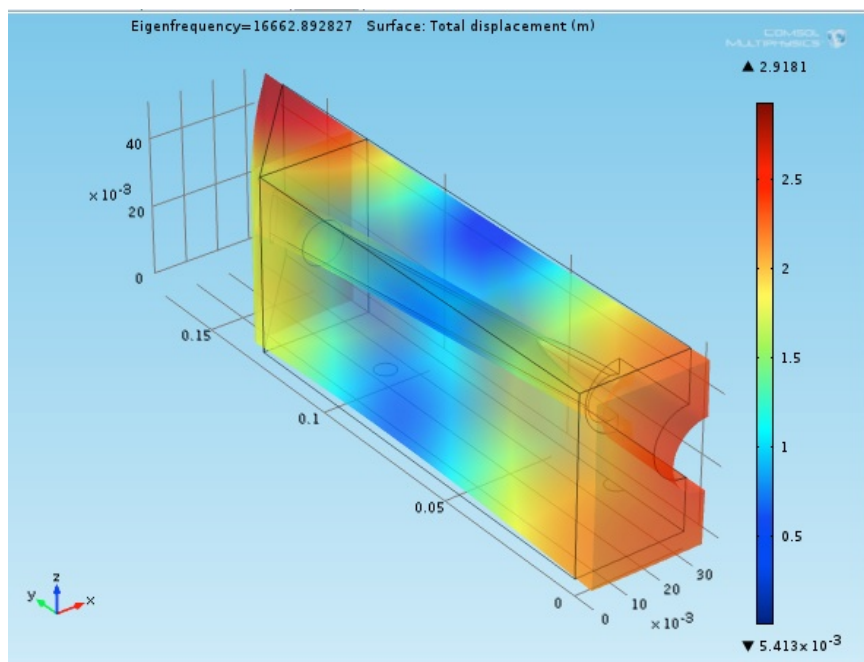


Figure F.1: First longitudinal mode of the PMC. The eigenfrequency is around 16,600 kHz.

Appendix G

Mathematical Note

G.1 Note About Fabry–Perot Cavity

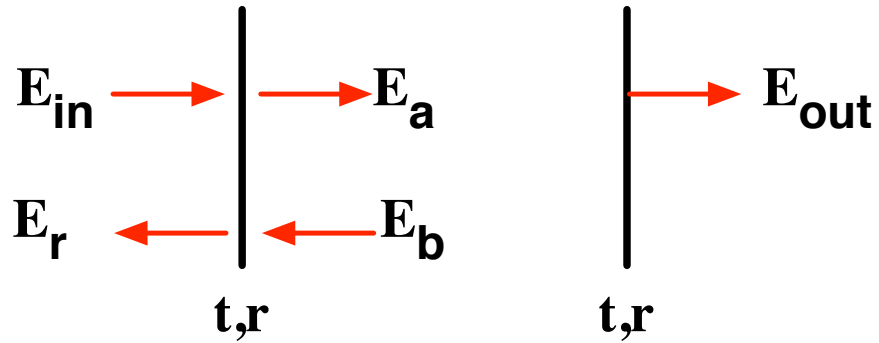


Figure G.1: E field inside a cavity formed by two similar mirrors.

$\delta = \frac{2\pi}{\lambda}L$ is the phase change during a single trip inside the cavity. We can write

$$E_{out} = E_a t e^{-i\delta}, \quad (\text{G.1a})$$

$$E_a = t E_{in} + r E_b, \quad (\text{G.1b})$$

$$E_b = E_a r e^{-2i\delta}. \quad (\text{G.1c})$$

Solving the above equations, we get

$$\frac{E_{out}}{E_{in}} = \frac{t^2 e^{-i\delta}}{1 - r^2 e^{-2i\delta}}. \quad (\text{G.2})$$

This equation explains why only certain optical frequencies are allowed to pass through a Fabry–Perot cavity (Eq. 3.1).

Next, Let's calculate the power build up in the cavity. We have to take E_a and E_b into account. For a high finesse cavity $E_a \approx E_b$, and they form a standing wave pattern. The total maximum electric field is $E_a + E_b \approx 2E_b$. Thus the amplification factor is the square of that ratio between

in-cavity electric field and the input field averaged over time (divided by a factor of 2) because of the standing wave pattern inside the cavity,

$$|P_{cav}/P_{in}| \approx \frac{1}{2} \left| \frac{2E_b}{E_{in}} \right|^2 \quad (\text{G.3a})$$

$$= \frac{2t^2 r^2}{(1-r^2)^2} \quad (\text{G.3b})$$

$$\approx \frac{2\mathcal{F}}{\pi}, \quad (\text{G.3c})$$

where $\mathcal{F} \approx \pi \frac{r}{1-r^2}$ is defined as the cavity finesse. The power build up as a function of frequency due to the cavity response is [77],

$$|P_{cav}/P_{in}(f)| = \frac{2\mathcal{F}/\pi}{1 + (f/f_{cav})^2}, \quad (\text{G.4})$$

where f_{cav} is the pole of the cavity.

G.2 Temperature Fluctuations for TO Calculation

The temperature fluctuation sensed by a Gaussian beam for TR calculation is given in Ref. [84] as (in a very simplified form where all constants in front of the integral are absorbed into one constant),

$$S_{\Delta T}^{TO} = \text{const} \int_0^\infty k_\perp e^{-k_\perp^2 w_0^2/4} dk_\perp \int_{-\infty}^\infty dk_z \frac{k_z^2 + k_\perp^2}{(k_z^2 + k_\perp^2)^2 + \Omega^2} \left(\frac{1}{1 + k_z^2 l^2} \right). \quad (\text{G.5})$$

Since the penetration depth l is typically much smaller than the beam radius, $l \ll l_{th} \ll \omega_0$, the integral is solved while assuming the last term as unity, and the denominator as constant while integrating over k_\perp .

For small spot size or low frequency where the assumption is not held, the integral can be solved analytically while ignoring the last term. The integral for k_z can be converted to a complex contour integral as

$$\int_{-\infty}^\infty dk_z \frac{k_z^2 + k_\perp^2}{(k_z^2 + k_\perp^2)^2 + \Omega^2} \rightarrow \oint dz \frac{z^2 + k^2}{(z^2 + k^2)^2 + \Omega^2} \quad (\text{G.6a})$$

$$= \oint dz \frac{z^2 + k^2}{(z^2 + k^2 + i\Omega)(z^2 + k^2 - i\Omega)} \quad (\text{G.6b})$$

$$= \oint dz \frac{z^2 + k^2}{(z + \sqrt{k^2 + i\Omega})(z - i\sqrt{k^2 + i\Omega})(z + \sqrt{k^2 - i\Omega})(z - i\sqrt{k^2 - i\Omega})} \quad (\text{G.6c})$$

$$= \oint dz \frac{z^2 + k_\perp^2}{(z - z_1)(z - z_2)(z - z_3)(z - z_4)}. \quad (\text{G.6d})$$

where,

$$z_1 = -i\sqrt{k^2 - i\Omega} \quad (\text{G.7a})$$

$$z_2 = i\sqrt{k^2 + i\Omega} \quad (\text{G.7b})$$

$$z_3 = i\sqrt{k^2 - i\Omega} \quad (\text{G.7c})$$

$$z_4 = -i\sqrt{k^2 + i\Omega} \quad (\text{G.7d})$$

Next is to find the positions of all the poles on the complex plane. $k^2 + i\Omega$ will be in the first quadrant. Its two roots, $\sqrt{k^2 + i\Omega}$, $-\sqrt{k^2 + i\Omega}$ will be in the first and third quadrant, respectively. Finally, after being multiplied by $i = e^{\frac{i\pi}{2}}$ that rotates the complex vector counter clockwise by $\pi/2$ radian, $i\sqrt{k^2 + i\Omega}$ and $-i\sqrt{k^2 + i\Omega}$ are in the second and fourth quadrants. By the same token, one can show that $i\sqrt{k^2 - i\Omega}$ and $-i\sqrt{k^2 - i\Omega}$ are in the third and first quadrants. Then, we can take the contour integral to cover the real axis and on the top half of the complex plane. So only z_1 and z_2 have to be considered during the contour integral. Using Cauchy's residue theorem, we can reduce the integral to

$$\oint f(z)dz = 0 = \int_{s_1} f(z)dz + \int_{s_2} f(z)dz + \int_{s_3} f(z)dz + \int_{s_4} f(z)dz, \quad (\text{G.8})$$

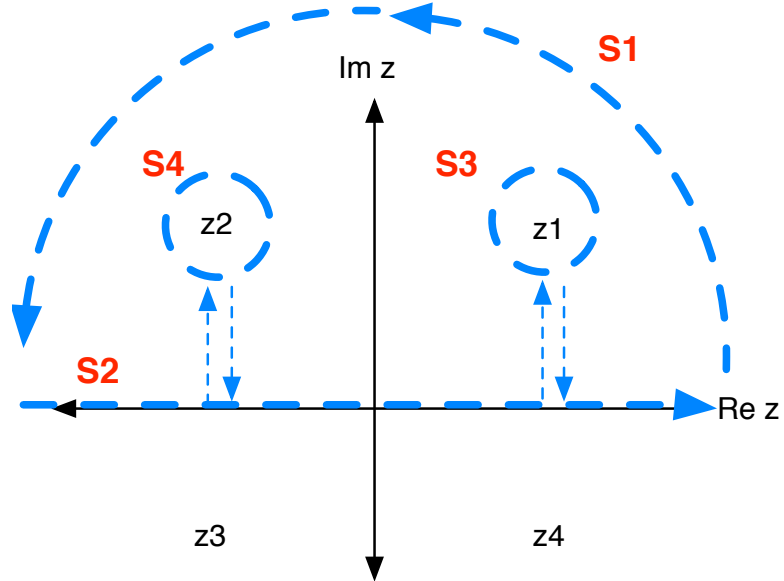


Figure G.2: The poles and their positions in the complex plane are shown in the figure. The contour line for the integrals can be separated into four line integrals. The integral along S_2 is the original integral to be solved.

where s_1 is the upper half of the circle, s_2 is the line along the real axis, s_3 is the circle around

z_1 , and s_4 is the circle around z_2 , see Fig. G.2. The first integral goes to zero, the second integral is the original integral we want to solve, the third and fourth integrals have to be evaluated,

$$\int_{s_3} f(z)dz = 2\pi i \frac{z_1^2 + k^2}{(z_1 - z_2)(z_1 - z_3)(z_1 - z_4)} \quad (\text{G.9a})$$

$$= \frac{\pi}{2\sqrt{k^2 + i\Omega}}, \quad (\text{G.9b})$$

and

$$\int_{s_4} f(z)dz = 2\pi i \frac{z_2^2 + k^2}{(z_2 - z_2)(z_2 - z_3)(z_2 - z_4)} \quad (\text{G.10a})$$

$$= \frac{-\pi}{2\sqrt{k^2 - i\Omega}}. \quad (\text{G.10b})$$

Thus,

$$\int_{-\infty}^{\infty} dk_z \frac{k_z^2 + k_{\perp}^2}{(k_z^2 + k_{\perp}^2)^2 + \Omega^2} = \int_{s_2} f(z)dz = - \left(\int_{s_3} f(z)dz + \int_{s_4} f(z)dz \right) \quad (\text{G.11a})$$

$$= \frac{\pi}{2} \left(\frac{\sqrt{k^2 + i\Omega} - \sqrt{k^2 - i\Omega}}{\sqrt{k^4 + \Omega^2}} \right) \quad (\text{G.11b})$$

$$= \pi \frac{\text{Re}[\sqrt{k^2 + i\Omega}]}{\sqrt{k^4 + \Omega^2}}. \quad (\text{G.11c})$$

By changing the variable k to u and rearranging all the constants, we show that the double integrals of k_z and k_{\perp} in Eq. G.5 can be reduced to a single integral as seen in Eq. 2.25

G.3 Error Analysis of the Measurement

As we use Eq. 2.16 to fit for the effective loss angle ϕ_c , uncertainties in various parameters can cause the error in ϕ_c . The summary of the effects from each parameters are given in Tab. G.1. An error in each parameter is propagated forward by thermal noise equation using Eq. 2.20. The root square sum of the error is 7.34 percent in $[Hz^2/Hz]$. This yields the error in the effective loss angle to be $\delta\phi_c = \pm 0.3$.

Parameter	Value	Contribution @100 Hz in % PSD
Y_{SiO_2}	72 ± 6 GPa	0.3
$Y_{Ta_2O_5}$	140 ± 20 GPa	7.2
Coating thickness	4.54 ± 0.02 μm	0.4
Cavity length	1.45 ± 0.01 inch	0.6
Mirror ROC	500 ± 3 mm	(causes spot size error)
Spot size	182 ± 0.5 μm	0.55
Temperature	308 ± 2 ,K	0.65
PLL calibration	710 ± 5 Hz/V	0.7
errors in the noise budget		0.4
root square sum		7.34

Table G.1: Errors contributed from various consideration. Values and errors of the material parameters are taken from [101, 159, 168]

G.4 Bayesian Analysis

We use Bayesian probability to determine the mechanical loss angles of SiO_2 and Ta_2O_5 because it should provide us with more reliable answers. Due to the rapid improvement of coating technology over the past decade, we only have a single coating measurement where the sample was manufactured by the similar vendor with similar equipment to those of our samples. We will use the result from [51] as the prior for our Bayesian analysis.

Given ϕ_c , a knowledge of the parameters of our coatings, and prior observations of coating loss angles, we can make a Bayesian estimate of ϕ_L and ϕ_H . To do this, we first write down a formula relating ϕ_c , ϕ_L and ϕ_H :

$$\mathcal{M}\phi_c = \Xi_L N_L d_L \phi_L + \Xi_H N_H d_H \phi_H. \quad (G.12)$$

Here $\mathcal{M} = (1 + \sigma_s)(1 - 2\sigma_s)d/E_s$, $N_L = 15$, $N_H = 14$, $d_L = \lambda/4n_L$, and $d_H = \lambda/4n_H$. The coefficients Ξ_L and Ξ_H are found by combining Table 1, and Eqs. 94 and 96 from Ref. [53], assuming zero light penetration into the coating. These coefficients depend only on the coating parameters. Next we write down Bayes's theorem [169]:

$$p(\phi_L, \phi_H | \hat{\phi}_c) = \frac{1}{Z} \mathcal{L}(\phi_L, \phi_H | \hat{\phi}_c) p(\phi_L, \phi_H), \quad (G.13)$$

where Z is a normalization. As a prior, we use data from the ring down measurements in Ref. [51], since these measurements were performed on coatings from the same manufacturer as in our experiment, and were made during a similar time period. Harry's quoted quantity $\phi_{||}$ is related to the

material loss angles ϕ_L and ϕ_H via

$$(E_L d_L + E_H d_H) \phi_{\parallel} = E_L d_L \phi_L + E_H d_H \phi_H. \quad (\text{G.14})$$

We use $\hat{\phi}_{\parallel} \pm \sigma_{\hat{\phi}_{\parallel}} = (5.2 \pm 0.3) \times 10^{-4}$ as the value measured by Harry et al. ¹.

We then construct the prior

$$p(\phi_L, \phi_H) = \frac{1}{Z_0} \exp \left[-\frac{1}{2} \frac{(\hat{\phi}_{\parallel} - \phi_{\parallel})^2}{\sigma_{\hat{\phi}_{\parallel}}^2 + \sigma_{\phi_{\parallel}}^2} \right], \quad (\text{G.15})$$

where Z_0 is a normalization, ϕ_{\parallel} is related to ϕ_L and ϕ_H via eq. G.14, and $\sigma_{\phi_{\parallel}}$ is found by propagating forward the uncertainties on the material parameters as given in appendix C.

As a likelihood we take

$$\mathcal{L}(\phi_L, \phi_H | \hat{\phi}_c) = \exp \left[-\frac{1}{2} \frac{(\hat{\phi}_c - \phi_c)^2}{\sigma_{\hat{\phi}_c}^2 + \sigma_{\phi_c}^2} \right] \quad (\text{G.16})$$

with $\hat{\phi}_c$ given by our measurement, and ϕ_c given by Equation G.12.

The prior, the likelihood, and the resulting posterior are shown in Figures G.3–G.5. By marginalizing the posterior for each loss angle, we find that the median estimates are $\phi_L = 1.6_{-1.0}^{+1.3} \times 10^{-4}$ and $\phi_H = 8.0_{-1.4}^{+1.4} \times 10^{-4}$, where the error bars indicate 68 % credible intervals.

¹Harry originally determined $\hat{\phi}_{\parallel} \pm \sigma_{\hat{\phi}_{\parallel}} = (1.0 \pm 0.3) \times 10^{-4}$ using a coating thickness that was 5 times the actual value. Taking into account the correction given in Penn et al. [99], we arrive at $\hat{\phi}_{\parallel} \pm \sigma_{\hat{\phi}_{\parallel}} = (5.2 \pm 0.3) \times 10^{-4}$, assuming that the uncertainty is dominated by systematics that do not scale with the nominal value of the loss angle.

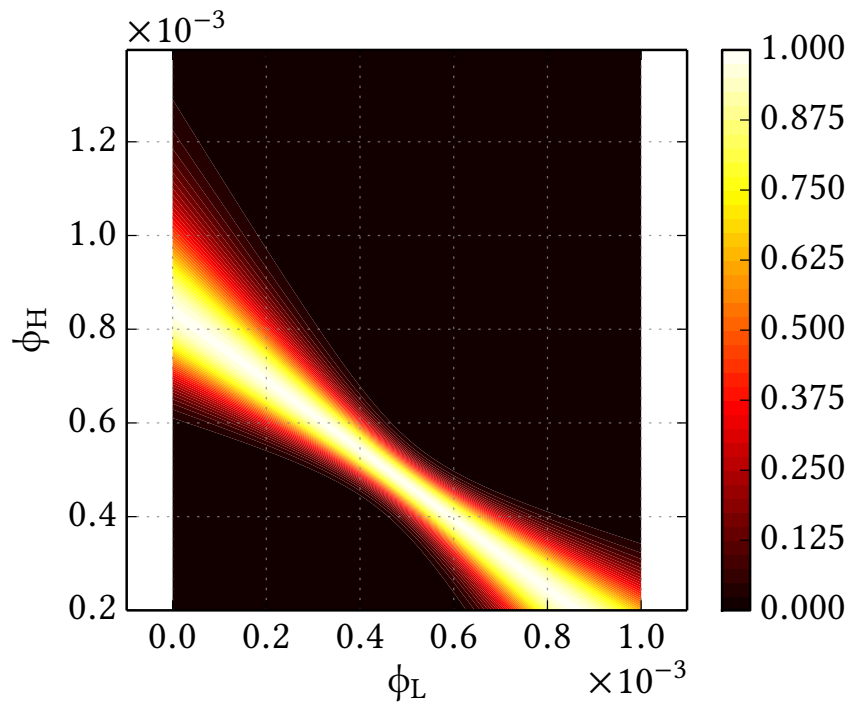


Figure G.3: Prior PDF, after Harry et al. [51]. Picture credit: Evan Hall.

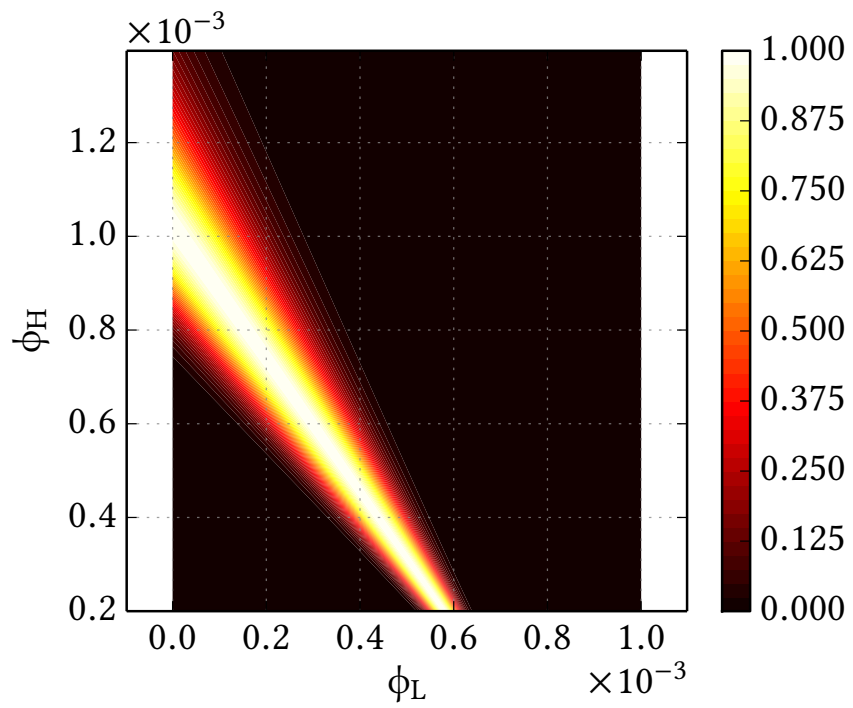


Figure G.4: Likelihood. Picture credit: Evan Hall.

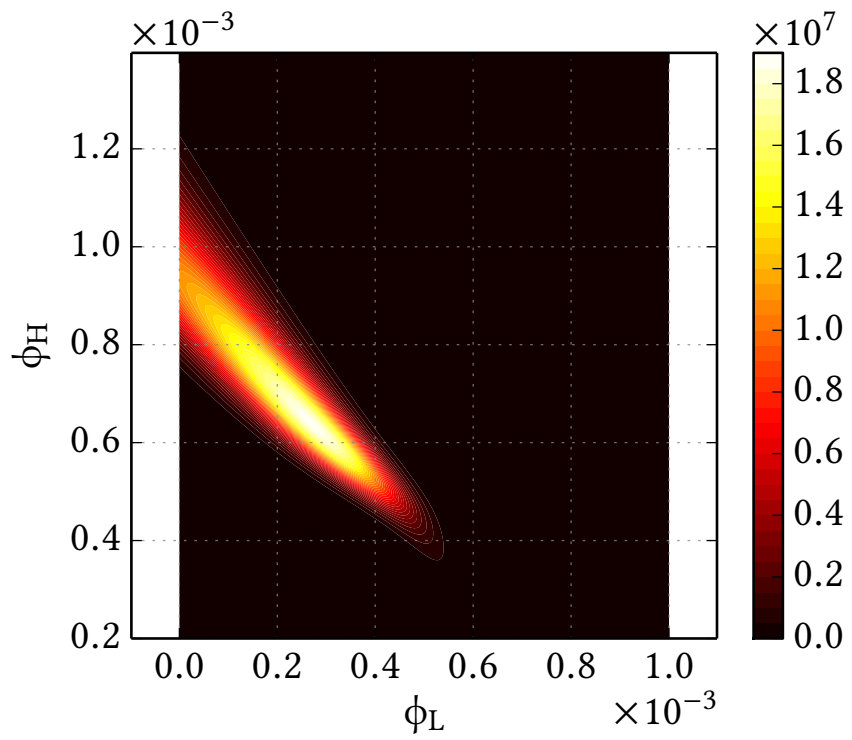


Figure G.5: Posterior PDF. Picture credit: Evan Hall.

Bibliography

- [1] Robert Brown. A Brief Account of Microscopical Observations made in the Months of June, July and August, 1827, on the Particles Contained in the Pollen of Plants; and on the General Existence of Active Molecules in Organic and Inorganic Bodies. A portion of it is reproduced in *A Source Book in Physics(1935), pp. 251-255.
- [2] Albert Einstein. ber die von der molekularkintischen theorie der warme geforderte bewegung von in ruhenden flussigkeiten. *Annalen der Physik*, 322:549–560, 1905.
- [3] Jean Perrin. Mouvement brownien et réaliité moléculaire. *Annales de Chimie et de Physique*, 18:5–104, 1909.
- [4] Robert Andrews Millikan, Duane Roller, and Earnest Charles Watson. *Mechanics, Molecular Physics, Heat, and Sound*. Ginn and Company, 1937.
- [5] J. B. Johnson. Thermal agitation of electricity in conductors. *Phys. Rev.*, 32:97–109, Jul 1928.
- [6] H. Nyquist. Thermal agitation of electric charge in conductors. *Phys. Rev.*, 32:110–113, Jul 1928.
- [7] Richard F. Voss and John Clarke. Flicker (1f) noise: Equilibrium temperature and resistance fluctuations. *Phys. Rev. B*, 13:556–573, Jan 1976.
- [8] J. W. Eberhard and P. M. Horn. Temperature dependence of 1f noise in silver and copper. *Phys. Rev. Lett.*, 39:643–646, Sep 1977.
- [9] Frank Seifert. Resistor current noise measurement. Technical Report LIGO-T0900200-v11, LIGO/Caltech, 2009.
- [10] Frank Seifert. *Power Stabilization of High Power Lasers for Second Generation Gravitational Wave Detectors*. PhD thesis, Leibniz Universitat Hannover, 2010.
- [11] D. M. Fleetwood, J. T. Masden, and N. Giordano. 1f. *Phys. Rev. Lett.*, 50:450–453, Feb 1983.
- [12] J. W. Eberhard, P. Dutta, and P. M. Horn. Reply to ”comment on 1f noise and its temperature dependence” in silver and copper. *Phys. Rev. B*, 19:1307–1309, Jan 1979.

- [13] F Mohd-Yasin, D J Nagel, and C E Korman. Noise in mems. *Measurement Science and Technology*, 21(1):012001, 2010.
- [14] T.B. Gabrielson. Mechanical-thermal noise in micromachined acoustic and vibration sensors. *Electron Devices, IEEE Transactions on*, 40(5):903–909, May 1993.
- [15] R.P. Leland. Mechanical-thermal noise in mems gyroscopes. *Sensors Journal, IEEE*, 5(3):493–500, 2005.
- [16] Rodney S. Tucker, D.M. Baney, W.V. Sorin, and Curt A. Flory. Thermal noise and radiation pressure in mems fabry-perot tunable filters and lasers. *Selected Topics in Quantum Electronics, IEEE Journal of*, 8(1):88–97, 2002.
- [17] Henry Cavendish. In MacKenzie, A. S. *Scientific Memoirs Vol.9: The Laws of Gravitation*. American Book Co. (published 1900). pp. 59–105. Retrieved 2014-04-01. Online copy of Cavendish’s 1798 paper, and other early measurements of gravitational constant.
- [18] Thibault Damour. Testing the equivalence principle: why and how? *Classical and Quantum Gravity*, 13(11A):A33, 1996.
- [19] S. Schlamminger, K.-Y. Choi, T. A. Wagner, J. H. Gundlach, and E. G. Adelberger. Test of the equivalence principle using a rotating torsion balance. *Phys. Rev. Lett.*, 100:041101, Jan 2008.
- [20] H.B.G. Casimir. On the attraction between two perfectly conducting plates. *Proc. K. Ned. Akad. Wet.*, 51, 1948.
- [21] S. K. Lamoreaux. Demonstration of the casimir force in the 0.6 to 6 μm range. *Phys. Rev. Lett.*, 78:5–8, Jan 1997.
- [22] Erwin J. Saxl and Mildred Allen. 1970 solar eclipse as ”seen” by a torsion pendulum. *Phys. Rev. D*, 3:823–825, Feb 1971.
- [23] A.F. Pugach, M.M. Medvedskii, N.N. Peretyatko, V.I. Shavlovskii, V.L. Karbovskii, T.V. Nikityuk, P.F. Lazorenko, A.V. Zolotukhina, D.P. Vorobyev, V.A. Pap, G.A. Lazorenko, I.P. Vedenicheva, S.V. Shatokhina, and N.M. Kostogryz. The first experience of solar eclipse observations with a miniature torsion balance. *Kinematics and Physics of Celestial Bodies*, 24(5):253–258, 2008.
- [24] Gabriela I. Gonzalez and Peter R. Saulson. Brownian motion of a torsion pendulum with internal friction. *Physics Letters A*, 201(1):12 – 18, 1995.

- [25] S. A. Diddams, Th. Udem, J. C. Bergquist, E. A. Curtis, R. E. Drullinger, L. Hollberg, W. M. Itano, W. D. Lee, C. W. Oates, K. R. Vogel, and D. J. Wineland. An optical clock based on a single trapped 199Hg^+ ion. *Science*, 293(5531):825–828, 2001.
- [26] Masao Takamoto, Feng-Lei Hong, Ryoichi Higashi, and Hidetoshi Katori. An optical lattice clock. *Nature*, 435, 2005.
- [27] Michael J. Martin. *Quantum Metrology and Many-Body Physics: Pushing the Frontier of the Optical Lattice Clock*. PhD thesis, University of Colorado, 2013.
- [28] Albert Einstein. Näherungsweise Integration der Feldgleichungen der Gravitation. *Sitzungsberichte der Königlich Preussischen Akademie der Wissenschaften (Berlin)*, 33:688–696, 1916.
- [29] A. Einstein. Über Gravitationswellen. *Sitzungsberichte der Königlich Preussischen Akademie der Wissenschaften (Berlin)*, 8:154–167, January 1918.
- [30] A. Einstein and A.J. Engel. *The Collected Papers of Albert Einstein: The Berlin Years: Writings, 1914-1917*. The Collected Papers of Albert Einstein. Princeton University Press, 1997.
- [31] R.A. Hulse and J.H. Taylor. Discovery of a pulsar in a binary system. *Astrophysical Journal*, 195, Jan 1975.
- [32] J. H. Taylor, L. A. Fowler, and P. M. McCulloch. Measurements of general relativistic effects in the binary pulsar psr1913 + 16. *Nature*, 277, 1979.
- [33] Joel M. Weisberg and Joseph H. Taylor. Relativistic binary pulsar B1913+16: Thirty years of observations and analysis. *ASP Conf.Ser.*, 328:25, 2005.
- [34] R. W. Ogburn IV, P. A. R. Ade, R. W. Aikin, M. Amiri, S. J. Benton, J. J. Bock, J. A. Bonetti, J. A. Brevik, B. Burger, C. D. Dowell, L. Duband, J. P. Filippini, S. R. Golwala, M. Halpern, M. Hasselfield, G. Hilton, V. V. Hristov, K. Irwin, J. P. Kaufman, B. G. Keating, J. M. Kovac, C. L. Kuo, A. E. Lange, E. M. Leitch, C. B. Netterfield, H. T. Nguyen, A. Orlando, C. L. Pryke, C. Reintsema, S. Richter, J. E. Ruhl, M. C. Runyan, C. D. Sheehy, Z. K. Staniszewski, S. A. Stokes, R. V. Sudiwala, G. P. Teply, J. E. Tolan, A. D. Turner, P. Wilson, and C. L. Wong. The bicep2 cmb polarization experiment. *Proc. SPIE*, 7741:77411G–77411G–11, 2010.
- [35] David A. Aguilar and Christine Pulliam. First direct evidence of cosmic inflation, 2014. <http://www.cfa.harvard.edu/news/2014-05>.
- [36] Alex Abramovici et al. Ligo: The laser interferometer gravitational-wave observatory. *Science*, 256(5055):325–333, 1992.

- [37] T Accadia. et al. Virgo: a laser interferometer to detect gravitational waves. *Journal of Instrumentation*, 7(03):P03012, 2012.
- [38] H Grote and LIGO Scientific Collaboration. The status of geo 600. *Classical and Quantum Gravity*, 25(11):114043, 2008.
- [39] Kentaro Somiya. Detector configuration of kagrathe japanese cryogenic gravitational-wave detector. *Classical and Quantum Gravity*, 29(12):124007, 2012.
- [40] S. M. Carroll. *An Introduction to General Relativity Spacetime and Geometry*. Addison Wesley, 2004.
- [41] Edmund Bertschinger and Edwin F. Taylor. Gravitational waves. Available online at <http://www.eftaylor.com/exploringblackholes/GravWaves100707V2.pdf>.
- [42] Rana X. Adhikari. Gravitational radiation detection with laser interferometry. *Rev. Mod. Phys.*, 86:121–151, Feb 2014.
- [43] Rana Adhikari, Guido Mueller, Norna Robertson, David McClelland, Yanbei Chen, Sam Waldman, Koji Arai, and Gregg Harry. Lsc instrument science white paper. Technical Report LIGO-T980045-00-D, LIGO/Caltech/MIT, 2011.
- [44] N A Robertson, G Cagnoli, D R M Crooks, E Elliffe, J E Faller, P Fritschel, S Goler, A Grant, A Heptonstall, J Hough, H Lck, R Mittleman, M Perreux-Lloyd, M V Plissi, S Rowan, D H Shoemaker, P H Sneddon, K A Strain, C I Torrie, H Ward, and P Willems. Quadruple suspension design for advanced ligo. *Classical and Quantum Gravity*, 19(15):4043, 2002.
- [45] G. Cagnoli, L. Gammaitoni, J. Hough, J. Kovalik, S. McIntosh, M. Punturo, and S. Rowan. Very high q measurements on a fused silica monolithic pendulum for use in enhanced gravity wave detectors. *Phys. Rev. Lett.*, 85:2442–2445, Sep 2000.
- [46] Bram Johannes Jozef Slagmolen. *Direct Measurement of the Spectral Distribution of Thermal Noise*. PhD thesis, The Australian National University, 2004.
- [47] Eric Quintero, Eric Gustafson, and Rana Adhikari. Experiment to investigate crackling noise in maraging steel blade springs. Technical Report LIGO-T1300465-v2, LIGO/Caltech, 2013.
- [48] H. J. Kimble, Yuri Levin, Andrey B. Matsko, Kip S. Thorne, and Sergey P. Vyatchanin. Conversion of conventional gravitational-wave interferometers into quantum nondemolition interferometers by modifying their input and/or output optics. *Phys. Rev. D*, 65:022002, Dec 2001.

- [49] Jan Harms, Yanbei Chen, Simon Chelkowski, Alexander Franzen, Henning Vahlbruch, Karsten Danzmann, and Roman Schnabel. Squeezed-input, optical-spring, signal-recycled gravitational-wave detectors. *Phys. Rev. D*, 68:042001, Aug 2003.
- [50] N. Nakagawa, A. M. Gretarsson, E. K. Gustafson, and M.M. Fejer. Thermal noise in half-infinite mirrors with nonuniform loss: A slab of excess loss in a half-infinite mirror. *Physical Review D*, 65(102001), 2002.
- [51] Gregory M Harry, Andri M Gretarsson, Peter R Saulson, Scott E Kittelberger, Steven D Penn, William J Startin, Sheila Rowan, Martin M Fejer, D R M Crooks, Gianpietro Cagnoli, Jim Hough, and Norio Nakagawa. Thermal noise in interferometric gravitational wave detectors due to dielectric optical coatings. *Classical and Quantum Gravity*, 19(5):897, 2002.
- [52] Kentaro Somiya and Kazuhiro Yamamoto. Coating thermal noise of a finite-size cylindrical mirror. *Phys. Rev. D*, 79:102004, May 2009.
- [53] Ting Hong, Huan Yang, Eric K. Gustafson, Rana X. Adhikari, and Yanbei Chen. Brownian thermal noise in multilayer coated mirrors. *Phys. Rev. D*, 87:082001, Apr 2013.
- [54] Kenji Numata, Masaki Ando, Kazuhiro Yamamoto, Shigemi Otsuka, and Kimio Tsubono. Wide-band direct measurement of thermal fluctuations in an interferometer. *Physical Review Letters*, 91(26), 2004.
- [55] Eric D. Black, Akira Villar, Kyle Barbary, Adam Bushmaker, Jay Heefner, Seiji Kawamura, Fumiko Kawazoe, Luca Matone, Sharon Meidt, Shanti R. Rao, Kevin Schulz, Michael Zhang, and Kenneth G. Libbrecht. Direct observation of broadband coating thermal noise in a suspended interferometer. *Physics Letters A*, 328(1):1 – 5, 2004.
- [56] A. D. Ludlow, X. Huang, M. Notcutt, T. Zanon-Willette, S. M. Foreman, M. M. Boyd, S. Blatt, and J. Ye. Compact, thermal-noise-limited optical cavity for diode laser stabilization at 1×10^{-15} . *Opt. Lett.*, 32(6):641–643, Mar 2007.
- [57] J. Alnis, A. Matveev, N. Kolachevsky, Th. Udem, and T. W. Hänsch. Subhertz linewidth diode lasers by stabilization to vibrationally and thermally compensated ultralow-expansion glass fabry-pérot cavities. *Phys. Rev. A*, 77:053809, May 2008.
- [58] S. A. Webster, M. Oxborrow, S. Pugla, J. Millo, and P. Gill. Thermal-noise-limited optical cavity. *Phys. Rev. A*, 77:033847, Mar 2008.
- [59] Kenji Numata, Amy Kemery, and Jordan Camp. Thermal-noise limit in the frequency stabilization of lasers with rigid cavities. *Physical Review Letters*, 93(250602), 2004.

- [60] Thomas Kessler, Thomas Legero, and Uwe Sterr. Thermal noise in optical cavities revisited. *J. Opt. Soc. Am. B*, 29(1):178–184, Jan 2012.
- [61] Herbert B. Callen and Richard F. Greene. On a theorem of irreversible thermodynamics. *Physical Review*, 86(5), 1952.
- [62] G V Chester. The theory of irreversible processes. *Reports on Progress in Physics*, 26(1):411, 1963.
- [63] R Kubo. The fluctuation-dissipation theorem. *Reports on Progress in Physics*, 29(1):255, 1966.
- [64] Peter R. Saulson. Thermal noise in mechanical experiments. *Physical Review D*, 42(8), 1990.
- [65] A. Gillespie and F. Raab. Thermally excited vibrations of the mirrors of laser interferometer gravitational-wave detectors. *Phys. Rev. D*, 52:577–585, Jul 1995.
- [66] Yu. Levin. Internal thermal noise in the ligo test masses: A direct approach. *Phys. Rev. D*, 57:659–663, Jan 1998.
- [67] Gabriela I. Gonzalez and Peter R. Saulson. Brownian motion of a mass suspended by an anelastic wire. *J. Acoust. Soc. Am.*, 96(207), 1994.
- [68] Clarence Zener. Internal friction in solids. i. theory of internal friction in reeds. *Phys. Rev.*, 52:230–235, Aug 1937.
- [69] J. L. Routbort and H. S. Sack. Background internal friction of some pure metals at low frequencies. *Journal of Applied Physics*, 37(13):4803–4805, 1966.
- [70] Clarence Zener. Internal friction in solids ii. general theory of thermoelastic internal friction. *Phys. Rev.*, 53:90–99, Jan 1938.
- [71] L. D. Landau and E. M. Lifshitz. *Statistical Physics*. Pergamon Press, 3rd edition, 1984.
- [72] Yuk Tung Liu and Kip S. Thorne. Thermoelastic noise and homogeneous thermal noise in finite sized gravitational-wave test masses. *Physical Review D*, 62(122002), 2000.
- [73] Yuri Levin. Fluctuationdissipation theorem for thermo-refractive noise. *Physics Letters A*, 372(12):1941 – 1944, 2008.
- [74] M. Evans, S. Ballmer, M. Fejer, P. Fritschel, G. Harry, and G. Ogin. Thermo-optic noise in coated mirrors for high-precision optical measurements. *Phys. Rev. D*, 78:102003, Nov 2008.
- [75] L. D. Landau and E. M. Lifshitz. *Theory of Elasticity*. Pergamon Press, 3rd edition, 1986.

- [76] V.B. Braginsky, M.L. Gorodetsky, and S.P. Vyatchanin. Thermodynamical fluctuations and photo-thermal shot noise in gravitational wave antennae. *Physics Letters A*, 264(1):1 – 10, 1999.
- [77] M. Cerdonio, L. Conti, A. Heidmann, and M. Pinard. Thermoelastic effects at low temperatures and quantum limits in displacement measurements. *Phys. Rev. D*, 63:082003, Mar 2001.
- [78] M. M. Fejer, S. Rowan, G. Cagnoli, D. R. M. Crooks, A. Gretarsson, G. M. Harry, J. Hough, S. D. Penn, P. H. Sneddon, and S. P. Vyatchanin. Thermoelastic dissipation in inhomogeneous media: loss measurements and displacement noise in coated test masses for interferometric gravitational wave detectors. *Phys. Rev. D*, 70:082003, Oct 2004.
- [79] Eric D. Black, Akira Villar, and Kenneth G. Libbrecht. Thermoelastic-damping noise from sapphire mirrors in a fundamental-noise-limited interferometer. *Physical Review Letters*, 93(241101), 2004.
- [80] D. Heinert, A. G. Gurkovsky, R. Nawrodt, S. P. Vyatchanin, and K. Yamamoto. Thermorefractive noise of finite-sized cylindrical test masses. *Phys. Rev. D*, 84:062001, Sep 2011.
- [81] Lingze Duan. General treatment of the thermal noises in optical fibers. *Phys. Rev. A*, 86:023817, Aug 2012.
- [82] Gregory M. Harry, Helena Armandula, Eric Black, D. R. M. Crooks, Gianpietro Cagnoli, Jim Hough, Peter Murray, Stuart Reid, Sheila Rowan, Peter Sneddon, Martin M. Fejer, Roger Route, and Steven D. Penn. Thermal noise from optical coatings in gravitational wave detectors. *Appl. Opt.*, 45(7):1569–1574, Mar 2006.
- [83] V.B. Braginsky and S.P. Vyatchanin. Thermodynamical fluctuations in optical mirror coatings. *Physics Letters A*, 312(34):244 – 255, 2003.
- [84] V.B. Braginsky, M.L. Gorodetsky, and S.P. Vyatchanin. Thermo-refractive noise in gravitational wave antennae. *Physics Letters A*, 271(56):303 – 307, 2000.
- [85] Alessandro Farsi, Mario Siciliani de Cumis, Francesco Marino, and Francesco Marin. Photothermal and thermo-refractive effects in high reflectivity mirrors at room and cryogenic temperature. *Journal of Applied Physics*, 111(4):043101, 2012.
- [86] Dana Z. Anderson. Alignment of resonant optical cavities. *Appl. Opt.*, 23(17):2944–2949, Sep 1984.
- [87] Jan Haisma, Nico Hattu, J. T. C. M. (Dook) Pulles, Esther Steding, and Jan C. G. Vervest. Direct bonding and beyond. *Appl. Opt.*, 46(27):6793–6803, Sep 2007.

- [88] Chris Myatt, Nick Traggis, and Kathryn Li Dessau. Optical fabrication: Optical contacting grows more robust. *Laser Focus World*, 42, 2006.
- [89] Alix Preston, Benjamin Balaban, G Boothe, and Guido Mueller. Stable materials and bonding techniques for space-based optical systems. In *NASA Science and Technology Conference, Session C1 P3*, 2007.
- [90] P H Sneddon, S Bull, G Cagnoli, D R M Crooks, E J Elliffe, J E Faller, M M Fejer, J Hough, and S Rowan. The intrinsic mechanical loss factor of hydroxy-catalysis bonds for use in the mirror suspensions of gravitational wave detectors. *Classical and Quantum Gravity*, 20(23):5025, 2003.
- [91] Rei Weiss. Concerning: Mechanical noise from optical contacting. Technical Report T880017, LIGO/MIT, 1989.
- [92] I W Martin, E Chalkley, R Nawrodt, H Armandula, R Bassiri, C Comtet, M M Fejer, A Grestarsson, G Harry, D Heinert, J Hough, I MacLaren, C Michel, J-L Montorio, N Morgado, S Penn, S Reid, R Route, S Rowan, C Schwarz, P Seidel, W Vodel, and A L Woodcraft. Comparison of the temperature dependence of the mechanical dissipation in thin films of ta 2 o 5 and ta 2 o 5 doped with tio 2. *Classical and Quantum Gravity*, 26(15):155012, 2009.
- [93] I W Martin, R Nawrodt, K Craig, C Schwarz, R Bassiri, G Harry, J Hough, S Penn, S Reid, R Robie, and S Rowan. Low temperature mechanical dissipation of an ion-beam sputtered silica film. *Classical and Quantum Gravity*, 31(3):035019, 2014.
- [94] M. E. Fine, H. Van Duyne, and Nancy T. Kenney. Lowtemperature internal friction and elasticity effects in vitreous silica. *Journal of Applied Physics*, 25(3):402–405, 1954.
- [95] O. L. ANDERSON and H. E. BMMEL. Ultrasonic absorption in fused silica at low temperatures and high frequencies. *Journal of the American Ceramic Society*, 38(4):125–131, 1955.
- [96] G. M. Harry, M. R. Abernathy, A. E. Becerra-Toledo, H. Armandula, K. Dooley E. Black, M. Eichenfield, C. Nwabugwu, A. Villar, D. R. M. Crooks, G. Cagnoli, J. Hough, C. R. How, I. MacLaren, P. Murray, S. Reid, S. Rowan, P. H. Sneddon, M. M. Fejer, R. Route, S. D. Penn, P. Ganau, J. Mackowski, C. Michel, L. Pinard, and A. Remillieux. Titania-doped tantala/silica coatings for gravitational-wave detection. *Class. Quantum Grav.*, 24:405–415, 2007.
- [97] Steve Penn, Jacob Podkaminer, Jing Luo, Christine Luongo, and Sean Kipperman. Recent measurements of mechanical loss of aligo coating research. Technical Report LIGO-G10000356, LIGO, 2010.

- [98] I W Martin, R Bassiri, R Nawrodt, M M Fejer, A Gretarsson, E Gustafson, G Harry, J Hough, I MacLaren, S Penn, S Reid, R Route, S Rowan, C Schwarz, P Seidel, J Scott, and A L Woodcraft. Effect of heat treatment on mechanical dissipation in ta 2 o 5 coatings. *Classical and Quantum Gravity*, 27(22):225020, 2010.
- [99] S. D. Penn, P. H. Sneddon, H. Armandula, J. C. Betzwieser, G. Cagnoli, J. Camp, D. R. M. Crooks, M. M. Fejer, A. M. Gretarsson, G. M. Harry, J. Hough, S. E. Kittelberger, M. J. Mortonson, R. Route, S. Rowan, and C. C. Vassiliou. Mechanical loss in tantala/silica dielectric mirror coatings. *Classical and Quantum Gravity*, 20:2917–2928, July 2003.
- [100] D R M Crooks, G Cagnoli, M M Fejer, A Gretarsson, G Harry, J Hough, N Nakagawa, S Penn, R Route, S Rowan, and P H Sneddon. Experimental measurements of coating mechanical loss factors. *Classical and Quantum Gravity*, 21(5):S1059, 2004.
- [101] D R M Crooks, G Cagnoli, M M Fejer, G Harry, J Hough, B T Khuri-Yakub, S Penn, R Route, S Rowan, P H Sneddon, I O Wygant, and G G Yaralioglu. Experimental measurements of mechanical dissipation associated with dielectric coatings formed using sio 2 , ta 2 o 5 and al 2 o 3. *Classical and Quantum Gravity*, 23(15):4953, 2006.
- [102] Juri Agresti, Giuseppe Castaldi, Riccardo DeSalvo, Vincenzo Galdi, Vincenzo Pierro, and Innocenzo M. Pinto. Optimized multilayer dielectric mirror coatings for gravitational wave interferometers. *Proc. SPIE*, 6286:628608–628608–10, 2006.
- [103] A. E. Villar, E. D. Black, R. DeSalvo, K. G. Libbrecht, N. Morgado C. Michel, L. Pinard, I. M. Pinto, V. Pierro, V. Galdi, M. Principe, , and I. Taurasi. Measurement of thermal noise in multilayer coatings with optimized layer thickness. *Physical Review D*, 81(122001), 2010.
- [104] Erika D’Ambrosio, Richard O’Shaughnessy, Kip Thorne, Phil Willems, Sergey Strigin, and Sergey Vyatchanin. Advanced ligo: non-gaussian beams. *Classical and Quantum Gravity*, 21(5):S867, 2004.
- [105] Mihai Bondarescu, Oleg Kogan, and Yanbei Chen. Optimal light beams and mirror shapes for future ligo interferometers. *Phys. Rev. D*, 78:082002, Oct 2008.
- [106] Benot Mours, Edwige Tournefier, and Jean-Yves Vinet. Thermal noise reduction in interferometric gravitational wave antennas: using high order tem modes. *Classical and Quantum Gravity*, 23(20):5777, 2006.
- [107] V.B. Braginsky, S.E. Strigin, and S.P. Vyatchanin. Analysis of parametric oscillatory instability in power recycled {LIGO} interferometer. *Physics Letters A*, 305(34):111 – 124, 2002.

- [108] C. Zhao, L. Ju, Y. Fan, S. Gras, B. J. J. Slagmolen, H. Miao, P. Barriga, D. G. Blair, D. J. Hosken, A. F. Brooks, P. J. Veitch, D. Mudge, and J. Munch. Observation of three-mode parametric interactions in long optical cavities. *Phys. Rev. A*, 78:023807, Aug 2008.
- [109] S. Gras, D. G. Blair, and L. Ju. Opto-acoustic interactions in gravitational wave detectors: Comparing flat-top beams with gaussian beams. *Phys. Rev. D*, 81:042001, Feb 2010.
- [110] John Miller. *On non-Gaussian beams and optomechanical parametric instabilities in interferometric gravitational wave detectors*. PhD thesis, University of Glasgow, 2010.
- [111] Stefan Goßler, Jeff Cumpston, Kirk McKenzie, Conor M. Mow-Lowry, Malcolm B. Gray, and David E. McClelland. Coating-free mirrors for high precision interferometric experiments. *Phys. Rev. A*, 76:053810, Nov 2007.
- [112] Deep Chatterjee, Matthew Abernathy, and Koji Arai. Design of a coating-less reference cavity with total internal reflection. Technical Report LIGO-T1300472-v1, LIGO/Caltech, 2013.
- [113] Daniel Friedrich, Bryan W. Barr, Frank Brückner, Stefan Hild, John Nelson, John Macarthur, Michael V. Plissi, Matthew P. Edgar, Sabina H. Huttner, Borja Sorazu, Stefanie Kroker, Michael Britzger, Ernst-Bernhard Kley, Karsten Danzmann, Andreas Tünnermann, Ken A. Strain, and Roman Schnabel. Waveguide grating mirror in a fully suspended 10 meter fabry-perot cavity. *Opt. Express*, 19(16):14955–14963, Aug 2011.
- [114] A. L. Schawlow and C. H. Townes. Infrared and optical masers. *Phys. Rev.*, 112:1940–1949, Dec 1958.
- [115] Melvin Lax. Classical noise. v. noise in self-sustained oscillators. *Phys. Rev.*, 160:290–307, Aug 1967.
- [116] T. J. Kane. *Coherent Laser Radar at 1.06-Microns Using Solid State Lasers*. PhD thesis, Stanford University, 1980.
- [117] Timothy Day. *Frequency Stabilized Solid State Lasers for Coherent Optical Communications*. PhD thesis, Stanford University, 1990.
- [118] R. V. Pound. Electronic frequency stabilization of microwave oscillators. *Review of Scientific Instruments*, 17(11):490–505, 1946.
- [119] R.W.P. Drever, J.L. Hall, F.V. Kowalski, J. Hough, G.M. Ford, A.J. Munley, and H. Ward. Laser phase and frequency stabilization using an optical resonator. *Applied Physics B*, 31(2):97–105, 1983.

- [120] Eric Black. Notes on the pound-drever-hall technique. Technical Report LIGO-T980045-00-D, LIGO/Caltech, 1998.
- [121] Fred L. Walls and Eva S. Ferre-Pikal. Measurement of frequency, phase noise and amplitude noise. Available online at <http://www.tf.nist.gov/timefreq/general/pdf/1287.pdf>.
- [122] B. Willke, N. Uehara, E. K. Gustafson, R. L. Byer, P. J. King, S. U. Seel, and Jr. R. L. Savage. Spatial and temporal filtering of a 10-w nd:yag laser with a fabry-perot ring-cavity premode cleaner. *Opt. Lett.*, 23(21):1704–1706, Nov 1998.
- [123] E. A. Donley, T. P. Heavner, F. Levi, M. O. Tataw, and S. R. Jefferts. Double-pass acousto-optic modulator system. *Review of Scientific Instruments*, 76(6):–, 2005.
- [124] H. Kogelnik and T. Li. Laser beams and resonators. *Appl. Opt.*, 5(10):1550–1567, Oct 1966.
- [125] Tianjun Li teal. Measurements of mechanical thermal noise and energy dissipation in optical dielectric coatings. Technical report, LMA, 2014.
- [126] Carmin DeCiantis. Private communication, May 12, 2014.
- [127] T. Nazarova, F. Riehle, and U. Sterr. Vibration-insensitive reference cavity for an ultra-narrow-linewidth laser. *Applied Physics B*, 83(4):531–536, 2006.
- [128] S. A. Webster, M. Oxborrow, and P. Gill. Vibration insensitive optical cavity. *Phys. Rev. A*, 75:011801, Jan 2007.
- [129] J. Millo, D. V. Magalhães, C. Mandache, Y. Le Coq, E. M. L. English, P. G. Westergaard, J. Lodewyck, S. Bize, P. Lemonde, and G. Santarelli. Ultrastable lasers based on vibration insensitive cavities. *Phys. Rev. A*, 79:053829, May 2009.
- [130] H Lck, J Degallaix, H Grote, M Hewitson, S Hild, B Willke, and K Danzmann. Opto-mechanical frequency shifting of scattered light. *Journal of Optics A: Pure and Applied Optics*, 10(8):085004, 2008.
- [131] Dennis Coyne. Ligo vacuum compatible materials list. Technical Report LIGO-E960050-v11, LIGO/Caltech, 2011.
- [132] Brian J. Meers and Kenneth A. Strain. Modulation, signal, and quantum noise in interferometers. *Phys. Rev. A*, 44:4693–4703, Oct 1991.
- [133] T. M. Niebauer, Roland Schilling, Karsten Danzmann, Albrecht Rüdiger, and Walter Winkler. Nonstationary shot noise and its effect on the sensitivity of interferometers. *Physical Review A*, 43:5022 – 5029, 1991.

- [134] C. Ishibashi, J. Ye, and J.L. Hall. Analysis/reduction of residual amplitude modulation in phase/frequency modulation by an eom. In *Quantum Electronics and Laser Science Conference, 2002. QELS '02. Technical Digest. Summaries of Papers Presented at the*, pages 91–92, May 2002.
- [135] J. L. Jewell, A. Scherer, S. L. McCall, A. C. Gossard, and J. H. English. Gaas?alas monolithic microresonator arrays. *Applied Physics Letters*, 51(2):94–96, 1987.
- [136] J. Talghader and J. S. Smith. Thermal dependence of the refractive index of gaas and alas measured using semiconductor multilayer optical cavities. *Applied Physics Letters*, 66(3):335–337, 1995.
- [137] J. Talghader and J. S. Smith. Erratum: thermal dependence of the refractive index of gaas and alas measured using semiconductor multilayer optical cavities [appl. phys. lett. 66, 335 (1995)]. *Applied Physics Letters*, 69(17):2608–2608, 1996.
- [138] J.J. Schermer, G.J. Bauhuis, P. Mulder, E.J. Haverkamp, J. van Deelen, A.T.J. van Niftrik, and P.K. Larsen. Photon confinement in high-efficiency, thin-film iiiiv solar cells obtained by epitaxial lift-off. *Thin Solid Films*, 511512(0):645 – 653, 2006. {EMSR} 2005 - Proceedings of Symposium F on Thin Film and Nanostructured Materials for Photovoltaics.
- [139] I. Schnitzer, E. Yablonovitch, C. Caneau, T. J. Gmitter, and A. Scherer. 30 percent external quantum efficiency from surface textured, thinfilm lightemitting diodes. *Applied Physics Letters*, 63(16):2174–2176, 1993.
- [140] I. Pollentier, L. Buydens, P. Van Daele, and P. Demeester. Fabrication of a gaas-algaas grin-sch sqw laser diode on silicon by epitaxial lift-off. *Photonics Technology Letters, IEEE*, 3(2):115–117, Feb 1991.
- [141] Garrett D. Cole, Yu Bai, Markus Aspelmeyer, and Eugene A. Fitzgerald. Free-standing alxgal?xas heterostructures by gas-phase etching of germanium. *Applied Physics Letters*, 96(26):–, 2010.
- [142] Garrett D. Cole, Ignacio Wilson-Rae, Katharina Werbach, Michael R. Vanner, and Markus Aspelmeyer. Phonon-tunnelling dissipation in mechanical resonators. *Nat Commun*, 2:644–650, 2011.
- [143] Garrett D. Cole, Wei Zhang, Michael J. Martin, Jun Ye, and Markus Aspelmeyer. Tenfold reduction of brownian noise in high-reflectivity optical coatings. *Nature Photonics*, 7:644–650, July 2013.
- [144] A. E. Siegman. *Lasers*. University Science Books, 1986.

- [145] Michael L. Gorodetsky. Thermal noises and noise compensation in high-reflection multilayer coating. *Physics Letters A*, 372(46):6813 – 6822, 2008.
- [146] Garrett D. Cole. Private communication.
- [147] E.F. Schubert. Refractive index and extinction coefficient of materials, 2004. <http://homepages.rpi.edu/~schubert/Educational-resources/Materials-Refractive-index-and-extinction-coefficient.pdf>.
- [148] Sadao Adachi. Gaas, alas, and alxga1xas: Material parameters for use in research and device applications. *Journal of Applied Physics*, 58(3):R1–R29, 1985.
- [149] Johannes Eichholz and Michael Hartman. Direct measurement of coating thermal noise with thor: Progress and cryogenic implementation. Technical Report LIGO-G1301008, LIGO/University of Florida, 2013.
- [150] R. Anderson, H. R. Bilger, and G. E. Stedman. sagnac effect: A century of earthrotated interferometers. *American Journal of Physics*, 62(11):975–985, 1994.
- [151] William Korth, Alastair Heptonstall, Eric Gustafson, Rana Adhikari, and Brian Lantz. Passive ring laser gyro for rotation sensing. Technical Report LIGO-T0900609-v1, LIGO/Caltech, 2009.
- [152] C. J. Hawthorn, K. P. Weber, and R. E. Scholten. Littrow configuration tunable external cavity diode laser with fixed direction output beam. *Review of Scientific Instruments*, 72(12):4477–4479, 2001.
- [153] Chloe Ling. Development of a low noise external cavity diode laser in the littrow configuration. Technical Report LIGO-T1300853, LIGO/Caltech, 2013.
- [154] S. Saito, Olle Nilsson, and Y. Yamamoto. Oscillation center frequency tuning, quantum fm noise, and direct frequency characteristics in external grating loaded semiconductor lasers. *Quantum Electronics, IEEE Journal of*, 18(6):961–970, Jun 1982.
- [155] F. Bondu, P. Fritschel, C. N. Man, and A. Brillet. Ultrahigh-spectral-purity laser for the virgo experiment. *Opt. Lett.*, 21(8):582–584, Apr 1996.
- [156] T. Kessler, C. Hagemann, C. Grebing, T. Legero, U. Sterr, F. Riehle, M. J. Martin, L. Chen, and J. Ye. A sub-40-mhz-linewidth laser based on a silicon single-crystal optical cavity. *Nat Photon*, 6:687–692, 2012.
- [157] Eva S. Ferre-Pikal and Fred L. Walls. Frequency standards, characterization. Available online at <http://www.tf.nist.gov/timefreq/general/pdf/1286.pdf>.

- [158] David R.M. Crooks. *Mechanical loss and its significance in the test mass mirrors of gravitational wave detectors*. PhD thesis, University of Glasgow, 2002.
- [159] Matthew R Abernathy. *Mechanical properties of coating materials for use in the mirrors of interferometric gravitational wave detectors*. PhD thesis, University of Glasgow, 2012.
- [160] M. Krieger, H. Sigg, N. Herres, K. Bachem, and K. Khler. Elastic constants and poisson ratio in the system alargaas. *Applied Physics Letters*, 66(6):682–684, 1995.
- [161] Kazuhiro Yamamoto. Thermo-optic noise at cryogenic temperature. Technical Report JGW-T1001852-v1, ICRR/University of Tokyo, 2013.
- [162] Thorlabs. Handling and cleaning procedures for optical components, May 2014. Available online at <http://www.thorlabs.us/tutorials.cfm?tabID=26066>.
- [163] Edmund Optics. Cleaning optics, May 2014. Available online at <http://www.edmundoptics.com/technical-resources-center/optics/cleaning-optics/>.
- [164] Thorlabs. How to clean optics, May 2014. Available online at <http://www.newport.com/How-to-Clean-Optics/141176/1033/content.aspx>.
- [165] Lord Rayleigh. A study of glass surfaces in optical contact. *Proceedings of the Royal Society of London. Series A - Mathematical and Physical Sciences*, 156(888):326–349, 1936.
- [166] Richard G. Budynas Warren C. Young. *Roark's Formulas for Stress and Strain*. McGraw-Hill, 7th edition, 2002.
- [167] Peter King, Rick Savage, Peter Wessels, and Benno Willke. Psl preliminary design. Technical Report LIGO-T0080195-v1, LIGO/Caltech, 2008.
- [168] Kenji Numata, Kazuhiro Yamamoto, Hidehiko Ishimoto, Shigemi Otsuka, Keita Kawabe, Masaki Ando, and Kimio Tsubono. Systematic measurement of the intrinsic losses in various kinds of bulk fused silica. *Physics Letters A*, 327(4):263 – 271, 2004.
- [169] Udo von Toussaint. Bayesian inference in physics. *Rev. Mod. Phys.*, 83:943–999, Sep 2011.